UNIVERSITÀ DEGLI STUDI DI PALERMO

DIPARTIMENTO DI ENERGIA, INGEGNERIA DELL'INFORMAZIONE
E MODELLI MATEMATICI (DEIM)

Dottorato in Ingegneria Elettronica e delle Telecomunicazioni
Doctorate in Electronics and Telecommunications Engineering

Computationally Efficient Innovative Techniques for the Design-Oriented Simulation of Free-Running and Driven Microwave Oscillators

Settore scientifico disciplinare ING-INF/01 Elettronica

TESI DI
ING. MARCO CARUSO

COORDINATORE DEL DOTTORATO
PROF. ING. GIOVANNI GARBO

TUTOR
PROF. ING. ENRICO F. CALANDRA

XXIV CICLO - ANNO ACCADEMICO 2013-2014

DOTTORATO

Abstract

Analysis techniques for injection-locked oscillators/amplifiers (ILO) can be broadly divided into two classes. To the first class belong methods with a strong and rigorous theoretical basis, that can be applied to rather general circuits/systems but which are very cumbersome and/or time-consuming to apply. To the second class belong methods which are very simple and fast to apply, but either lack of validity/accuracy or are applicable only to very simple or particular cases.

In this thesis, a novel method is proposed which aims at combining the rigorousness and broad applicability characterizing the first class of analysis techniques above cited with the simplicity and computational efficiency of the second class. The method relies in the combination of perturbation-refined techniques with a fundamental frequency system approach in the dynamical complex envelope domain. This permits to derive an approximate, but first-order exact, differential model of the phase-locked system useable for the steady-state, transient and stability analysis of ILOs belonging to the rather broad (and rigorously identified) class of nonlinear oscillators considered.

The hybrid (analytical-numerical) nature of the formulation developed is suited for coping with all ILO design steps, from initial dimensioning (exploiting, e.g., the simplified semi-analytical expressions stemming from a low-level injection operation assumption) to accurate prediction (and fine-tuning, if required) of critical performances under high-injection signal operation.

The proposed application examples, covering realistically modeled low- and high-order ILOs of both reflection and transmission type, illustrate the importance of having at one's disposal a simulation/design tool fully accounting for the deviation observed, appreciable for instance in the locking bandwidth of high-frequency circuits with respect to the simplified treatments usually applied, for a quick arrangement, in ILO design optimization procedures.

Acknowledgements

I would like to express my most sincere gratitude and appreciation to the following people for their help over the years, contributing to the completion of my Ph.D. program in the Università degli Studi di Palermo (*University of Palermo*).

First and foremost, I thank my Ph.D. supervisor Prof. Enrico F. Calandra for his inestimable guidance, strong support and cooperation throughout the three years of work together. In addition to assisting me with his knowledge and his valuable time, he also strongly contributed to my personal development, which was the most important outcome of this program.

I also acknowledge his contribution as director of the Laboratorio di Elettronica delle Microonde (LEM, *Microwave Electronics Laboratory*), which resources have been invaluable both for its hardware equipment and software simulators, by fulfilling all my research needs.

My gratitude is also extended to Dr Daniele Lupo, who shared part of my doctorate period, whose proficiency, willingness and competence often helped me in getting into some of the tougher topics. Moreover, I want to thank Dr Rosario Cirincione for his cooperation with skill, passion and expertise, as well as for his friendly nature to share anything about life, politics, culture, and especially music.

A special acknowledgement goes to my friend and Ph.D. colleague Dr Giovanni Artale, who accompanied my last five years of studies with his friendship, enthusiasm and inventiveness.

Table of Contents

List of Abbreviations

As a useful reference, a list of the main abbreviations adopted throughout this thesis is here presented, sorted mainly by appearance, but appropriately grouped for a better usability.

Abbreviation	*Full form*	*Definition*
ILO	Injection-locked oscillator	page 9
RILO	Reflection-type injection-locked oscillator	page 10
TILO	Transmission-type injection-locked oscillator	page 10
LBW	Locking bandwidth	page 9
LLI	Low-level injection	page 9
MLI	Medium-level injection	page 99
HLI	High-level injection	page 40
SIDF	Sinusoidal-input describing function	page 8
TSIDF	Two-sinusoid input describing function	page 51
FDDF	Frequency-dependent describing function	page 85
ST	Single tuned	page 12
MTNS	Multiple-tuned nearly-synchronous	page 86
EDA	Electronic design automation	page 15
ADS	(Agilent EEsof EDA) Advanced Design System	page 15
HB	Harmonic Balance	page 15
CE	Circuit Envelope	page 18
DCE	Dynamical complex envelope	page 17
SVA	Slowly-varying amplitude	page 17
OLG	Open-loop gain	page 20
BLDO	Band-limited differential operator	page 21
SS	Steady state	page 22
CW	Continuous wave	page 23
NDR	Negative differential resistance	page 48
ASB	Adynamic shifting-bias	page 52
DR	Dielectric resonator	page 78
QS	Quasi sinusoidal	page 85
QS^2	Quasi sinusoidal quasi static	page 85
OSB	One side band	page 91
LCPM	Least common polynomial multiple	page 92

1. Introduction

1.1 Framework and Motivations

Electronic oscillators have been studied for a long time now, and for various purposes: in fact, they are the key element of most communication equipments as well as of test and measurement systems. Aside from their most common use under free running operation (i.e., with no input signal acting upon) there is the possibility of a driven operation, with an injection signal of proper amplitude/frequency applied to achieve a "synchronized" oscillation through the nonlinear phenomenon of "injection phase-locking".

Injection-locked oscillators are a class of nonlinear circuits with peculiar features. They are adopted in the RF and microwave frequency ranges when a highly-saturated, narrow-band, amplification of a weak signal is required [1]. In this case they are also indicated as injection-locked amplifiers to stress their oscillating amplifier nature. They can also be adopted to obtain, from a high-power high-efficiency but noisy oscillator and a low-power low-noise source, a quasi-sinusoidal signal with excellent phase noise performances [2,3].

Their use has recently been brought back to the top by several new applications, for example wireless LAN [4] and wireless body area network receivers [5], as well as signal generators with the purpose of filtering and phase-shifting the clock in micro-processors [6], or low-power low-noise amplifiers in vital-sign sensors [7].

Driven oscillators are also adopted in other applications, such as frequency multipliers [8–10], frequency dividers [11–15], alternatives to PLLs [16], self-oscillating mixers [17,18], or devices for beam-steering of phased arrays [19,20].

Because of the nonlinear resonant nature of the equations characterizing such circuits, conventional analysis or simulation techniques in the time-domain are extremely inefficient, especially if global behavior quality indexes are of interest, e.g., for design purposes. The theoretical studies not always account for all practical design issues, and the software tools, while extremely powerful in the (numerical) evaluation of circuit responses, lack to provide synthetic evidence of the involved phenomena.

The best example is represented by the evaluation of the locking bandwidth (LBW), i.e., the range of frequencies where the phase-lock condition is achieved. Especially in case of low-level injection operation, where the LBW is a small fraction of the carrier frequency, this search, if carried out numerically, can become extremely time consuming (see Appendix A1 for required time durations). For this reason, a number of methods have been developed in the past for the study of injection locked oscillators in the stroboscopic time-domain, i.e., directly in terms of amplitude and phase of the fundamental component of oscillating signals [2,21]. In case the analysis is developed in a completely numerical manner (e.g., using *Circuit Envelope* algorithms [22]), there is a significant advantage in terms of computational efficiency, but the problem of the lack of a design-oriented tool remains. Also, while the steady-state and transient operation are efficiently simulated, the same does not occur for the LBW evaluation, which still involves a time-consuming, man-assisted, iterative search procedure through the bracketing of stable and unstable solutions in the surroundings of the unlock frequency limits. As to the fully analytical approaches, while potentially extremely powerful, they have to cope with the difficulties of such a stiff dynamical nonlinear problem [2, 23–28]. Therefore, they usually ground on substantial approximations of the problem, which either limit the class of treatable systems, or reduce the accuracy of the analysis. In particular, it can be noticed that while the frequency-domain theory of oscillating amplifiers equipped with negative-resistance microwave diodes is relatively complete [24], the same does not hold for more up-to-date circuit configurations using RF transistors as active element(s) and a transmission-type topology [23].

Understanding how to act in order to obtain a given design goal, or forecasting global behavioral aspects is left to the designer's intuition. This often leads to inefficient cut and try iterative design procedures. Or, as an alternative, a flawed non-optimized design can be conducted by means of approximated models and procedures, which of course don't allow actual optimizations.

All of these thorny problems arose during the design of a 10 GHz injection-locked oscillator, carried out by student Lorenzo Puccio for his Master's Degree thesis work, inside the LEM laboratory (Microwave Electronics Laboratory) in DIEET Department of the University of Palermo, while I was putting my effort in the same lab into my Bachelor's Degree thesis. That way I could see already by then, with my own eyes, the difficulties encountered during design and realization steps of microwave injection-locked oscillators, and discrepancy between theoretical forecasts and experimental results. That indirect experience contributed to the choice of topic for research later conducted over my Ph.D. program. Such circumstance stimulated a personal motivation originated by curiosity, which added to theoretical and technical reasons above exposed.

1.2 Outline of Achieved Results

In this thesis, a novel hybrid (analytic-numerical) approach to the above stated design problem is proposed. The aim was to combine high computational efficiency with a reasonably wide applicability range, so to cope with real world circuits and permit their performance optimization with a design-oriented consistent procedure that reduces to the bare minimum cut-and-try iterations. This goal has been achieved in various subsequent steps.

A general, reduced-order, model of the injected oscillator is firstly introduced. A perturbation-refined analysis method is then applied, which permits to derive the first-order exact set of differential equations describing the circuit behavior in the fundamental-frequency complex-envelope domain. This differential model is the basis for all subsequent steps, including transient response calculations, phase-lock stability analysis and the secondary simplification that permits a simplified, semi-analytical, investigation of the low-level injection operation, useful for initial circuit dimensioning.

As shown later on through the worked out examples, this perturbation-refined first-order exact method do actually achieve the stated goal of combining high computational efficiency and reasonably good accuracy for the rather broad class of treatable circuits and systems, subsequently widened by virtue of a further novel semi-numerical approach. This latter one, fully addressing higher injection signals whose investigation has an increasing leading role [12], represents a convenient alternative to the use of purely numerical, iterated and simulation-based, design approaches usually adopted in practice, with respect to which produces a better phenomenological insight due to its partially analytical base. Since it incorporates, extending significantly their applicability range, also all previous simplified treatments (e.g. the Adler-based methods), it provides a unified design environment for all the steps of an injection-locked system design, with the important difference, with respect to some of them, of a solid theoretical ground.

During the various investigation steps that led, in the three year period here described, to the completion of the development of such analysis method, intermediate theoretical results have been validated through an extensive campaign of simulation and experimental tests.

1.3 Thesis Organization

Firstly, the state of the art in the field of free-running and driven oscillators is examined. In **Chapter 2** classical models for injection-locked oscillators as well as newer ones are quickly described, ranging from old Adler's treatment, to recent Ohira's method. Different classes of injection locked oscillators are introduced, and comparisons between different techniques have been carried out.

Chapter 3 is concerned with introduction into phasor domain approach, and dynamical complex envelope analysis. Fully analytical method, its applicability conditions, and explanation of the concepts employed throughout the present thesis are examined in depth, e.g., describing functions, dynamical locking stability, Locus and Boundary limits, lateral bands. A simple single-tuned example is presented to better explain all passages.

Chapter 4 deals with discovered phenomena related to the shifting of bias point, where the interaction between DC and RF signal not only produces quantitative effects, but new qualitative consequences are observed, too, especially in terms of particular locking regions.

In **Chapter 5** the proposed theory is enhanced to cope with transmission-type class circuits, with the main result of the introduction of a new effective quality factor instead of classical or loaded ones, usually adopted in literature. Three different examples are presented to clarify and validate the presented method.

An absolutely new approach, addressing high-order feedback-type driven oscillators, of circuital or any other nature, is presented in **Chapter 6**. This semi-numerical analysis method can be particularly useful when internal topology of the circuit is not known, or suitable models are not available, and data can be more easily identified on the basis of direct measurements. An extended step-by-step application procedure is presented by means of a rather troublesome example, where several parasitic elements (usually neglected in literature) are accounted for.

In the end, three **Appendices** include further analyses, an effective comparison between time required by simulations with EDA tools versus computation of presented methods with mathematical software, and a few extra formulas.

2. State of the Art

2.1 Oscillators and Injection-Locked Oscillators

A simple oscillator is, as a principle, a circuit composed by an amplifier and a resonator, with a positive feedback loop taking the filtered output signal back to the input of the amplifier. The natural input noise is amplified until the nonlinearity of the amplifying stage reduces the loop gain to unity, landing to a dynamic equilibrium. This is - in short - the Barkhausen stability criterion, which is strictly applicable only to linear systems, but represents an easy reference for understanding oscillators' behavior.

Since the system is nonlinear, output signal is not a pure sinusoidal indeed. Actually, when the resonator has a reasonable quality factor, it can be defined a "quasi-sinusoidal" oscillator, since higher harmonics have much lower magnitude than the fundamental tone. Moreover, to achieve this property, many systems feature a weak nonlinearity, i.e., their state equations can be written in the form:

$$\frac{d\mathbf{x}}{dt} = \mathbf{A}\cdot\mathbf{x} + \varepsilon\,\mathbf{f}[\mathbf{x}] \tag{2.1}$$

where **A** is the state matrix, **x** is the state vector, and $\varepsilon\,\mathbf{f}[\mathbf{x}]$ is the weakly nonlinear relationship. The epsilon factor represents the smallness of the "deviation" from a pure linear system (which would provide $\varepsilon = 0$).

Oscillators can be broadly divided into "negative resistance" and "feedback loop" types, although both categories can be studied with the same general system theory [29]. First ones employ a nonlinear element whose resistance is negative – under a differential perspective – which is the case of tunnel diodes, for instance, that show an "N-shaped" I-V characteristic. Biasing the element in the descending section, a negative differential resistance is exhibited, i.e., to a (small) increase in the voltage corresponds a (small) decrease in the current. Under oscillating conditions, this negative resistance perfectly balance the positive resistance deriving from the losses of the resonator.

A positive feedback loop is the main feature of the second above-mentioned class of oscillators. The focus this time is on a path designed to bring the oscillation back to the input of a loop, thus sustaining the oscillations. Generally this path is well defined from a circuital point of view.

A simple approximation of an N-shaped characteristic is commonly obtained with a cubic polynomial nonlinearity, whose smooth qualities ease the treatment. One common modeling option for the nonlinear element is the employment of a *Sinusoidal-Input Describing Function* (SIDF) [30], that is a linearization of that nonlinear element subjected to a sinusoidal input, as a function of its amplitude and phase.

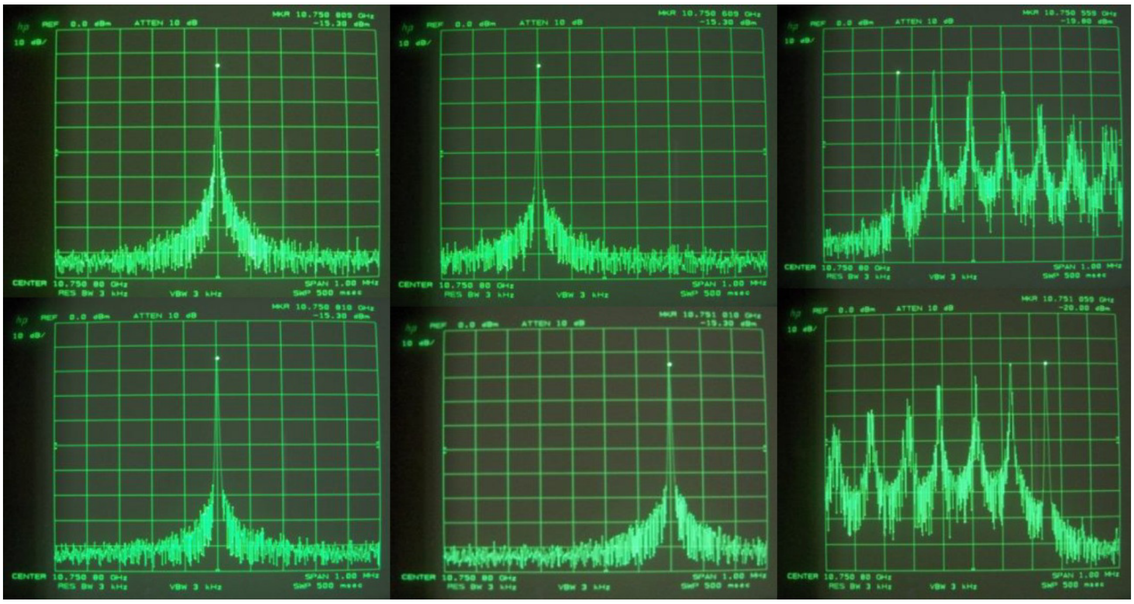

(a) *(c)* *(e)*

(b) *(d)* *(f)*

Fig. 2.1 – Spectrum of an injection-locked osc. under all possible operating conditions [31]:
(a) free-running oscillation; (b) locked state, $f_{INJ} = f_{OSC}$;
(c,d) detuned locked state, $f_{INJ} < f_{OSC}$ *and* $f_{INJ} > f_{OSC}$;
(e,f) detuned unlocked state, $f_{INJ} \ll f_{OSC}$ *and* $f_{INJ} \gg f_{OSC}$

On various types of oscillators, a specific phenomenon can occur, producing an (intentional or accidental) variation in oscillator's output quantities - in terms of frequency and/or amplitude (and power, consequently). This behavior, named injection locking, can take place when an appropriate external signal drives the oscillator to a different steady-state regime. The locked state happens if the detuning between free-run and injected frequencies is limited, otherwise an unlocked state will be observed, characterized by a spectrum where many beating tones appear (Fig. 2.1). The difference between the maximum and the minimum locking frequencies is called *locking bandwidth* (LBW). The LBW increases when input power is higher, with a linear relationship for a *Low-Level Injection* (LLI). With higher injection rates, the bandwidth follows a nonlinear relationship, depicting what is known as *Arnold Tongue* (Fig. 2.2) [32].

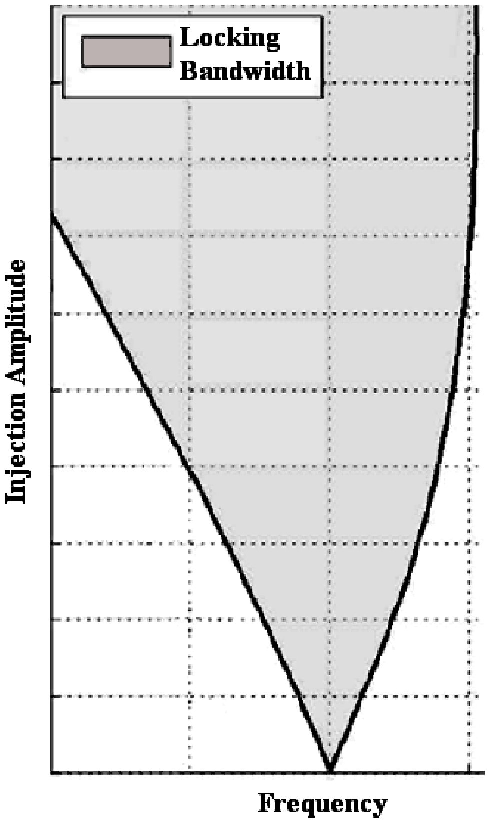

Fig. 2.2 – Locking bandwidth shaped as an Arnold Tongue.

In some oscillators, injection locking represents an interference event, caused by an excessive coupling between two or more lines. On the other hand, many circuits are specifically designed to benefit from it, such as the several types listed in Section 1.1. The class represented by saturated amplifiers [33–35] is the one this thesis will be mostly focused on, and will be here identified with the name of *Injection-Locked Oscillators* (ILOs), even though this naming is sometimes adopted to refer to all circuits based on injection-locking phenomenon as well. Because of their nonlinear amplifying nature, ILOs are also defined *Oscillating Amplifiers*, emphasizing their usage on non-monochromatic applications.

Older configurations detailed in the technical literature consider the usage of a classic standalone oscillator, equipped with a nonlinear active one-port element, where the drive signal is injected by means of a circulator, in order to provide power insulation between input and output ports. These circuits are called *Reflection-type Injection-Locked Oscillators* (RILOs), as opposite to *Transmission-type Injection-Locked Oscillators* (TILOs) [3,23] (Fig. 2.3). These latter ones are realized by designing an oscillator with separate signal-input and power-output ports, e.g., by means of a nonlinear active two-port device.

It is notable that a transmission-type, while retaining high gain, provide a higher locking bandwidth, often doubling it, moreover eliminating the need for a ferrite circulator [36]. The employment as oscillating source of a three-terminal device with a large maximum-stable gain, such as a GaAs FET, is demonstrated to produce a locking range wider than the one obtainable by means of a reflection-type ILO [23].

The other main characterizing specification of an ILO is the injection-ratio ρ, defined as the ratio between the output power of the ILO and the injection signal power (i.e., the equivalent of the power gain for conventional, non-saturated, amplifiers). Unfortunately, ρ and the locking bandwidth achievable for any given injection-ratio value are conflicting each-other (a high value of ρ implies a small LBW, and vice versa) and appropriate trade-off has usually to be determined for fulfillment of system-level induced specifications on the ILO.

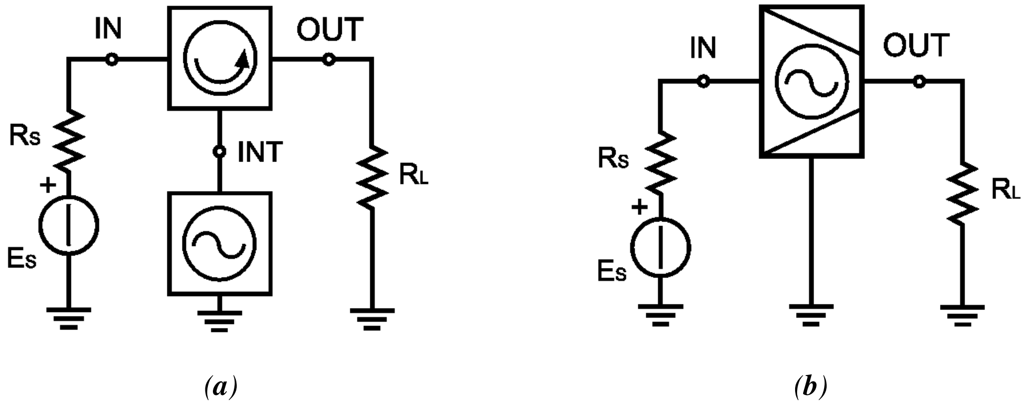

Fig. 2.3 – Classes of Injection Locked Oscillators:
*(**a**) Reflection-type (RILO); (**b**) Transmission-type (TILO).*

2.2 Adler's Equation

One of the leading milestones in injection-locking theory was posed by a study published by Robert Adler in 1946 [26], which means one year before Bardeen, Brattain and Shockley invented the first bipolar transistor at Bell Laboratories. Despite its age, his work is still one of the main references in this field. Adler obtained a differential equation describing the oscillator phase as a function of time, employing a simple tuned vacuum tube oscillator as example, where he could express:

$$\text{(2.2)} \qquad \sin[\alpha] = 2Q \frac{E_0}{E_1} \frac{\omega_0 - \omega_1}{\omega_0}$$

with E_0 and E_1 the voltage amplitude across nonlinear element under free-run oscillation and amplitude of injected signal, respectively, α the phase shift between those two signals, ω_0 and ω_1 the (angular) free-run oscillation frequency and injected signal's frequency, respectively. The Q factor represents the quality factor of the single tuned resonator. Since the absolute value of sine cannot exceed the unity, the relationship (2.2) is used to evaluate the maximum detuning $\Delta\omega_0 = \omega_1 - \omega_0$ at a specific E_1 injection level, in case of a single tuned (2.3a) or a generic resonator (2.3b):

$$\text{(2.3a)} \qquad \Delta\omega_{0,\,\max} = \frac{\omega_0}{2Q} \frac{E_1}{E_0}$$

$$\text{(2.3b)} \qquad \Delta\omega_{0,\,\max} = \frac{1}{\tau_g} \frac{E_1}{E_0}$$

It is to be noted that the adoption of the group delay $\tau_g = -\,d\theta_{OLG}/d\omega$, where θ_{OLG} is the phase of the open-loop gain, is (and is declared as) a valid approximation only because of the assumption that all frequencies are near the free-run oscillation one, therefore supposing a linear behavior. This is equivalent to considering a low-level injection, which is important to be pointed out for next sections' investigations.

2.3 Kurokawa's Development

A simple *single-tuned* (ST) model for the circuit's resonator is inadequate in many applications, and some specific behaviors were discussed by Kaneyuki Kurokawa [37], like rapid changes in (free-run) oscillation frequency and hysteresis effects, that could find no full explanation with such an elementary model, especially from a quantitative perspective. He underlined the importance to adopt a multiple-resonance model, in order to address some practical considerations. Also, he showed the benefits of practical introduction of several resonator networks (Fig. 2.4) in order to obtain some performance improvements, like the LBW widening or the goal of a greater linearity. Under his conditions, all these resonators must have a resonance frequency in the neighborhood of the oscillation one, i.e., the whole resonator is modeled as a multiple-tuned nearly-synchronous one.

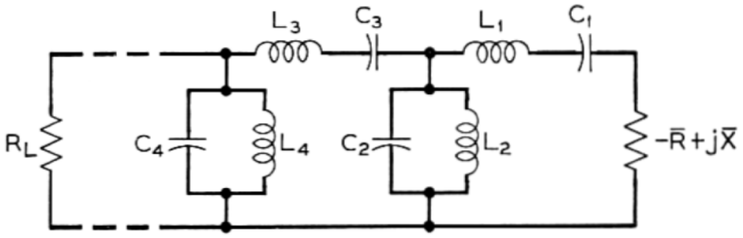

Fig. 2.4 – An oscillator with a multiple-resonant circuit, by Kurokawa [37].

Further, Kurokawa studied on expansion of Adler's theory, presenting a comprehensive theoretical review for the injection-locking of solid-state ILOs in 1973 [2], and deriving a similar locking-bandwidth equation. Kurokawa’s work covers almost all information on the matter available at that time, and addresses both quasi-static and dynamic analyses of the locking range, large-signal injection and locking stability. His theory is the first one to introduce the circulator to separate the injection signal and the oscillator output signal, and was also used to develop a locking bandwidth equation for transmission type injection-locked oscillators [23]. His formula differs from Adler's one primarily because Kurokawa employs the external Q-factor instead of the loaded one, but still treats it as a constant value [38].

2.4 Gen-Adler Equation by Roychowdhury

The interest on the topic raised again in 2004 when Behzad Razavi wrote a detailed an in-depth summary and analysis of some injection locking peculiarities, and enhanced the theory in order to manage quadrature oscillators and then frequency dividers [39].

This path proceeded in 2009 when Prateek Bhansali and Jaijeet Roychowdhury, University of Minnesota, published a generalization of Adler's formula, defining it "Gen-Adler equation". That work [27], grounded on the studies carried out by Roychowdhury since 2004 [25], presents a method that is not limited to LC oscillators, and therefore dependent on quality factor, as the Adler one was. Procedure proposed by those authors makes use of PPV (*Perturbation Projection Vector*) phase macromodel to determine the locking range for LLI signals, and formulates an analytical equation averaging that model. It lands to:

$$\frac{d\Delta\phi[t]}{dt} = -(\omega_1 - \omega_0) + \omega_0 \cdot g[\Delta\phi[t]] \tag{2.4}$$

where

$$g[\Delta\phi[t]] \equiv \int_0^1 \chi\big[\Delta\phi[t]+\phi_1[t]\big] \cdot b\big[\phi_1[t]\big] d\phi_1[t] \tag{2.5}$$

and $\Delta\phi[t] \equiv \phi[t] - \phi_1[t]$ is the phase difference between the oscillator's reference phasor and the injection signal phasor, while $b[\cdot]$ is the injection function, defined as a 1-periodic function (i.e. $b[\omega_1 t] = b[\omega_1 t + 1]$). The $\chi[\cdot]$ function is a generic 1-periodic function also. Angular frequencies ω_1 and ω_2 are the same defined in Section 2.2.

This equation is demonstrated to reproduce Adler's formula under his assumptions and peculiar example circuit, but considerably extending the range of applicability from this point of view.

However, it assumes a low-level injection, and is therefore unable to cope with higher injection levels. This technique represents the first extension of the linearized problem, but cannot tell the basic structure of the amplitude perturbation signal and the modifications of the oscillator locking properties compared to small amplitude perturbation. Other studies, later on, have captured and studied the modifications of the locking characteristics of the oscillator under an injection of noticeable amplitude.

2.5 Ohira's Determination of the Q-factor

In parallel with Roychowdhury's studies on the matter, Takashi Ohira developed a novel approach for the determination of the locking bandwidth. His work, published in 2010, is mainly based on his previous examinations on Q-factor of oscillator circuits. The aim is to extend the original Adler's relationship, substituting its quality factor of the resonator with a new coefficient calculated through linear Z[ω] matrix of the network. This makes it a simple method, while applicable to a wide class of circuits.

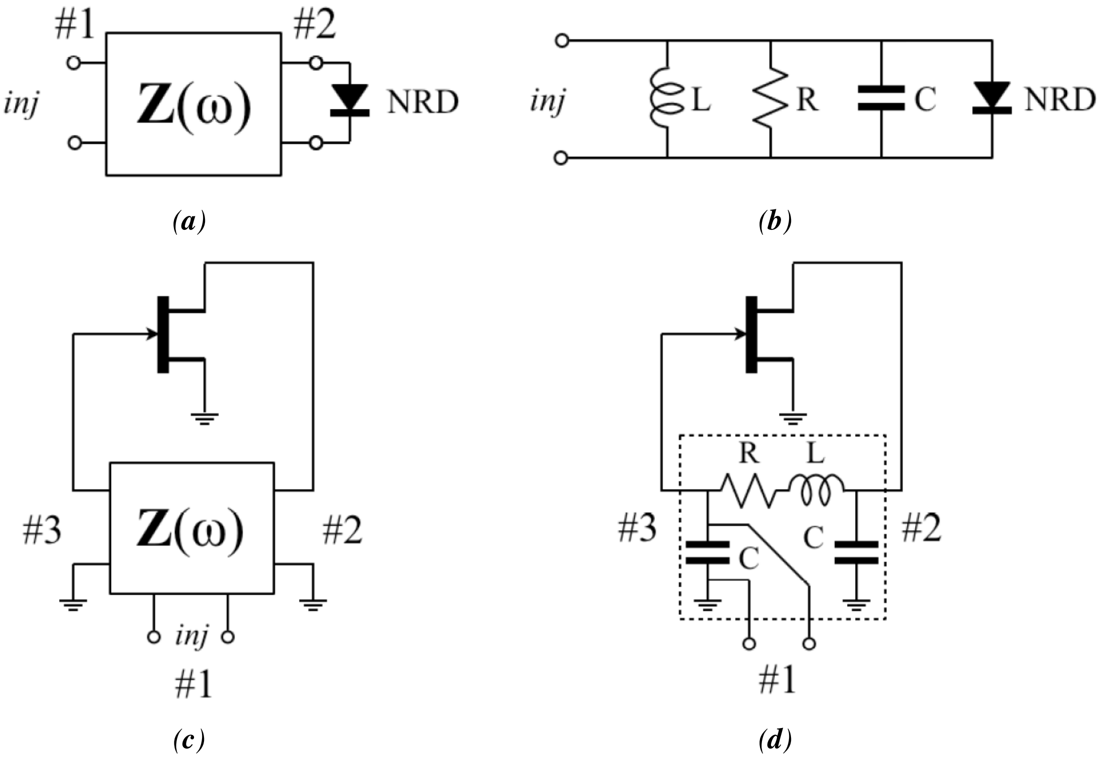

(a) (b)

(c) (d)

*Fig. 2.5 – Subdivision by Ohira of injection-locked oscillators employing (**a**, **b**) one-port active device, (**c**, **d**) two-port active device. Simple models (**a**, **c**) and simple examples (**b**, **d**) are provided [28].*

It considers specifically, as notable examples of different structures, one-port and two-port active device oscillators, providing a precise analysis of those two cases (Fig. 2.5). However, it addresses only negative real resistance models, and even if it can be extended to device including reactive components such as parasitic capacitance, by moving them from device to passive network, it is unable to treat nonlinear parasitic elements. Nevertheless, it disregards nonlinear dynamic aspects of the involved phenomenon, since it doesn't appropriately take cognizance of what happens in presence of generic amplitude signals and, above all, it doesn't provide the applicability limits for evaluated linear bandwidth.

2.6 State of the Art in the EDA Field

Beyond all analytical or semi-analytical approaches, a free-running or injection-locked oscillator circuit can obviously be simulated by means of *Electronic Design Automation* (EDA) tools. We will adopt as a reference the most popular and complete simulation software, that is *Advanced Design System* (ADS) [22] by *Agilent EEsof*. As already pointed out, these class of circuits are very stiff and performing an exhaustive analysis through an EDA software is not practicable.

The easiest and more straightforward simulation is the one aimed to free-running oscillation point evaluation. It is carried on by means of *Harmonic Balance* (HB) algorithm, where the simulation frequency – being unknown – is found inserting in series an ideal probe (named "OscPort") in the feedback loop.

Driven regime conditions can be evaluated in a similar manner. An HB simulation permits to obtain steady-state solution (if it exists) under any injection amplitude/frequency couple given by the user. But, if a more general picture is attempted, some problems arise. Steady-state curves may provide useful information about the locking bandwidth, but only if the injection level is not high, and their production is not flawless. The best procedure to achieve workable results is quite laborious. Here is provided an outlook of it. First required step is finding the value of the free-running oscillation, putting injection to zero if present, ensuring to save all state variable data in an output automatically-generated file. Second, a frequency-swept HB simulation has to be performed, deactivating the oscillator mode, for a specific amplitude of the injection. Previous saved data is employed, which means the topology of the circuit must not be altered, or the number of involved nodes/branches would change and loading the old output file will be impossible. It is required to use that information on the free-running oscillation because, otherwise, the simulator engine would typically reach the wrong solution, i.e. the lowest one, which is normally an unstable one. To better understand those curves, see Sec. 3.6. Furthermore, HB simulator is clearly unable to find a regime when in unlocking conditions, and if this situation is met it aborts the simulation and returns only data generated until that moment. For this reason, it's necessary that the user provides a frequency range that doesn't start from a value outside the locking region, which has therefore to be known or found by iterated attempts. Setting a stop frequency higher of the last locking one is instead possible. In that case the simulator will return an error, but all collected data will be given. It is thus possible to try and perform the simulation sweeping frequency starting from a value just a little higher of the free-running oscillation one. This approach usually provides useful indications. But it must be remarked that sometimes convergence problems are met even in the simple case of a starting point close (little lower or little higher) to the free-run oscillation frequency.

The third type of analysis that is possible to carry on is the traditional transient one. In such stiff circuits there are time constants so different that it's impossible to choose an integration-step accomplishing high precision on a sufficiently wide time range. In fact, there are normally big differences between the period bound to oscillations (free-running or driven) and the time needed to reach the regime (e.g., for injection case or the start-up time). A regular transient analysis is therefore not a viable way to study driven oscillators.

In Section 3.1 a powerful alternative for the study of transient evolution will be introduced, named Circuit Envelope. However, it still offers only a local information and, when used to obtain the whole locking bandwidth, or just a few-dots approximation of it, it requires an extremely long time. Since its operating principle is quite complex, further details are left to Sec. 3.1, while more information on both a step-by-step simulation procedure and on time duration is provided in Appendix A1.

3. Presented Dynamical Phasor Domain Theory

3.1 Dynamical Complex Envelope

As described, the study of injection locking phenomenon is more convenient when performed in the phasor domain. Since the involved quantities are phasors which magnitude and phase can change over time, depending on the injected signal instantaneous value, the best way to describe its equations is the employment of the *dynamical complex envelope* (DCE) domain. An example will clarify its characteristics and usage.

When a sinusoidal signal with angular frequency ω is applied to an impedance Z, it is possible to describe the current flowing through it by means of the classical electric relationship defined in the phasor domain:

$$\mathbf{I} = \mathbf{Z} \cdot \mathbf{V} = (R + j\,X) \cdot V \cdot e^{j\phi} \tag{3.1}$$

Assuming that amplitude V and phase ϕ of the applied voltage are slow functions of time, this equation in the dynamical complex envelope domain is obtained:

$$\mathbf{I}[t] = (R + j\,X) \cdot V[t] \cdot e^{j\phi[t]} \tag{3.2}$$

In this relation it has been supposed that variables have a *slowly varying amplitude* (SVA). It's possible to think about it as a quasi-static equation that is valid every discrete time-step, provided the envelope changes much slower than the carrier of the signal.

Behind these apparently trivial relationships is hidden one more of the fundamental bricks in the DCE domain theory. When the frequency of the signals in the oscillator under analysis varies over time, but is enclosed inside a narrow band, it can be assumed as a constant, and its variation can be handled just as if it was a phase variation over time. Joining this together with the capability to treat time dependent amplitudes, it is possible to employ the DCE theory to study modulated signals such as those found in high-frequency amplifiers, oscillators, mixers, and ILOs. Furthermore, for many of these circuits transient analysis is possible too.

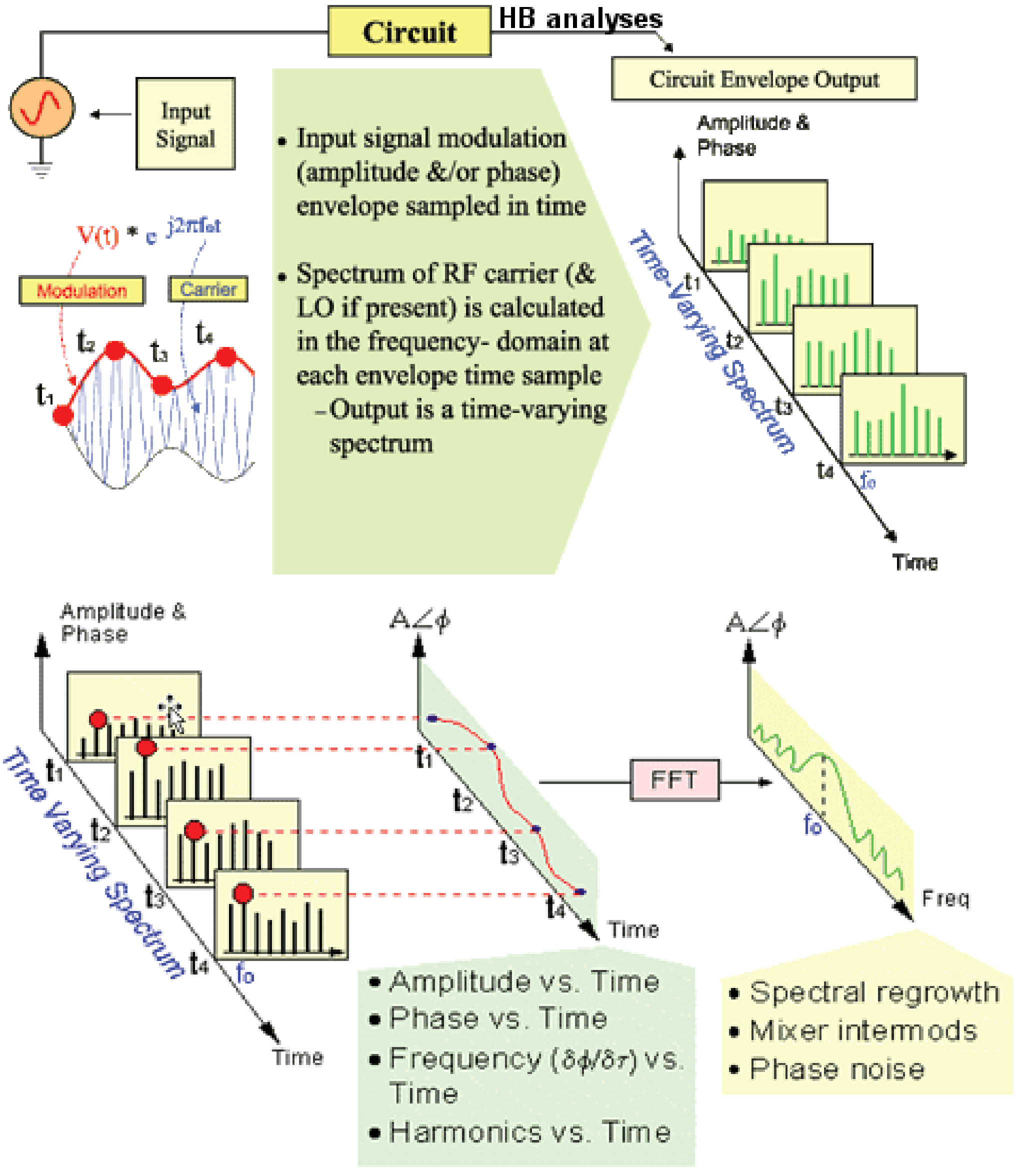

Fig. 3.1 – Example of ADS Circuit Envelope simulation process [40].

DCE domain theory is notably implemented in ADS in the *Circuit Envelope* (CE) simulation [22,40,41]. The values of amplitude and phase of the sampled envelope are used as input signals for HB analyses (Fig. 3.1): at each time step an HB analysis is performed, therefore evaluating the corresponding spectrum for that time step. A time domain representation of the desired amplitude and phase evolutions is obtained through a Fourier series with evaluated time-varying complex coefficients, therefore every single node – independent (e.g., input signal) or dependent – is represented by means of the relationship:

$$v[t] = \mathrm{Re}\left[\sum_{k=0}^{N} \mathbf{V}_k[t] \cdot e^{j\omega_k t}\right] \tag{3.3}$$

where ω_k is the k-th (angular) frequency, N is the user-defined number of harmonics selected in the simulation, and $V_k[t]$ is the coefficient, often referred to as the "k-th envelope".

However, when studying a circuit with analytical procedures, only fundamental harmonic is usually considered, considerably simplifying the treatment. In particular, when a selective resonator is present, higher harmonics can be neglected without great reduction in accuracy.

3.2 Method's Application and Equations

The analysis method proposed in the present thesis, in the dynamical complex envelope domain, first of all deals with the study of the circuit through its system analogy. Please note that this system representation is broader than the only circuital subclass, and the following theory can also manage, with little o no variation, different settings, e.g., laser oscillators [42–46], mechanical [47], acoustic oscillations [48], biological machines [39,49], etc. The theoretical demonstration for this approach is based on perturbation theory developed by E. F. Calandra and A. Sommariva [24,21], to which considerable extensions have been applied. A very specific example will be adopted in this section, in order to better understand the main features of the proposed approach, which will be later explained in detail.

The phasor-domain block diagram related to an example of a simplified driven oscillator is depicted in Fig. 3.2, in which the system block G_N represents the describing function of a conductance-type nonlinear element, i.e., a device whose characteristic equation is $I_O = f[V_I]$, like a tunnel diode. Indeed, a pure real element has been chosen for now for the sake of simplicity, which is function of only one input variable. All of the voltage/current variables shown in figure are to be intended

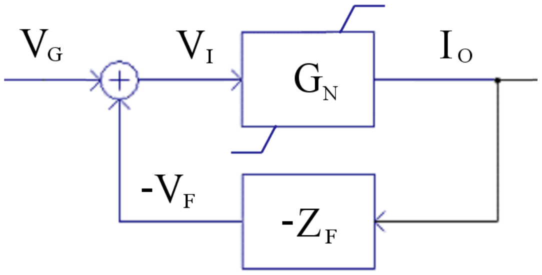

Fig. 3.2 – Phasor-domain example block-diagram of a simplified driven oscillator.

in fundamental-mode, and under the above-quoted SVA hypothesis. In this diagram a feedback loop can be found by means of the linear feedback impedance $\mathbf{Z}_F$, generating the voltage $\mathbf{V}_F$ which is subtracted from the injection voltage $\mathbf{V}_G$, to restore the $\mathbf{V}_I$ again. The open-loop gain (**OLG**) of the free-running oscillator alone (i.e., $\mathbf{V}_G = 0$) turn out to be therefore:

$$\mathbf{OLG} = -G_N \cdot \mathbf{Z}_F \tag{3.4}$$

In order to obtain, at the resonance frequency (or, more properly, at the oscillation frequency), an OLG magnitude equal to unity and phase equal to zero, it is clear that G_N must be an active element characterized at ω_{OSC} by a negative resistance, whose value equals the (positive) resistance exhibited - at the same frequency - by the resonator.

In Fig. 3.3 is depicted a circuital example that can be represented with above analyzed block diagram. In this case, impedance $\mathbf{Z}_F$ is constituted by a second-order circuit, precisely a parallel RLC filter.

As it can be observed from this figure, the conformity with previous block diagram is guaranteed by the validity of following relationships:

$$\begin{aligned} &\mathbf{V}_G - \mathbf{V}_F = \mathbf{V}_I \\ &\mathbf{I}_O = G_N[V_I] \cdot \mathbf{V}_I \\ &\mathbf{V}_F = \mathbf{Z}_F \cdot \mathbf{I}_O \end{aligned} \tag{3.5}$$

where voltages and currents are generalized time-varying phasors $\mathbf{X}_n = X_n[t] \cdot e^{\,j\phi n[t]}$, with $X_n[t]$ and $\phi_n[t]$ slowly-varying amplitude quantities in the scaled time t/T_0 (T_0 being the period of the free-running oscillation). This is tantamount to saying that

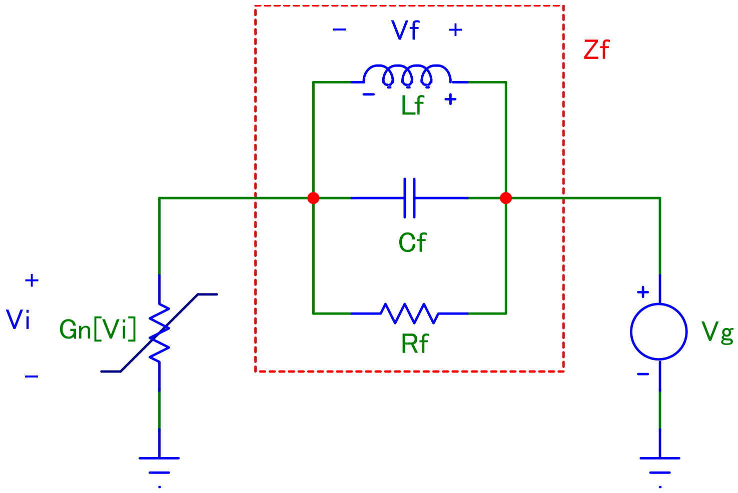

Fig. 3.3 – Example circuit of simplified driven oscillator.

their variation is "small" in the period of the fundamental of the oscillation under both free-running and phase-locked operation.

Combining equations (3.5), the frequency-domain nonlinear phasor equation is obtained:

$$(1 + \mathbf{Z}_F \cdot G_N[V_I]) \cdot \mathbf{V}_I = \mathbf{V}_G \tag{3.6}$$

which characterizes the behavior of injection-locked oscillator, through the nonlinearity input voltage $\mathbf{V}_I$, as a function of the driven voltage $\mathbf{V}_G$. In this specific case, the $\mathbf{Z}_F$ filter is represented by a well known parallel RLC circuit, whose impedance equals:

$$\mathbf{Z}_F = \frac{R_F}{1 + jQ_F \dfrac{(\omega^2 - \omega_F{}^2)}{\omega \cdot \omega_F}} \tag{3.7}$$

where ω_F is the resonance (angular) frequency ($1/\sqrt{L_F\, C_F}$), and Q_F the quality factor ($\omega_F\, R_F\, C_F$). Now, with a less rigorous demonstration with respect to [21], the same DCE equations will be derived, with respect to this particular case. The reasonable assumption that $\omega + \omega_F \cong 2\omega$ will thus be made, obtaining the BLDO approximation [24] for a single-tuned resonator:

$$\mathbf{Z}_F \doteq \frac{R_F}{1 + j2Q_F \dfrac{(\omega - \omega_F)}{\omega_F}} \tag{3.8}$$

Using (3.8) in (3.6) and rearranging, we obtain the in-line equation:

$$\begin{aligned}(\omega_F + 2Q_F\,(j\omega - j\omega_F) + \omega_F\,R_F\,G_N[V_I]) \cdot V_I\,e^{j\phi_I} = \\ (\omega_F + 2Q_F\,(j\omega - j\omega_F)) \cdot V_G\,e^{j\phi_G}\end{aligned} \tag{3.9}$$

which analytically defines *steady state* (SS) values of V_I and ϕ_I as a function of the injection signal amplitude V_G, phase ϕ_G and frequency ω. To work out the differential system model we can follow an analogous procedure, in view of the theory presented in [24], simply by replacing every jω term with its symbolic counterpart (jω + d/dt) and then performing the necessary calculations. This way, we firstly get:

$$\begin{aligned}&2Q_F\,V_I^{'}[t]\,e^{j\phi_I[t]} + (\omega_F + j2Q_F\,(\omega - \omega_F) + \omega_F\,R_F\,G_N[V_I[t]] + j2Q_F\phi_I^{'}[t]) \cdot \\ &\cdot V_I[t]\,e^{j\phi_I[t]} = e^{j\phi_G[t]}\,(2Q_F V_G^{'}[t] + (\omega_F + j2Q_F\,(\omega - \omega_F) + j2Q_F\phi_G^{'}[t])V_G[t])\end{aligned} \tag{3.10}$$

Splitting it into a real and an imaginary equation and rearranging, the normal form of differential set of equations is obtained:

$$\begin{aligned}V_I^{'}[t] = \frac{1}{2Q_F}\Big(&V_G[t]\,\big(2Q_F\,\sin[\Delta\phi_{IG}[t]](\Delta\omega + \phi_G^{'}[t]) + \omega_F\,\cos[\Delta\phi_{IG}[t]]\big) + \\ &- \omega_F\,(1 + R_F\,G_N[V_I[t]])\,V_I[t]\Big) + \cos[\Delta\phi_{IG}[t]]\,V_G^{'}[t]\end{aligned} \tag{3.11a}$$

$$\begin{aligned}\phi_I^{'}[t] = \frac{1}{2Q_F V_I[t]}&\Big(V_G[t]\,\big(2Q_F\,\cos[\Delta\phi_{IG}[t]](\Delta\omega + \phi_G^{'}[t]) - \omega_F\,\sin[\Delta\phi_{IG}[t]]\big)\Big) + \\ &-\left(\Delta\omega + \sin[\Delta\phi_{IG}[t]]\,\frac{V_G^{'}[t]}{V_I[t]}\right)\end{aligned} \tag{3.11b}$$

In above equations, $\Delta\phi_{IG} = \phi_I[t] - \phi_G[t]$ and $\Delta\omega = \omega - \omega_F$ definitions have been used. Differential system (3.11) fully describes the transient evolution of the $\mathbf{V}_I$

variable, once $G_N[V_I[t]]$ describing function, $\{Q_F, \omega_F, R_F\}$ circuit parameters and $\{\omega, V_G[t], \phi_G[t], V_G'[t], \phi_G'[t]\}$ injection functions are known.

Under free-run conditions ($\mathbf{V}_G[t] = 0$), the steady-state oscillation values are easily obtained from (3.10), resulting in:

$$V_{I,OSC} \cdot \left(\omega_F + j2Q_F(\omega_{OSC} - \omega_F) + R_F\,\omega_F\,G_N[V_{I,OSC}]\right) = 0 \tag{3.12a}$$

$$\begin{cases} G_N[V_{I,OSC}] = -\dfrac{1}{R_F} \\ \omega_{OSC} = \omega_F \end{cases} \tag{3.12b}$$

In this simple case, an analytical solution can be found even without the need to describe the analytical form of the SIDF, but this is not a general rule, e.g., in oscillators with more reactive components there are two possibilities: or a full definition of the $G_N[V_I[t]]$ is given, or the second of these equations is not gained.

As a simplified example, useful for a better understanding of the involved phenomena, it is convenient to study the specific case of a *continuous wave* (CW) injection. Formulas (3.11) reduce to two simpler equations:

$$V_I'[t] = V_{G,CW}\left(\Delta\omega \sin[\phi_I[t]] + \frac{\omega_F}{2Q_F}\cos[\phi_I[t]]\right) - \frac{\omega_F}{2Q_F}\left(1 + R_F G_N[V_I[t]]\right) V_I[t] \tag{3.13a}$$

$$\phi_I'[t] = -\Delta\omega + \frac{V_{G,CW}}{V_I[t]}\left(\Delta\omega \cos[\phi_I[t]] - \frac{\omega_F}{2Q_F}\sin[\phi_I[t]]\right) \tag{3.13b}$$

where $\phi_{G,SS}$ has been set to zero for sake of compactness, i.e., used as phase reference.

In this process of particularization under specific conditions, special attention deserves the low-level injection hypothesis. That is, if we assume that a small $V_{G,CW}$ voltage is applied to the free-running oscillator, then only a small perturbation come out in all oscillator's variable quantities. In this perturbation theory, an "order of smallness" ε must be introduced. A convenient choice for its magnitude is the inverse of the Q factor of the resonator, when applicable.

In example of Fig. 3.3, this considerations lead to the selection of $\varepsilon = 1/Q_F$. For example, if a $V_{G,CW} = O[\varepsilon]$ drive voltage is injected into the ILO, then we obtain $V_I[t] = V_{I,OSC} + \Delta V_I[t]$, where $\Delta V_I[t]$ results in an ε smallness.

Now, for the purpose of deducing the corresponding LLI system to (3.13), we will suppose the following smallness conditions, which are the ones producing equations of the same structure of - and very similar to - classical Adler's ones [26]:

$$\begin{aligned} & Q_F = O[\varepsilon^{-1}] \\ & V_{G,CW} = O[\varepsilon] \\ & \Delta\omega = O[\varepsilon^2] \\ & \Delta V_I[t] = O[\varepsilon]; \qquad \Delta V_I'[t] = O[\varepsilon^3] \\ & \phi_I[t] = O[1]; \qquad \phi_I'[t] = O[\varepsilon^2] \end{aligned} \tag{3.14}$$

These equations, together with series approximation of $G_N[V_I[t]] \cong G_N[V_{I,OSC}] + G_N'[V_{I,OSC}]\cdot\Delta V_I[t]$, lead to the following LLI CW dynamical complex envelope domain system:

$$\Delta V_I[t] = \frac{V_{G,CW}\cos[\phi_I[t]]}{R_F\, V_{I,OSC}\, G_N'[V_{I,OSC}]} \tag{3.15a}$$

$$\phi_I'[t] = -\Delta\omega - \frac{V_{G,CW}}{V_{I,OSC}}\cdot\frac{\omega_F}{2Q_F}\sin[\phi_I[t]] \tag{3.15b}$$

It is to be noted that this algebraic-differential system is a well known result in literature [24,26,27,50–53]. This can be successfully employed for the stability evaluation, but it is not always accurate to reproduce transitory evolution of the circuit. For that purpose, full unconstrained system (3.13) should be used. We will deepen this argument in Section 3.4.

3.3 Class Defining Conditions

Before proceeding further, it is convenient to summarize some relevant aspects. For argument's sake, it has been preferred to introduce this treatment exploiting a precise example, whose peculiarities are especially well-known and clear, for the purpose of making easy to understand the theoretical structure and standard sequence of the general approach, as well as the adopted nomenclature for variables in use.

Now, we will clarify the limits and the conditions an injection-locked oscillator must satisfy in order to be treatable with this analysis method in the dynamical complex envelope domain.

This class can be basically identified as the class of "properly designed" fundamental-mode ILOs, i.e., systems based on a quasi-sinusoidal (unimodal and self-starting) "core-oscillator" driven by a narrowband-modulated injection signal, with a carrier frequency quite close to the free-run oscillation one.

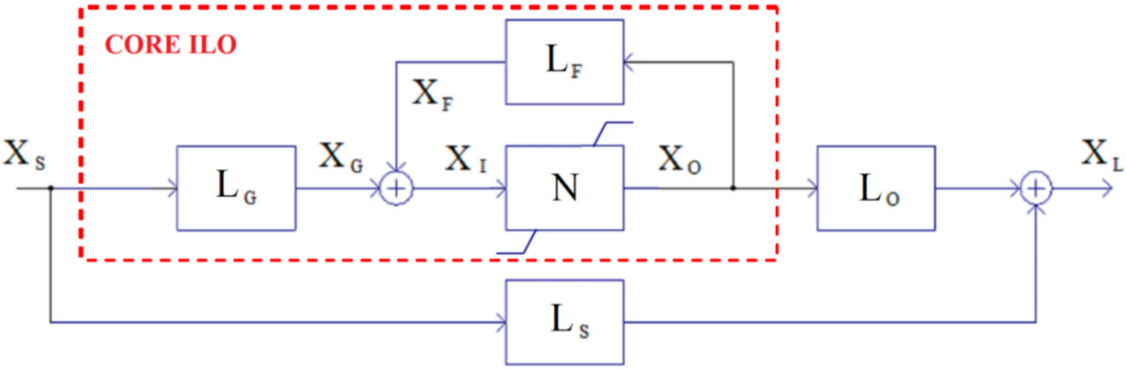

Fig. 3.4 – Phasor-domain block-diagram of the generic driven oscillator system considered.

The generalized system under analysis is represented in Fig. 3.4, where a larger number of blocks are available in comparison with Fig. 3.2. The nonlinear element is now represented by an "**N**" symbol, meaning it can be different from a simple negative conductance (as in previous example was). Therefore, its control and controlled variables are now generic $\mathbf{X}_I/\mathbf{X}_O$ signals, instead of $\mathbf{V}_I/\mathbf{I}_O$, respectively. In the generic case, the transfer function in the feedback loop is described by the linear block $\mathbf{L}_F$.

In figure is highlighted the "core ILO", which is the main part involved in the determination of oscillators' behavior. It includes the linear block $\mathbf{L}_G$, which takes into account the possibility that injection $\mathbf{X}_S$ can be of a different type with respect of $\mathbf{X}_I$, for example injected variable is a current while nonlinear element is voltage controlled. Also, it can represent an additional filtering behavior of the circuit under test.

Last two linear blocks in figure, $\mathbf{L}_O$ and $\mathbf{L}_S$, have been added in order to take into account for a generic output variable $\mathbf{X}_L$ that the user may want to analyze. Since it can be directly influenced by the drive signal, the linear block $\mathbf{L}_S$ have been included, too.

All these four $\mathbf{L}_X$ blocks represent the various time-invariant, passive and linear elements of the system, properly grouped. Furthermore, $\mathbf{L}_F$ block must reproduce a high selectivity resonant filter. In first example detailed in previous section, a single tuned has been taken, and $\mathbf{L}_F$ was the (approximated) impedance of a second order resonator. When a higher order is given, different possibilities can present. In many practical cases, main resonator is well-approximable as a single tuned, and is therefore called a "single-tuned like". Otherwise, a more complicated model needs to be considered, as we will see in chapter 6.

About nonlinear (active) elements, they must be all collectable inside the only nonlinear block $\mathbf{N}[X_I]$. In Section 3.2 we have considered one single nonlinear bipole (a simplified tunnel diode) characterized by a real function, but in the most general case a series of nonlinear devices, including parasitic effects (i.e., producing a complex function), can be appropriately modeled. The main limitation is the assumption of a single control variable for the nonlinear active device (or for the system block), but this constraint can be considered a reasonable approximation in many feedback-type high-frequency TILOs designed exploiting modular/matched structures, and nearly unilateral active devices.

Notice that the use of the SIDF, and its extensions that will be introduced in the following, in the circuital context usually assumes that variations of the active device bias in the various operating conditions investigated is negligibly small or none. A discussion and an example in the case of shifting of the bias point will be treated in chapter 4.

The injection is supposed to be a slowly-varying quantity, both in amplitude and phase, narrowband-modulated with a carrier in the neighborhood of the free-run oscillation frequency. Amplitude of drive voltage is usually assumed to be of an order of magnitude not greater than oscillation voltage, though this will be more precisely discussed in the following.

3.4 Describing Function and Transient Analysis

From DCE equations (3.11) or (3.13), transient responses can be evaluated with very high computational efficiency, via standard numerical integration methods. For the sake of simplicity, we will refer to example exposed in Section 3.2.

The nonlinear conductance there adopted, will be here represented with a polynomial, in particular through a standard cubic model. Easy as it may appear, it is often not well documented, thus we will briefly summarize its usage before proceeding. The appellation "cubic" refers to time domain model, and actualizes in the definition of this voltage controlled element, where $P_N = 3$:

$$i_O[t] = \sum_{p=0}^{P_N} g_{Np} v_I[t]^p = g_{N0} + g_{N1} v_I[t] + g_{N2} v_I[t]^2 + g_{N3} v_I[t]^3 \tag{3.16}$$

Applying a sinusoidal voltage $v_I[t] = V_I[t] \cdot \cos[\omega t + \phi_I]$, and grouping all terms with reference to different frequencies, we obtain:

$$\begin{aligned} i_O[t] &= (g_{N0} + \frac{1}{2} g_{N2} V_I^2) + (g_{N1} V_I + \frac{3}{4} g_{N3} V_I^3) \cos[\omega t + \phi_I] + \\ &+ (\frac{1}{2} g_{N2} V_I^2) \cos[2(\omega t + \phi_I)] + (\frac{1}{4} g_{N3} V_I^3) \cos[3(\omega t + \phi_I)] \end{aligned} \tag{3.17}$$

where all V_I and ϕ_I are slowly varying functions of the time, but it has been omitted for a better readability. Please note that g_{N0} must be zero in order to represent a realistic passive element, with no current when zero voltage is applied.

Since we want to consider the fundamental harmonic only, we need to exclude both the constant term and higher harmonics. Hence, passing from the time domain to the frequency domain:

$$\begin{aligned} & i_{O,FUND}[t] = G_N[V_I[t]] \cdot V_I[t] \cdot \cos[\omega t + \phi_I] \\ & \mathbf{I}_O[t] = G_N[V_I[t]] \cdot \mathbf{V}_I[t] \\ & G_N[V_I[t]] = g_{N1} + \frac{3}{4} g_{N3} V_I^2 \end{aligned} \tag{3.18}$$

Finally, subdividing this SIDF with another polynomial representation, but in the phasor domain, we get:

$$
\begin{aligned}
& G_N[V_I[t]] = \sum_{p=0}^{P_N-1} G_{Np} \cdot V_I[t]^p = G_{N0} + G_{N1} V_I[t] + G_{N2} V_I[t]^2 \\
(3.19) \qquad & G_{N0} = g_{N1} \\
& G_{N1} = 0 \\
& G_{N2} = \frac{3}{4} g_{N3}
\end{aligned}
$$

Therefore, the fundamental mode of a (time-domain) cubic model is completely defined by G_{N0} and G_{N2} coefficients.

It is now possible to introduce (in Tab. 3.1) all numerical values employed for circuit parameters in following transient evolutions:

$\omega_F = 10^9$ rad/s	$G_{N0} = -2$ mS
$Q_F = 100$	$G_{N1} = 0$
$R_F = 1$ kΩ	$G_{N2} = 1$ mS/V^2

Tab. 3.1 – Numerical values for example of Sec. 3.2, employed in following transient graphics

To evaluate a transient response from obtained differential system, the operative procedure is quite straightforward. Since the set of equations (3.13) is not solvable in analytical closed form, numerical integration will be required to calculate the output waveform evolution. Driving the oscillator with a simple signal in continuous wave, introduced at time t = 0, the standard procedure requires to:

1) set injection conditions (i.e. ω, V_G);
2) set an initial condition (i.e. $\mathbf{V}_{I,0} \equiv \mathbf{V}_I [t]|_{t=0}$), which can be the free-running oscillation regime, for example;

3) insert all above specified numerical conditions into the DCE system, and solving it numerically. In this research, this has been accomplished with the software Wolfram Mathematica [54].

Please note that steady-state values ($V_{I,SS}$, $\phi_{I,SS}$) can be easily obtained by means of those equations, by setting $V_I'[t] = \phi_I'[t] = 0$.

For comparison reasons, simulations performed with (3.15) LLI equations have been provided also in figures, showing that, in some cases, an excessive approximation results from those ones, as previously stated.

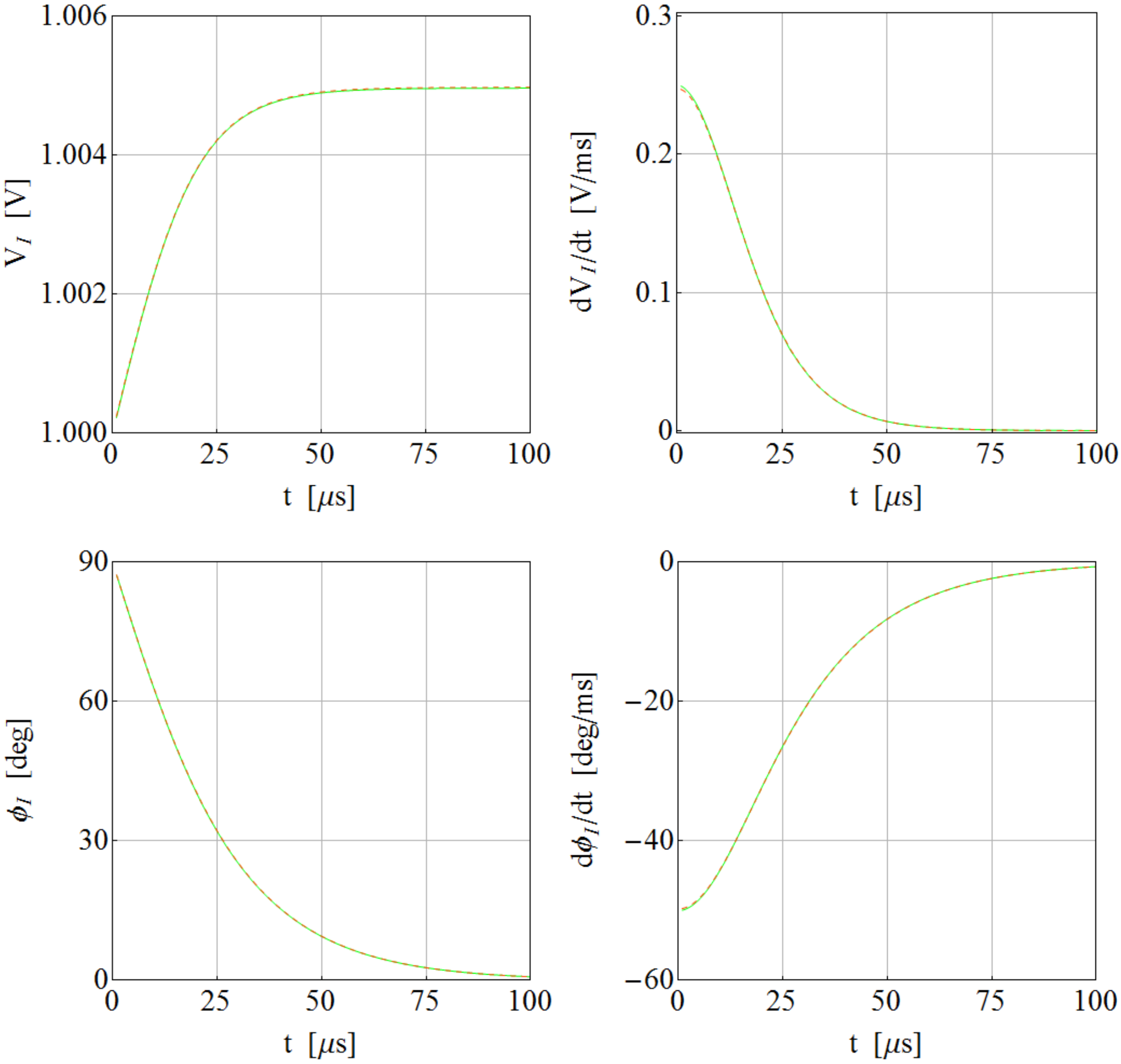

Fig. 3.5 – Transient evolution of $V_I[t]$, $V_I'[t]$, $\phi_I[t]$, $\phi_I'[t]$ in the circuit of Fig. 3.3, when driven by $V_G = 10$ mV, $\omega = \omega_F$, starting from oscillation conditions ($V_{I,0} = 1$ V, $\phi_{I,0} = 90$ deg); solution of full system is green, of LLI system is dashed orange.

First simulation, depicted in Fig. 3.5, illustrates the transient evolution of the circuit under test when the injection is suddenly activated starting from the oscillation condition. In particular, $V_{I,OSC}$ = 1 V, V_G = 10 mV, $\omega = \omega_F = \omega_{OSC}$, resulting in steady state value $V_{I,SS} \cong 1.005$ V. In the four frames represented, $V_I[t]$, $V_I'[t]$, $\phi_I[t]$, $\phi_I'[t]$ are shown, respectively.

In this case, LLI approximation produces nearly the same results of the complete solution, that is a common exponential behavior.

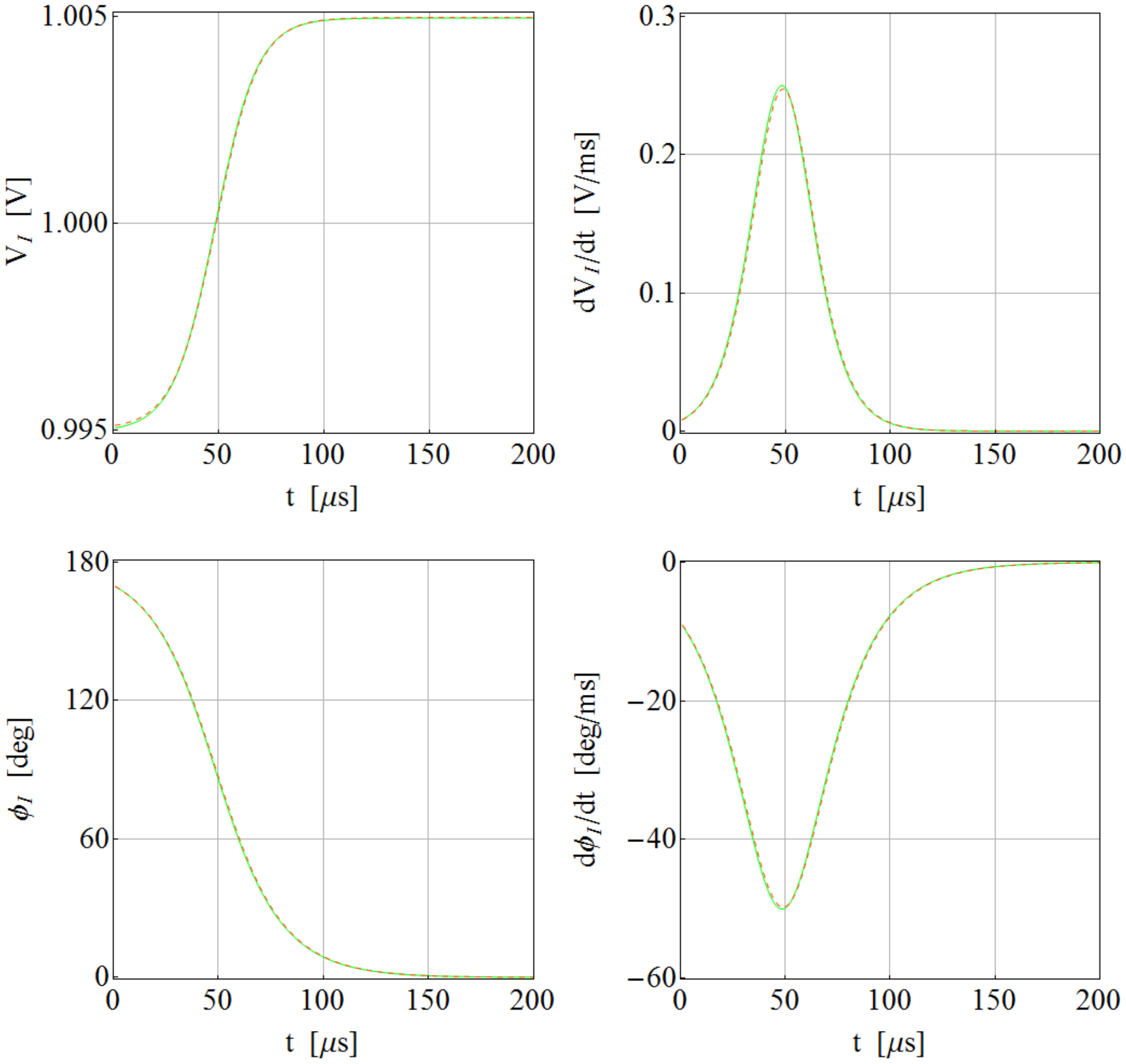

Fig. 3.6 – Transient evolution of $V_I[t]$, $V_I'[t]$, $\phi_I[t]$, $\phi_I'[t]$ in the circuit of Fig. 3.3, when driven by V_G = 10 mV, $\omega = \omega_F$, starting from conditions $V_{I,0}$ = 0.995 V, $\phi_{I,0}$ = 170 deg; solution of full system is green, of LLI system is dashed orange.

When starting condition is not the free-running oscillation regime, a more complicated evolution can be exhibited. The case of a lower initial amplitude, and more distant phase from its steady-state value, is shown in Fig. 3.6, where $V_{I,0} = 0.995$ V, $\phi_{I,0} = 170$ deg.

This time, two time constant are visible. Both amplitude and phase of $\mathbf{V}_I[t]$ exhibit a double exponential behavior, well indicated by their bell-shaped derivatives graphics, too.

However, a very fast initial transient is also present but not evident from those graphics. During this time interval, amplitude shows a (small) falling and rising

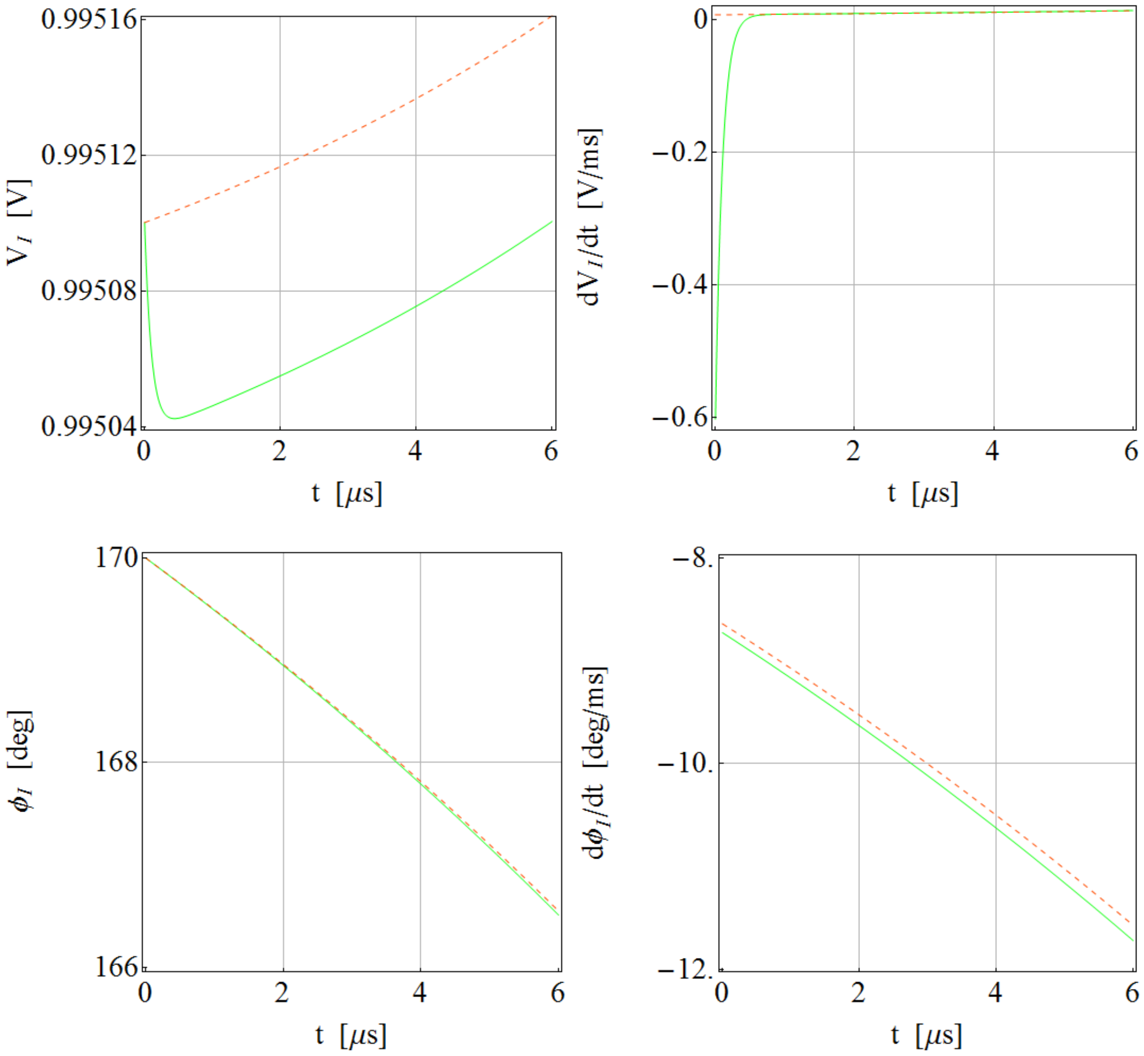

Fig. 3.7 – Transient evolution of $V_I[t]$, $V_I'[t]$, $\phi_I[t]$, $\phi_I'[t]$ in the circuit of Fig. 3.3, when driven by $V_G = 10$ mV, $\omega = \omega_F$, starting from conditions $V_{I,0} = 0.995$ V, $\phi_{I,0} = 170$ deg; solution of full system is green, of LLI system is dashed orange.

evolution, which is not caught by LLI equations, since the order of the corresponding algebraic-differential system is too low. That is, derivative of the magnitude is different at the beginning, as highlighted by the upper right frame of Fig. 3.7. Phase trend has no such trend, instead.

Let's consider detuned injections cases now. When the angular frequency of the drive voltage is 30 krad/s higher than free-running oscillation, an overshoot in nonlinear conductance's amplitude is exhibited, and correctly represented by both

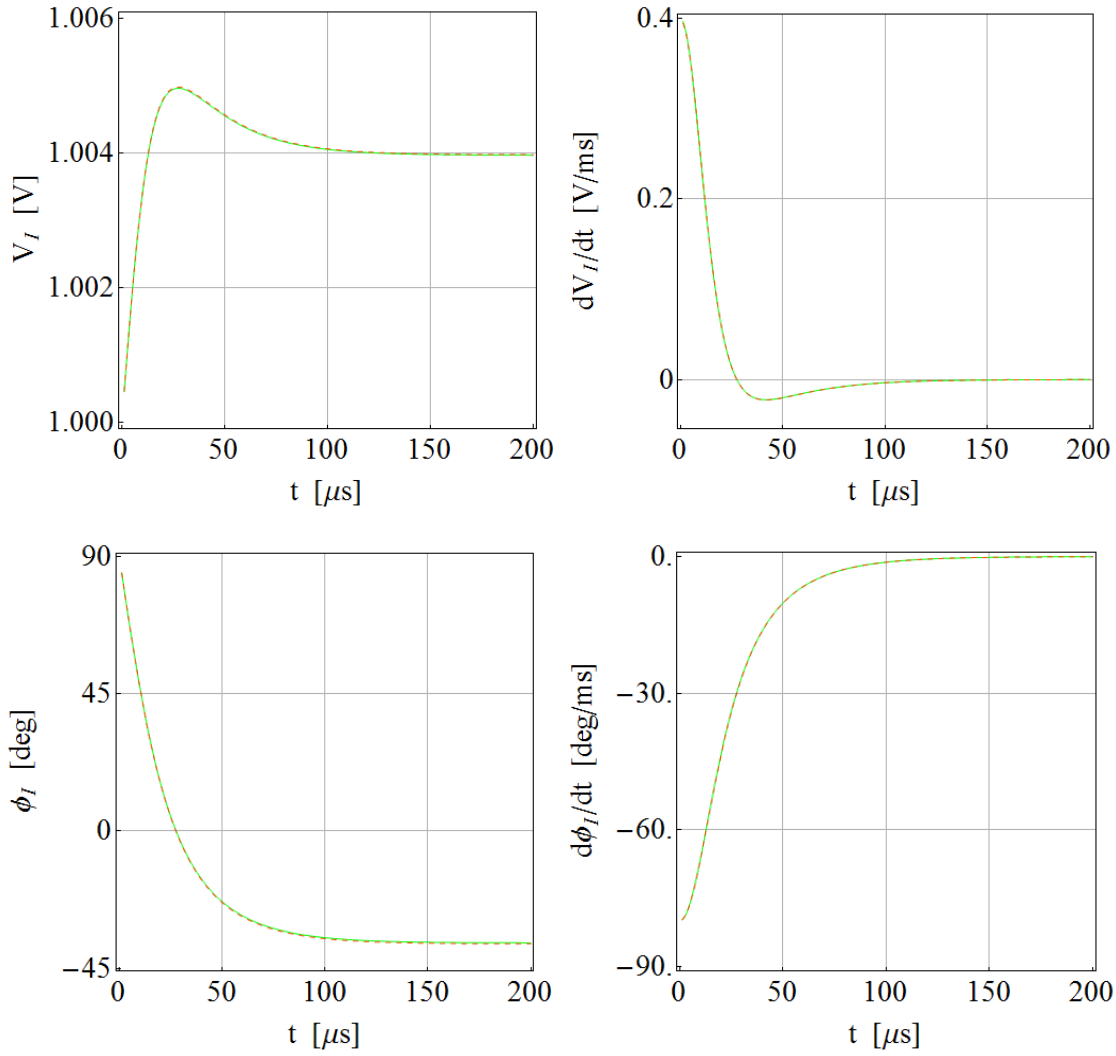

Fig. 3.8 – Transient evolution of $V_I[t]$, $V_I'[t]$, $\phi_I[t]$, $\phi_I'[t]$ in the circuit of Fig. 3.3, when driven by $V_G = 10$ mV, $\omega = \omega_F + 30$krad/s, starting from oscillation conditions ($V_{I,0} = 1$ V, $\phi_{I,0} = 90$ deg); solution of full system is green, of LLI system is dashed orange.

full and LLI analyses. Fig. 3.8 shows that its derivative feature an overshoot too, while it is to be noted that steady-state value of the phase is not zero any more.

This detuning width is approximately 60% of the bandwidth calculated at that injection level.

With a detuning width exceeding the bandwidth (e.g., 120% of it, like in Fig. 3.9), the unlocked state is obtained. In this case, no steady-state regime can be reached by the amplitude or by the phase, but it is revealed a periodic movement of $V_I[t]$ and $\phi_I[t]$. It matches with a non-sinusoidal oscillation of the envelope of $v_I[t]$ in

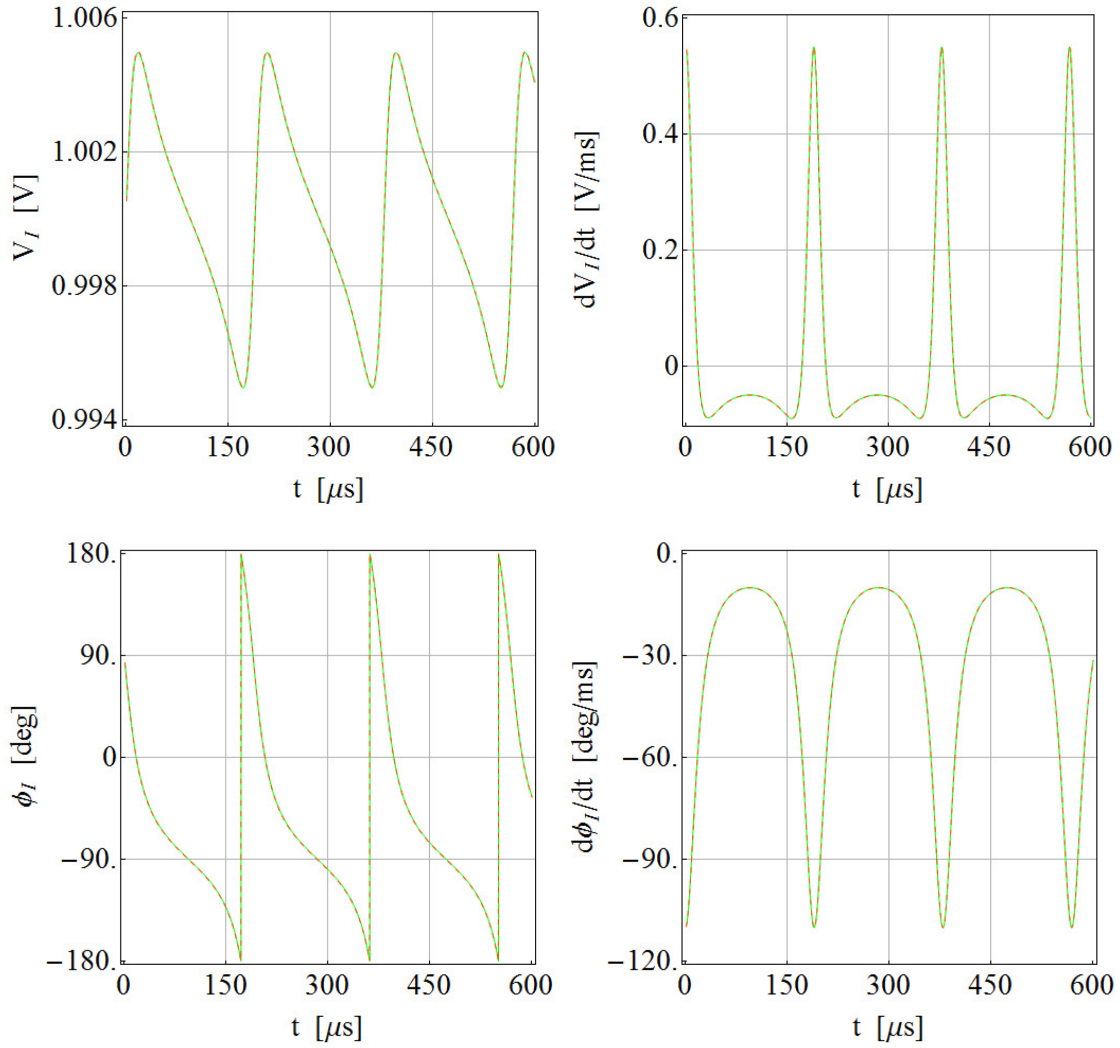

Fig. 3.9 – Transient evolution of $V_I[t]$, $V_I'[t]$, $\phi_I[t]$, $\phi_I'[t]$ in the circuit of Fig. 3.3, when driven by V_G = 10 mV, $\omega = \omega_F + 60krad/s$, starting from oscillation conditions ($V_{I,0}$ = 1 V, $\phi_{I,0}$ = 90 deg); solution of full system is green, of LLI system is dashed orange.

the time domain, therefore no sinusoidal regime is achieved. Obviously, respective derivatives have a periodic evolution, too.

As pointed out by this figure, both full system (3.13) and LLI system (3.15) are able to correctly illustrate the transient evolution in case of an unlocked state.

As last example, a free-running oscillation is shown, starting from a zero condition, (i.e., startup transient evolution). This event is different from previous ones, in fact it is not possible to define any phase evolution, since there is no injected signal to use as a reference. Moreover, LLI equations (3.15) cannot be applied in this case, since they would provide only a constant value both for $\mathbf{V}_I[t]$ amplitude and phase, i.e., no evolution at all.

In Fig. 3.10 the startup evolution of present test circuit is reproduced, with both $V_I[t]$ and $V_I'[t]$ being displayed.

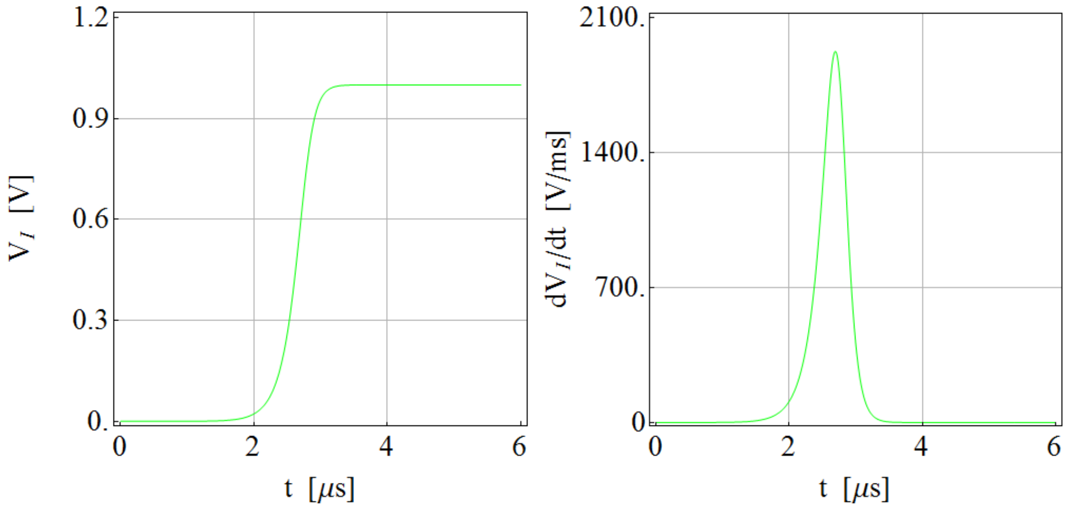

Fig. 3.10 – Free-running startup transient evolution (i.e., $V_{I,0} = 0$) of $V_I[t]$, $V_I'[t]$, in the circuit of Fig. 3.3.

Indeed, since the zero solution is mathematically a possible one, a small perturbation to the initial condition had to be added (in particular, a 1 µV voltage), whose role is the same played by background noise in real oscillators, in order to let the signal move from its initial state.

3.5 Dynamical Stability Analysis

First of all, we need to analytically define the steady-state system, obtainable from the (3.13) equations, setting $V_I'[t] = \phi_I'[t] = 0$, still focusing on the specific case of a single-tuned (or single-tuned like) oscillator. Solving for $\cos[\phi_{I,SS}]$ and $\sin[\phi_{I,SS}]$ and after some rearrangements we get:

$$\left(1+\frac{R_F\,\omega_F^2\,G_N[V_{I,SS}]\,(2+R_F\,G_N[V_{I,SS}])}{4Q_F^2\Delta\omega^2+\omega_F^2}\right)V_{I,SS}^2=V_{G,CW}^2 \tag{3.20a}$$

$$\sin\left[\phi_{I,SS}\right]=\frac{2Q_F\,R_F\,V_{I,SS}\,\Delta\omega\,\omega_F\,G_N[V_{I,SS}]}{V_{G,CW}(4Q_F^2\Delta\omega^2+\omega_F^2)} \tag{3.20b}$$

These equations are decoupled, the first being the only needed to evaluate $V_{I,SS}$, while the second permits to evaluate $\phi_{I,SS}$ substituting the solution provided by the previous one. However, equation (3.20a) cannot be solved in $V_{I,SS}$ in its general form until the SIDF is not defined. In the case of a cubic polynomial, it develops into a "fake sixth-degree" equation, that is a third-order equation in the variable $V_{I,SS}^2$:

$$\begin{aligned}&(G_{N2}^2\,R_F^2\,\omega_F^2)\,V_{I,SS}^6+\big(2\,G_{N2}\,R_F\,\omega_F^2(1+G_{N0}\,R_F)\big)V_{I,SS}^4+\\&+\big(4Q_F^2\Delta\omega^2+(\omega_F+G_{N0}R_F\omega_F)^2\big)V_{I,SS}^2-(4Q_F^2\Delta\omega^2+\omega_F^2)\,V_{G,CW}^2=0\end{aligned} \tag{3.21a}$$

$$\sin\left[\phi_{I,SS}\right]=\frac{2Q_F\,R_F\,V_{I,SS}\,\Delta\omega\,\omega_F\,(G_{N0}+G_{N2}V_{I,SS}^2])}{V_{G,CW}(4Q_F^2\Delta\omega^2+\omega_F^2)} \tag{3.21b}$$

which provides three acceptable solutions, since negative values are meaningless for the magnitude $V_{I,SS}$.

As already stated, locking-bandwidth (LBW) is one of the principal features of an injection-locked oscillator. Steady-state equation provides, in general, more than one solution, i.e., more than one possible regime, as shown in the (3.21) example. To ascertain if a given equilibrium point, calculated by the fundamental mode spectral balance equation under CW injection, corresponds to locked or unlocked regime, a dynamical stability analysis has to be carried out. We will equivalently name them stable and unstable points, respectively.

Stability analysis can be performed with standard Routh-Hurwitz criterion [55], after the first step of evaluating the characteristic polynomial of the Jacobian Matrix. This method is generally faster than direct eigenvalues calculus, but there are alternatives that can ease the evaluation of the local stability conditions, as we will describe in the following.

In order to simplify the exposition, it is often convenient to refer to a specific example, therefore part of the treatment will be related to circuit of Fig. 3.3, where the order of the system is N=1.

Calculation of the (2N)×(2N) Jacobian Matrix is supported by the form of (3.13) differential equations, permitting a standard local linearization technique [56,21], in the $\{V_{I,SS}, \phi_{I,SS}\}$ specific point under test. In particular, defining:

(3.22a)
$$f_1[V_{I,SS}, \phi_{I,SS}] = V_{G,CW}\left(\Delta\omega \sin[\phi_{I,SS}] + \frac{\omega_F}{2Q_F}\cos[\phi_{I,SS}]\right) + \\ -\frac{\omega_F}{2Q_F}\left(1 + R_F G_N[V_{I,SS}]\right) V_{I,SS}$$

(3.22b)
$$f_2[V_{I,SS}, \phi_{I,SS}] = -\Delta\omega + \frac{V_{G,CW}}{V_{I,SS}}\left(\Delta\omega \cos[\phi_{I,SS}] - \frac{\omega_F}{2Q_F}\sin[\phi_{I,SS}]\right)$$

The general form of the Jacobian Matrix, in the case of a first-order differential system, is:

(3.23)
$$\underline{\underline{J}} = \begin{bmatrix} J_{11} & J_{12} \\ J_{21} & J_{22} \end{bmatrix} = \begin{bmatrix} \dfrac{\partial f_1}{\partial V_{I,SS}} & \dfrac{\partial f_1}{\partial \phi_{I,SS}} \\ \dfrac{\partial f_2}{\partial V_{I,SS}} & \dfrac{\partial f_2}{\partial \phi_{I,SS}} \end{bmatrix}$$

therefore, substituting from (3.22) and performing the derivatives, we obtain:

$$
\begin{aligned}
J_{11} &= -\frac{\omega_F}{2Q_F}\left(1 + R_F G_N[V_{ISS}] + R_F V_{ISS} G_N{}'[V_{ISS}]\right)\\
J_{12} &= V_{G,CW}\left(\Delta\omega \cos[\phi_{I,SS}] - \frac{\omega_F}{2Q_F}\sin[\phi_{I,SS}]\right)\\
J_{21} &= -\frac{V_{G,CW}}{V_{I,SS}{}^2}\left(\Delta\omega \cos[\phi_{I,SS}] - \frac{\omega_F}{2Q_F}\sin[\phi_{I,SS}]\right)\\
J_{22} &= -\frac{V_{G,CW}}{V_{I,SS}}\left(\Delta\omega \sin[\phi_{I,SS}] + \frac{\omega_F}{2Q_F}\cos[\phi_{I,SS}]\right)
\end{aligned}
\tag{3.24}
$$

The corresponding characteristic polynomial, whose roots ascertain the eigenvalues whose values determine the circuit's time response to a perturbation of the analyzed equilibrium point, is:

$$
p_C = \det[\lambda \cdot \underline{\underline{I}}_{(2N)\times(2N)} - \underline{\underline{J}}] = \sum_{n=0}^{2N} p_n \cdot \lambda^n = p_2\lambda^2 + p_1\lambda + p_0
\tag{3.25}
$$

where in last equivalence N = 1 has been set. Also, note that p_{2N} is a structural unity, when its calculation is performed through the steps here described. In this single-tuned example, the other two terms result:

$$
\begin{aligned}
p_1 &= \frac{V_{G,CW}}{V_{I,SS}}\Delta\omega \sin[\phi_{I,SS}] + \\
&\quad + \frac{\omega_F}{2Q_F}\left(1 + R_F\, G_N[V_{I,SS}] + R_F V_{I,SS} G_N{}'[V_{ISS}] + \frac{V_{G,CW}}{V_{I,SS}}\cos[\phi_{I,SS}]\right)\\
p_0 &= \left(\left(\Delta\omega \cos[\phi_{I,SS}] - \frac{\omega_F}{2Q_F}\sin[\phi_{I,SS}]\right)\frac{V_{G,CW}}{V_{I,SS}}\right)^2 + \\
&\quad + \frac{\omega_F}{2Q_F}\left(\Delta\omega \sin[\phi_{I,SS}] + \frac{\omega_F}{2Q_F}\cos[\phi_{I,SS}]\right)\cdot\\
&\quad \cdot \left(1 + R_F\, G_N[V_{I,SS}] + R_F\, V_{I,SS}\, G_N{}'[V_{I,SS}]\right)\cdot\frac{V_{G,CW}}{V_{I,SS}}
\end{aligned}
\tag{3.26}
$$

The (3.26) coefficients here calculated depends on both amplitude and phase of the point under test, but it is possible to remove dependence on the phase substituting the solution in sin[$\phi_{I,SS}$] and cos[$\phi_{I,SS}$], mentioned at the beginning of this section. The results will not depend on $V_{G,CW}$ either:

$$\text{(3.27)}\qquad \begin{aligned} p_1 &= \frac{\omega_F}{2Q_F}\left(2 + 2\, R_F\, G_N[V_{ISS}] + R_F\, V_{ISS}\, G_N'[V_{ISS}]\right) \\ p_0 &= \Delta\omega^2 + \left(\frac{\omega_F}{2Q_F}\right)^2 (1+R_F\, G_N[V_{ISS}])(1+R_F\, G_N[V_{ISS}]+R_F V_{ISS} G_N'[V_{ISS}]) \end{aligned}$$

Those coefficients are crucial for stability analysis. In fact, in many cases they can provide complete information without the need of solving the characteristic polynomial. As anticipated before, evaluation of eigenvalues is not required, as any other standard method (e.g., Routh-Hurwitz) providing equivalent information can be conveniently adopted.

On the other hand, if a global picture of the LBW-related characteristics of the analyzed system is aimed at, avoiding repeated single-point analyses, one can directly look for the stability surfaces in the response space $\{V_{G,CW}, \Delta\omega, V_{I,SS}\}$. To this purpose, in most common cases one can take advantage of the generalized definition of Locus and Boundary introduced in [21] which identify two cylindrical surfaces (curves in the plane $\{\Delta\omega, V_{I,SS}\}$), that, in combination, define a subset of the boundary borders between stable and unstable locking regions. In fact, they permit adequate investigation of both the *principal* locking band (i.e., the one surrounding the free-run oscillation frequency with step-continuous dependence on $V_{G,CW}$) or the *lateral* bands (those associated to hysteresis phenomena) which involve only the stability manifolds covered by Locus or Boundary (see Sec. 3.6 for more information). Their use alone, i.e., without the support of a complete stability analysis through Routh-Hurwitz or equivalent method, is critical only for the evaluation of *isolated* locking bands, which are sometimes erroneously predicted by Locus or Boundary (see Appendix A2 for more information).

In the first-order example under investigation, conditions introduced by Locus and Boundary limits are respectively represented by:

$$\begin{cases} p_0 > 0 & \textit{(Locus condition)} \\ p_1 > 0 & \textit{(Boundary condition)} \end{cases} \tag{3.28}$$

A graphical interpretation of these two conditions in the $\{\Delta\omega, V_{I,SS}\}$ plane will point out the advantages they supply. Both the requirements must be met, therefore the stability is observed in the unshaded region of Fig. 3.11, where unstable regions ($p_0 < 0$ and $p_1 < 0$) are colored in light red.

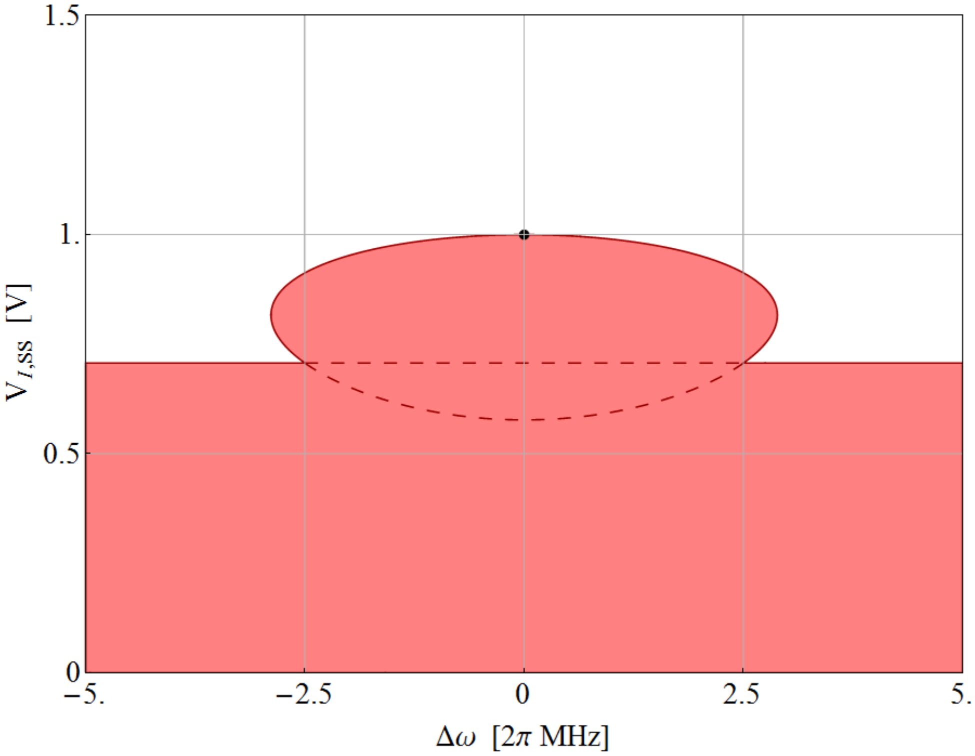

Fig. 3.11 – Stability plane for first-order example of Fig 3.3. Boundary limit is the straight line at 0.707 V, Locus limit is the elliptic-like curve. The black dot corresponds to the free-running oscillation.

In this figure some elements might be observed. First, regions in red provide the set of unstable points. It means that every couple $\{\Delta\omega, V_{I,SS}\}$ falling inside the shaded area, is not a possible steady-state solution. The oscillator can be somehow driven to one of these points, but it will leave that position as soon as it is able. Please note that stability borders are only the straight lines, while dashed ones are only provided as a graphical reference, indicating Locus and Boundary respective borders.

The Boundary limit is a horizontal line, i.e., it is not a function of the detuning $\Delta\omega$. That is, it does not depend on injection frequency. This is not a general result, but in most examples its trend is a weak function of the detuning, especially in comparison with the Locus limit. This latter one, exhibiting in Fig. 3.11 an elliptic-like shape, is actually the only one involved in case of a low-level injection. In fact, when drive voltage is small, steady-state value of the nonlinear voltage will be in the neighborhoods of the oscillation value, that is the black dot depicted in figure. Only with a *high level injection* (HLI), possible regimes will be influenced by the Boundary limit, as we will see in next section.

From a practical point of view, the free-running stability must be calculated before the steady-state one, obviously. In this case, with a single free-run oscillating solution, it is likely that it is stable, but a check must be performed.

The straightest way to ensure the stability, is to evaluate eigenvalues in the specific point, excluding the null eigenvalue $\lambda = 0$, corresponding to the positioning on the Locus itself. This characteristic is a general one. In the described example, substituting oscillation values to the characteristic polynomial, lead to $\lambda_1 = -10^7$, which, being its real part negative, confirms the stability of the free-running oscillation point obtained. If characteristic polynomial is not easy to solve (e.g., it is of an high degree, and numerical estimation is not a viable opportunity), then Routh-Hurwitz criterion could be carried out, for example.

In other cases more than one oscillation point can be provided from the DCE equations (after appropriate conditions have been set), and a stability analysis is necessary for everyone of these solutions.

3.6 Steady-State Curves and Locking Bandwidth

Stability regions are especially useful to understand circuit's behavior and locking/unlocking transitions when steady-state regimes are superimposed.

Those latter ones correspond to points in the stability plane that can be obtained solving numerically the (3.20) regime DCE system, once a $\{\Delta\omega, V_{G,CW}\}$ couple has been chosen. By means of the second equation, the steady-state phase can be determined, too.

It is especially meaningful to reproduce in that plane a steady-state curve, achieved with the numerical choice of a fixed $V_{G,CW}$ and sweeping the frequency detuning as a parameter. The intersection between a steady-state curve and stability borders do provide the locking bandwidth.

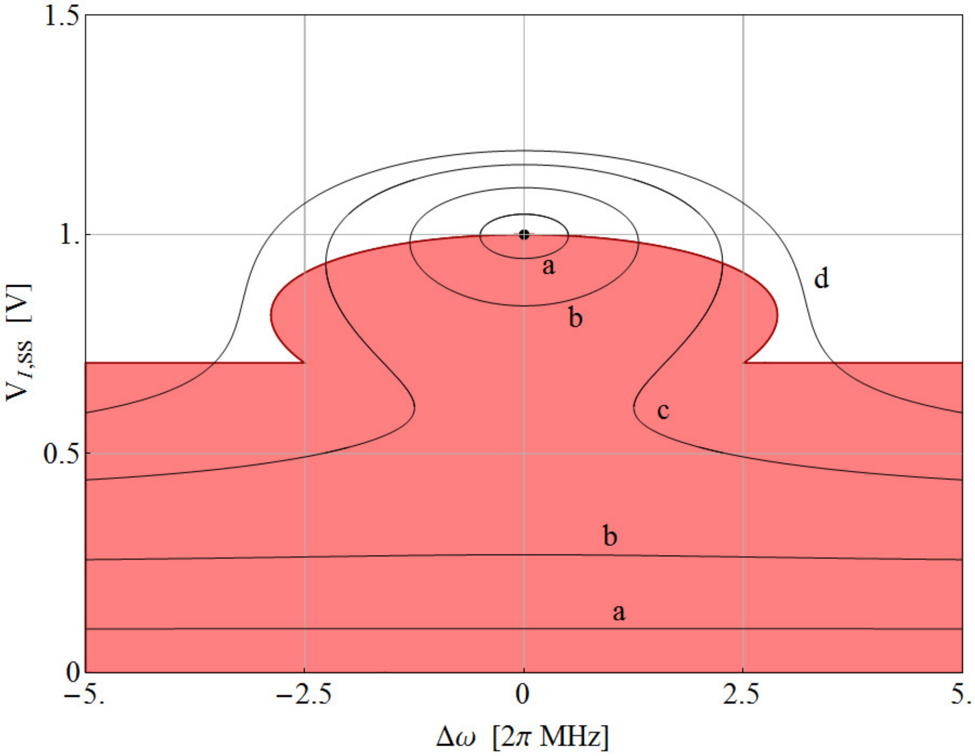

Fig. 3.12 – Steady-state curves superimposed over stability plane for first-order example of Fig 3.3. (a) $V_{G,CW}$ = 100 mV, (b) $V_{G,CW}$ = 250 mV, (c) $V_{G,CW}$ = 400 mV, (d) $V_{G,CW}$ = 500 mV.

Figure 3.12 shows that for lower injection levels, steady-state curves are elliptic-shaped (perfect ellipses for injection tending to zero). However, the lower part (approximately the lower half) of this ellipse is unstable, which means it can only be found in a transient evolution. Given a specific injection, Δω sets with a vertical line all possible transient evolutions, while $V_{G,CW}$ provides which regimes (black curves) are possible. For example, if $\Delta\omega = 1.0 \cdot 2\pi$ MHz (Fig. 3.13) three regimes are possible, but only one (the green dot) falls in the stable region, thus the actual steady-state solution is identified.

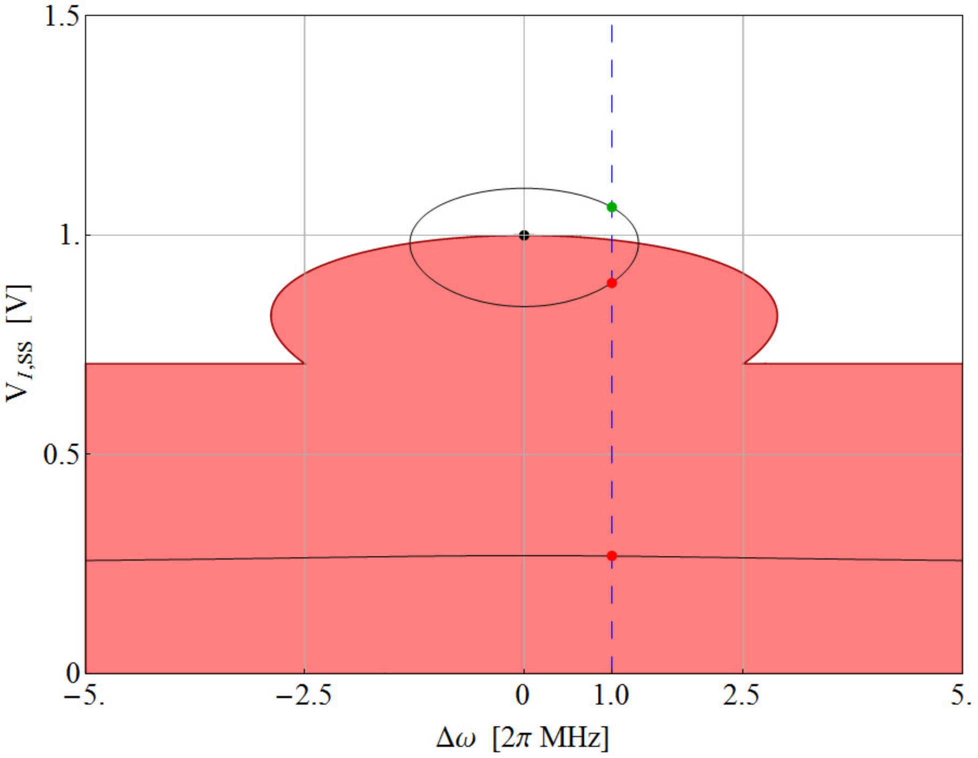

Fig. 3.13 – Steady-state curve for $V_{G,CW}$ = 250 mV, superimposed over stability plane for first-order example of Fig 3.3. Intersections with dashed blue line $\Delta\omega = 1.0 \cdot 2\pi$ MHz are displayed with red dots when unstable or green dots when stable.

For low-level injections a lower branch is in fact present, but it falls (as usual in many cases) entirely inside the unstable region. Therefore, the only stable branch provides by its own the locking bandwidth, which is determined by the interception between it and the Locus border, since the bandwidth is established by the set of "green" points as the frequency detuning varies.

Rising the injection amplitude, higher and lower branches join together (e.g., curve c in Fig. 3.12), and the elliptic-like shape is deformed until, as injection grows, it becomes a curve without backward paths (e.g., curve d).

An relevant observation can be made, useful for injection-locked oscillators design: it is possible to demonstrate that steady-state curves intercept the Locus limit in vertical position, i.e., the derivative tends to infinite. Consequently, if the Boundary border is not involved, and infinite in the derivative is found, the frequency this event occur is the maximum or minimum possible detuning, permitting to analytically evaluate the locking bandwidth.

As previously stated, the Boundary border is relevant at higher injection levels. Indeed, the distinction between low-level injection (LLI) and high-level injection (HLI) can be defined exactly as the transition from a locking band determined only by the Locus, and a bandwidth influenced by the Boundary limit.

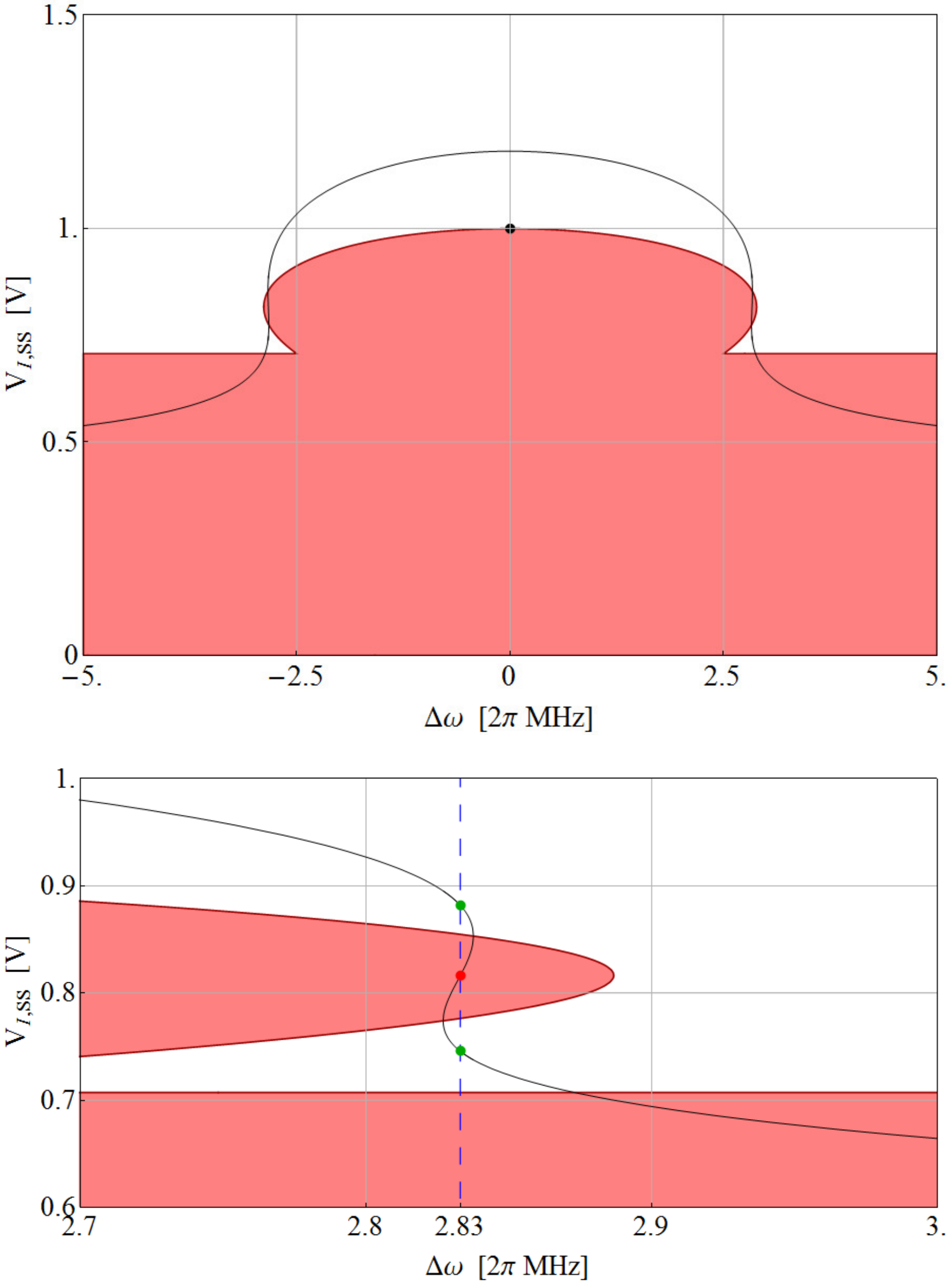

Fig. 3.14 – Steady-state curve for $V_{G,CW}$ = 467 mV, superimposed over stability plane for first-order example of Fig 3.3. Lower figure is a zoom on region where intersections with Locus and Boundary limits lie. Dashed blue line is the section for a sample frequency.

At very high injection levels the Boundary is the only limit involved, but there is a (usually small) range of injections where both borders are relevant. In Fig. 3.14 we can see an example falling in this range ($V_{G,CW}$ = 467 mV). In this case, in an interval of detuning frequencies, two stable locking regimes are possible.

The lower figure displays a zoom on the area where Locus and Boundary borders intersect with steady-state curve, and at $\Delta\omega = 2.83 \cdot 2\pi$ MHz we can observe a condition like this. In addition to higher stable locking regime, a lower one is possible, under the Locus ellipsoid. Which of the two will be obtained depends on the locked/unlocked state previously reached, when sweeping injection's frequency and/or amplitude. Alternative locking bandwidths like these are usually defined "lateral bands", and these are the reason for (small) hysteresis effects often observable [37,57–60]. This time, the maximum detuning - and consequently the locking bandwidth - is determined by the Boundary limit.

Similarly to steady-state amplitude curves, phase curves can be plotted (Fig. 3.15). However, no stability regions can be superimposed, therefore their usage is less relevant to these purposes.

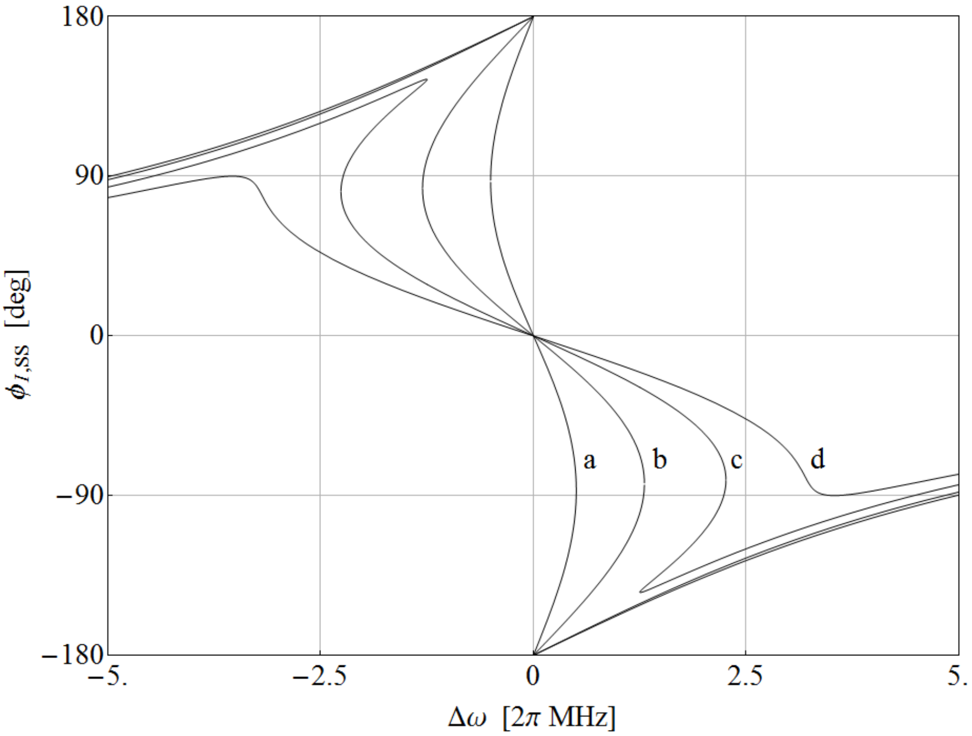

Fig. 3.15 – Steady-state phase curves for first-order example of Fig 3.3. (a) $V_{G,CW}$ = 100 mV, (b) $V_{G,CW}$ = 250 mV, (c) $V_{G,CW}$ = 400 mV, (d) $V_{G,CW}$ = 500 mV.

We can observe that at low-level of injection (e.g., curve a), minimum and maximum locking frequency corresponds to ± 90 degrees, which is strictly related to what many theories (e.g., [26,28]) use as a reference for the locking bandwidth itself. But this is not true for higher injections, like in curve c. That's why a rigorous demonstration of the LBW under a generic injection level should not make use of this approximated equivalence.

Finally, let's plot the locking bandwidth for the example under test. To evaluate it, a numerical method has been performed, coupling two high order systems. The first one connects the Locus limit equation ($p_0 = 0$, from eqn. 3.27) which depends on $\{\Delta\omega, V_{I,SS}\}$, with the steady-state regime equation for amplitude (3.20a), which is a function of $\{\Delta\omega, V_{I,SS}, V_{G,CW}\}$. An implicit function $V_{G,CW} = f\,[\Delta\omega]$ is thus eventually obtained, and exploited for the numerical determination of the borders depending on the Locus limit. The same procedure is followed to obtain the interception with Boundary limits, even if in this simple example its equation ($p_1 = 0$, from eqn. 3.27) is not a function of $\Delta\omega$, and is therefore easier to produce desired results.

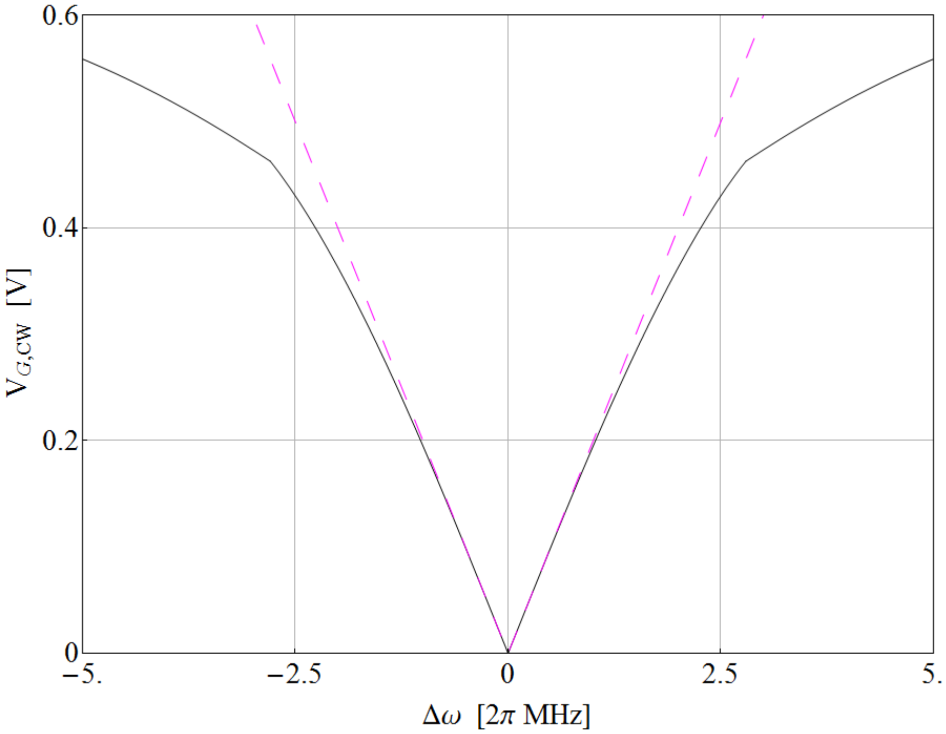

Fig. 3.16 – Locking bandwidth (black solid line) for first-order example of Fig 3.3. In dashed magenta is reproduces the LLI approximation.

In Fig. 3.16 the Locus-related bandwidth limits are the inner ones of the broken black line. That is, when injection is lower only Locus is involved, as previously discussed. In dashed magenta is drawn the low-level injection approximation results, as a comparison, whose analytical equation is the same provided by Adler [26]:

$$LBW_{LLI} = \frac{\omega_F}{Q_F} \cdot \frac{V_{G,CW}}{V_{I,OSC}} \tag{3.29}$$

It is clear from the drawing that (at least in this example) it represents a good approximation until a certain amplitude of the drive signal is reached. We will discuss more about it in the following chapters.

The Boundary-related bandwidth limits are instead the outer parts, as more evident in zoomed Fig. 3.17, where the LBW is the solid broken line. In green it's possible to identify the "Upper Locus"-related limit, i.e., the upper part of the Locus limit (see Fig. 3.14 for example), while the Lower Locus is represented by the red

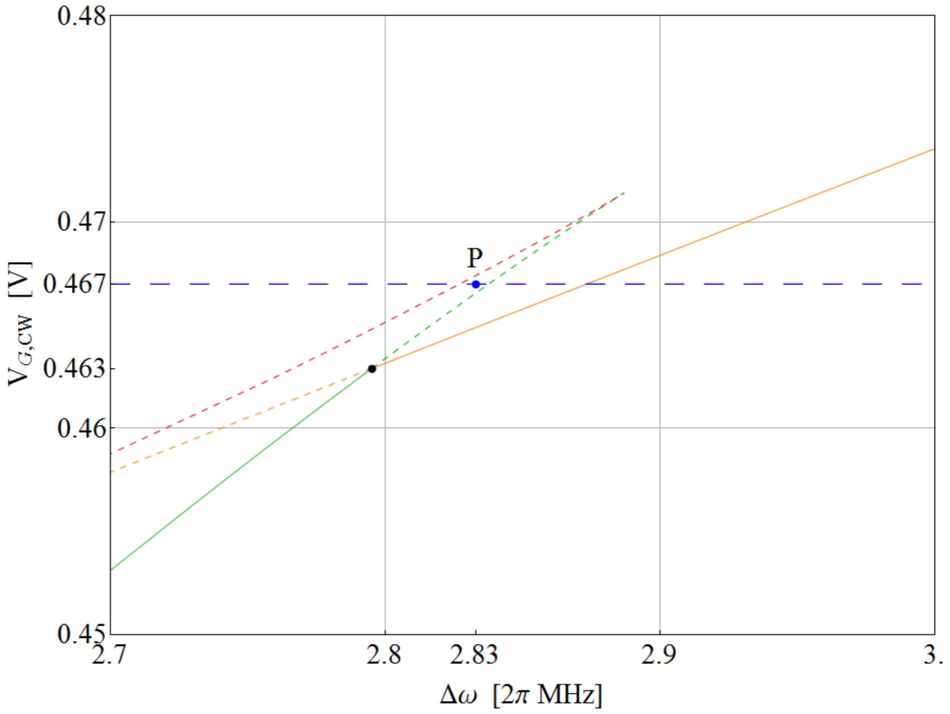

Fig. 3.17 – Zoomed locking bandwidth (solid line) for first-order example of Fig 3.3. Single branches are represented: Lower Locus limit (red), Upper Locus limit (green), Boundary limit (orange). Short-dashed lines highlight the hysteresis phenomenon, while long-dashed blue line and blue point are the section for the sample injection amplitude and frequency chosen in Fig. 3.14.

line. As well, the Boundary limit is the orange line, short-dashed when it is non influential for the determination of the locking bandwidth, even if a lateral band is present. From the black dot to larger detuning frequencies, it is the Boundary to set the LBW limit. Hence, the high-level of injection (HLI) can be considered to begin here (0.463 V). Multiple locking phenomenon seen in Fig. 3.14 is here emphasized, too. In Fig. 3.18 specific regions are depicted, referred to all possible locking modes, not only to the locking bandwidth:

- in green: steady-state regime is locked before reaching the Locus border;

- in yellow: the locking regime is only limited by the Boundary, i.e., the Locus limit is not met across all detuning values;

- in orange: a locking state does exist after crossing both Locus borders, i.e. under the Locus ellipse-like region, but before reaching the Boundary limit.

When both green and orange colors apply, two locking regimes are possible. For example, at a detuning frequency of 2.83 MHz and injection level of 0.467 V (blue point P) both a principal band and a lateral band can be found.

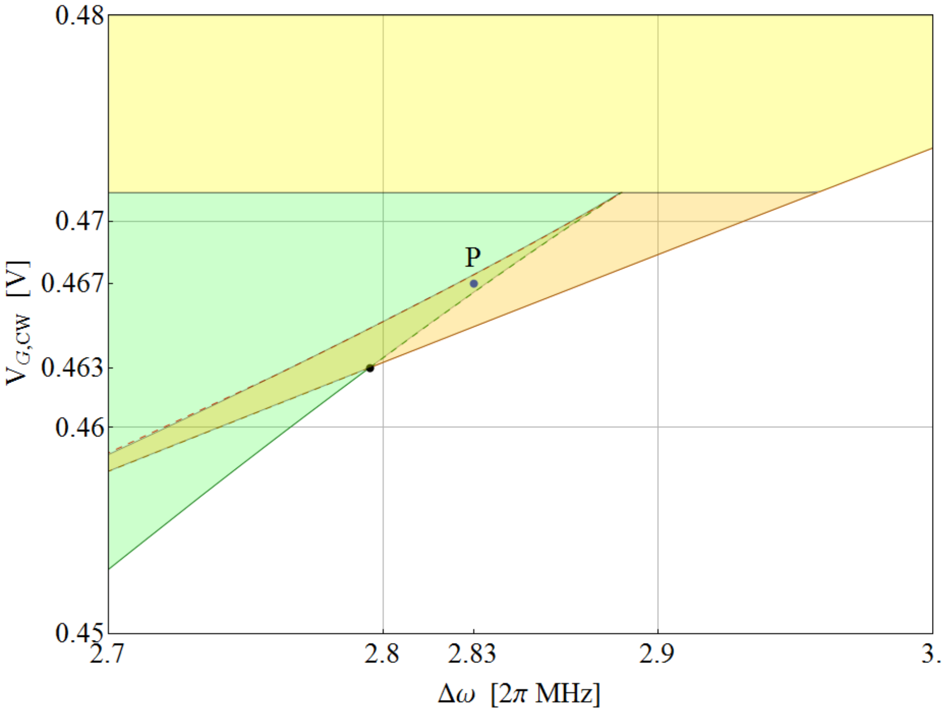

Fig. 3.18 – Zoomed locking bandwidth for first-order example of Fig 3.3 with specific regions highlighted: locking before Locus limit (green zone); locking before Boundary limit (orange or yellow zones). Two locking regimes are possible in intersection zone with both green and orange colors, like the P point example.

4. Bias-Shift Related Phenomena

4.1 About the Shifting-Bias Effects on NDR Oscillators

Among the various aspects not fully accounted for by the theoretical treatments available in the literature , there is the interaction phenomena occurring between DC and RF signal components and associated sub-circuits [61]. In fact, in most of such treatments, the bias of the active device(s) sustaining oscillations is usually assumed as fixed at the quiescent operating point. The analysis is then developed with reference to an analytical/behavioral system model that neglects bias-shift phenomena which - instead - always occur in practice, though in a more or less significant manner [62]. As shown here, even remaining to within the assumption of a weakly-nonlinear operation for the core oscillator, the influence of such bias-shift can be significant on the (driven or not) oscillator performances. More important, it can induce qualitatively new phenomena to occur, which - being unexpected - complicate the understanding of the numerical simulation results and can even mislead the designer [63].

On the basis of the above considerations, a research activity is here reported with the aim of developing an investigation method capable of accounting for such bias-shift phenomena in an efficient and user-friendly manner, so to permit its use more as a design rather than as an analysis tool.

Results here reported are related to a specific - though rather wide - class of *Negative Differential Resistance* (NDR) oscillators operating in a free-running or driven (injection-locked) manner, where this problem is strongly present, as detailed in literature [64,65]. For such circuits, the investigation is developed in the frequency-domain, directly in terms of the time-varying DC and fundamental-frequency components of the circuit variables in a computationally efficient semi-analytical way. This will permit to rapidly highlight differences occurring between non-shifting and shifting-bias cases, as it is well illustrated even by the simple tunnel-diode single-tuned ILO example reported.

4.2 DCE Analysis Method Including DC Harmonic

The circuit structure of the class of negative-resistance (driven) oscillators here considered is illustrated in Fig. 4.1. There are evidenced: the (Thévenin-equivalent) DC power supply net, the nonlinear resistor which models the active device, the L_B/C_B decoupling elements representing the bias-tee network, the linear two-port which incorporates the resonator and load-coupling net, and the (Norton-equivalent) current generator associated to the synchronizing source, when present. Also evidenced are the DC and RF components of the current flowing into the nonlinear element, separated by the bias-tee.

This bias-tee is assumed to be appropriately dimensioned, so to avoid spurious oscillations and to guarantee an adequate decoupling between the biasing circuit and the resonator. Therefore, the interaction between DC and RF occurs only through the nonlinear element common to both meshes. Further considerations on the dimensioning of the bias-tee will be made in the following. As evidenced in the schematic, the bias supply is here considered time-independent (after power-on).

As to the negative-resistance active device, it is modeled here as a memoryless, voltage-controlled, nonlinear element described in time-domain by the polynomial-type constitutive equation:

$$i[t] = \sum_{p=1}^{M} g_{Np} v[t]^{p} \qquad (4.1)$$

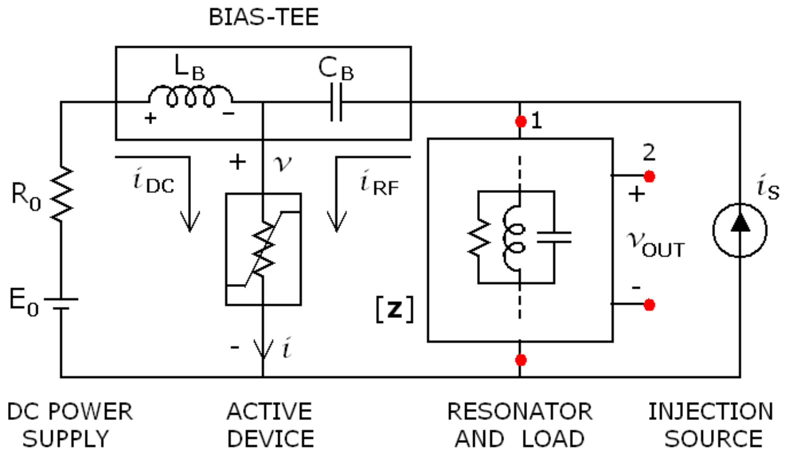

Fig. 4.1 – Circuit structure of the oscillator analyzed (driven if $i_S \neq 0$ or undriven if $i_S = 0$).

The injection signal source, present only when the driven operation is considered, is here restricted to being an unmodulated sinusoidal signal:

$$i_S[t] = I_S \cos[\omega_S t + \psi_S] \tag{4.2}$$

with proper amplitude (I_S) and frequency (ω_S) so to guarantee stable entrainment of the free-running oscillation. Since ψ_S is a constant, it can be assumed as reference phase and set to zero.

The two-port resonator/load is assumed to incorporate linear passive elements only, topologically connected and properly dimensioned so to guarantee, as standard in this type of circuits, a quasi-sinusoidal weakly-nonlinear operation of the oscillator. This two-port will be quantitatively characterized by means of its impedance matrix [**z**].

Considering all above assumptions, for the DC and RF current components can be written:

$$\begin{aligned} i_{DC}[t] &= I_0[t] \\ i_{RF}[t] &= \sum_{p=1}^{M} I_p[t] \cos\left[p \cdot \omega\, t + \psi_p[t]\right] \end{aligned} \tag{4.3}$$

where all $I_p[t]$ and $\psi_p[t]$ are slowly-varying functions in the fundamental-frequency time scale.

As to the node voltages, considering that the resonator has to exhibit a qualitatively parallel behavior (to match the current-defined nonlinear element here assumed) and its implied high selectivity, they will be approximated by the first two harmonics (DC + fundamental) only:

$$v_n[t] \cong V_{n,0}[t] + V_{n,1}[t] \cos\left[\omega\, t + \phi_{n,1}[t]\right] \tag{4.4}$$

with $V_{n,0}[t]$, $V_{n,1}(t)$ and $\phi_{n,1}[t]$ (n=1, … , N) slowly-varying quantities, N being the number of nodes of the circuit.

The rest of the analysis will be then developed with reference to these two signal components only. Of course, a treatment applicable in case of a voltage defined nonlinearity, a series type resonator, and quasi-sinusoidal currents could be developed as well, by duality. In particular, we will perform the analysis in the DCE domain, by extending the perturbation-refined approach introduced in [24] to cope with the presence of a shifting-bias DC component $V_0[t]$ in the voltage $v[t]$ across the nonlinear element, that adds up to the RF one ($\mathbf{V}_1[t] \equiv V_1[t]\, e^{j\phi_1[t]}$). In these definitions the number indication of this main node has been omitted for the sake of compactness. The subsequent steps can then be developed with reference to the frequency-domain (DC+RF) system block diagram of Fig. 4.2, where are evidenced only the network variables (**I** or **V** phasors) which are essential to the treatment.

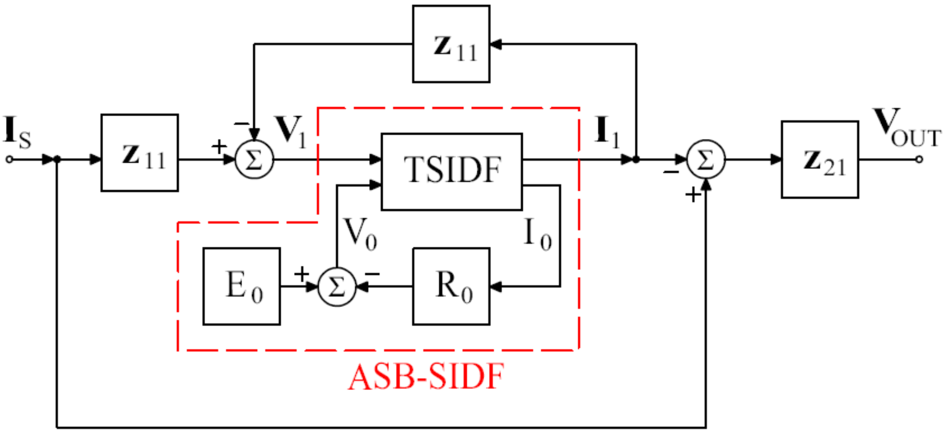

Fig. 4.2 – Frequency-domain block-diagram of the oscillator analyzed (driven if $I_S \neq 0$ or undriven if $I_S = 0$).

In this block diagram, the nonlinear element is modeled via a *Two-Sinusoid Input Describing Function* (TSIDF), which can be associated to the active device of Fig. 4.1 by slightly modifying the original definition set up in [30] to account for one of the two input signal frequencies being set to zero. The use of the TSIDF permits to cope with the presence of the shifting-bias DC component in a rather simple manner. In fact, considering the memoryless nature of the nonlinear element modeled via the TSIDF, the quantities I_0 and I_1 will turn out to be instantaneous functions of V_0 and V_1. We can thus write:

$$\begin{aligned} I_0 &= I_0[V_0, V_1] \\ \mathbf{I}_1 &= I_1[V_0, V_1]\, e^{j\phi_1} \end{aligned} \qquad (4.5)$$

where $\mathbf{I}_1 = I_1[t]\, e^{j\phi_1[t]}$, being $\psi_1[t] = \phi_1[t]$. Notice that, in this specific case, the two functions characterizing the TSIDF outputs will be polynomials of M-th degree. From the block diagram of Fig. 4.2 stems the following DC constraint:

$$V_0 = E_0 - R_0 \cdot I_0[V_0, V_1] \tag{4.6}$$

Since the above implicit equation (4.6) can always be solved (analytically or numerically) for V_0, we can define the function $V_0[V_1]$ relating – under declared assumptions – the instantaneous value of V_0 to that of V_1 in an adynamic manner.

This relationship can then be employed to eliminate V_0 from $I_1[V_0,V_1]$, obtaining a function $I_1[V_1] \equiv I_1[V_0[V_1],V_1]$ which links the RF input to the RF output of the TSIDF. This situation is graphically depicted in Fig. 4.2, where the TSIDF and the biasing elements E_0 and R_0 are incorporated into the macro-block bounded by the red dashed lines. This macro block, representing a generalized SIDF [30], capable of accounting for the "*adynamic shifting-bias*" relationship $I_1[V_1]$, is named here as ASB-SIDF. To this macro-block is associated the nonlinear ASB negative conductance $G_N[V_1] \equiv I_1[V_1] \,/\, V_1$. Notice that even for simple cases, e.g., cubic polynomial nonlinearities, this function can turn out to be quite complicated, for example not monotonic (see formula A3.1 in Appendix A3). If we employ this definition into the equation expressing $\mathbf{V}_1$ as function of $\mathbf{I}_S$ and $\mathbf{I}_1$ and rearrange, we get the steady-state equation (under CW operation):

$$(1 + \mathbf{z}_{11} \cdot G_N[V_1]) \cdot V_1\, e^{j\phi_1} = \mathbf{z}_{11} \cdot I_S \tag{4.7}$$

The general case of a multiple-tuned resonator [66] could be treated as well, following an analogous approach. However in this chapter we will only explore the case of a "single-tuned like" resonator, i.e., a resonator that is well approximated, in the neighborhoods of the oscillation frequency, by a single-tuned equivalent scheme. In parallel-structure case analyzed, this is tantamount to saying that the $\mathbf{z}_{11}$ parameter can be narrow-band approximated by the (3.8) relationship:

$$\mathbf{z}_{11}[j\omega] \cong \frac{R_r\, \omega_r}{\omega_r + j2Q_r(\omega - \omega_r)} \tag{4.8}$$

where Q_r is the loaded quality factor of the resonator. From steady state-equation (4.7) the first-order exact differential model of the adynamic shifting-bias oscillator can now be obtained by applying to (4.8) the BLDO algebra, following the method described in Sec. 3.2. After replacing the term jω with the symbolic operator (jω + d/dt), calculations, rearranging and solving for $V_1{}'$ and $\phi_1{}'$, we finally get:

$$
\begin{aligned}
V_1{}'[t] &= \frac{\omega_r}{2Q_r}\Big(R_r\, I_S \cos[\phi_1[t]] - (1 + R_r\, G_N[V_1[t]]) \cdot V_1[t]\Big) \\
\phi_1{}'[t] &= \omega_r - \omega - \frac{\omega_r}{2Q_F} \cdot \frac{R_r\, I_S \sin[\phi_1[t]]}{V_1[t]}
\end{aligned}
\qquad (4.9)
$$

The set of equations (4.9), different from (3.13) essentially because of the presence of the ASB nonlinearity $G_N[V_1[t]]$, completely describes the dynamics of the phase-locked oscillation under CW injection (or the free-running one, for I_S=0). From it, steady-state and transient operation can be numerically simulated directly in terms of the RF complex envelope components $\{V_1[t],\ \phi_1[t]\}$ with high computational efficiency. The associated evolution of $V_0[t]$ is then straightforwardly calculated from the relationship $V_0[V_1]$.

The dynamical or phase-locking stability can be evaluated in a semi-analytical manner resorting to a local linearization technique (see Sec. 3.5), i.e., by evaluating the Jacobian matrix [J] of system (4.9) and its eigenvalues. We will also calculate the coefficients of the characteristic polynomial associated to [J], obtaining Locus and Boundary stability borders that can be superimposed to the steady-state regime curves of $V_1(\omega_S,\ I_S)$ to get a global picture of the locked oscillator behavior, as previously done for a similar example.

4.3 Examples of Bias-Shift Related Phenomena

To illustrate application of the proposed method, the example oscillator of Fig. 4.3 is analyzed here. The active device, a tunnel-diode, is modeled by a cubic polynomial nonlinearity with fictitious coefficients $\{g_{N1} = 0.07,\ g_{N2} = -0.09,\ g_{N3} = 0.03\}$. The LC tank circuit is characterized by a resonant frequency f_r = 1 GHz

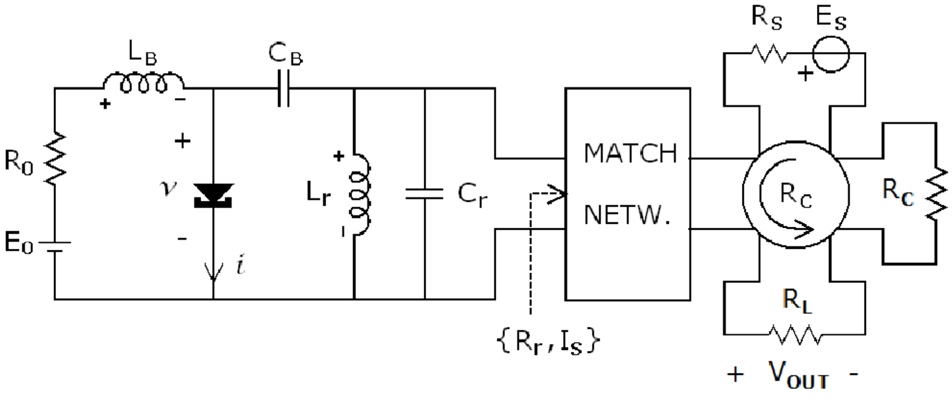

Fig. 4.3 – Example circuit: a tunnel diode reflection-type ILO.

and a loaded $Q_r = 100$ (held fixed by conceptually changing L_r and C_r when the equivalent resistance R_r, determined by the source/load matching network, is parametrically changed to permit investigation of its influence). The values of $C_B = 250$ pF and $L_B = 250$ nH of the bias-tee elements have been balanced to satisfy the stated assumption of minimal interaction between DC and RF sub-circuits, while maintaining a reasonably fast response of V_0 to V_1 variations during dynamical operation. The equivalent injection signal I_S (originated by the generator E_S and injected via the circulator) has variable frequency and amplitude, to within reasonable limits referred to the case at hand. The negative-conductance $G_N[V_1]$ associated to the ASB-SIDF of the biased tunnel diode is depicted in Fig. 4.4 for three different values of R_0 but the same quiescent point ($V_{00} = 1.4$ V).

As shown, the 15 Ω case does not modify too much the quadratic-like shape of the fixed-bias nonlinearity (corresponding to $R_0 = 0\ \Omega$), while avoiding the spurious oscillations associated to this latter case. On the contrary, when R_0 exceeds around 20 Ω, the negative nonlinear conductance is no longer monotonic and non-conventional behavior for the ILO will be observed. Such situation is well evidenced by Figs. 4.5 and 4.6, both of which refer to the case $R_0 = 50\ \Omega$, but different values of R_r. In Figs. 4.5a and 4.6a, the steady-state curves of V_1 are reported, as function of injection frequency, with equivalent current amplitude (I_S) as parameter. Superimposed are the stability regions. In Figs. 4.5b and 4.6b, the phase ϕ_1 is instead reported (only for stable branches, for better readability).

Figures 4.5a-b illustrate that the case $R_r = 200\ \Omega$ does not present unusual phenomena with respect to the case of a simple-cubic nonlinearity, non shifting bias

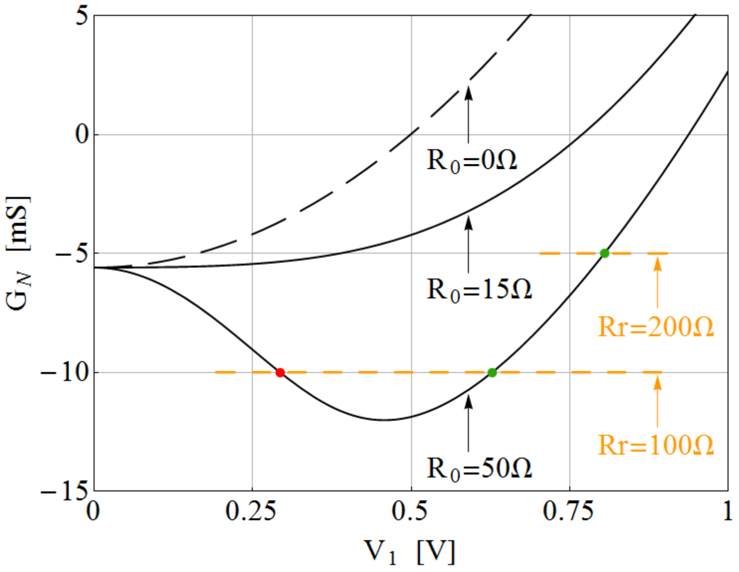

Fig. 4.4 – Dependence of $G_N[V_1]$ on RF signal amplitude V_1 (see (A3.1) in Appendix A3) for V_{00}=1.4V and different values of R_0. Equilibrium points (green when stable, red unstable) of the free-running oscillations are superimposed, pertaining to R_r =100 Ω and 200 Ω.

single-tuned ILO. The free-running oscillation is self-starting (i.e., oscillation at zero voltage is unstable) and has a single regime. The entrained operation evidences a locking band around the free-running oscillation point, which increases monotonically in its frequency span as the injection signal amplitude increases. The Locus and Boundary have their customary look, the first one exhibiting an elliptical-like shape and the second one delimiting, whatever the frequency, an instability region extending to zero from a precise minimum sustainable oscillation-amplitude. Any initial condition will thus evolve into the stable phase-locked regime associated to the specific drive parameters set {ω_S, I_S}. Of course, while qualitative aspects are similar, all quantitative aspects do differ from those that would have been observed if the bias resistance R_0 was smaller (e.g., 15 Ω) or a canonical fixed-bias ILO configuration was involved.

Quite different situation occurs if the matching network is dimensioned so that the equivalent load resistance is decreased to the second test value of R_r = 100 Ω. From Fig. 4.4 we can first note that there are two potential free-running oscillation points (one dynamically unstable and one stable) but they are not self-starting, since the trivial zero solution is stable itself.

As apparent from Figs. 4.6a-b, the injection-locking portrait is actually much

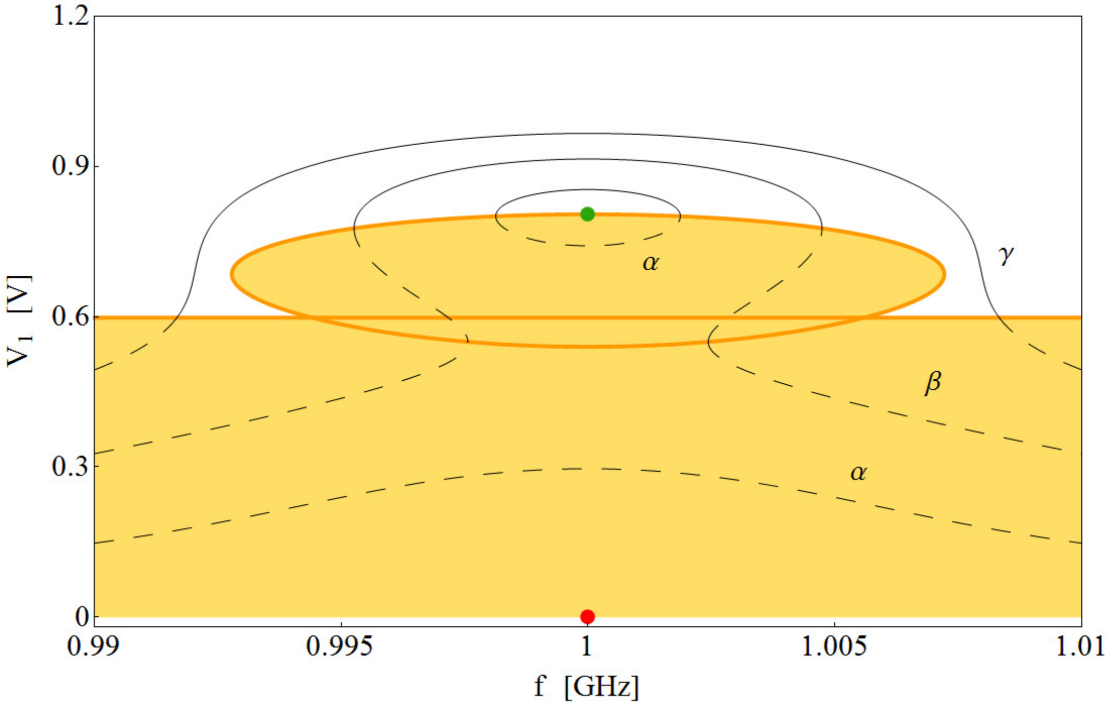

(a)

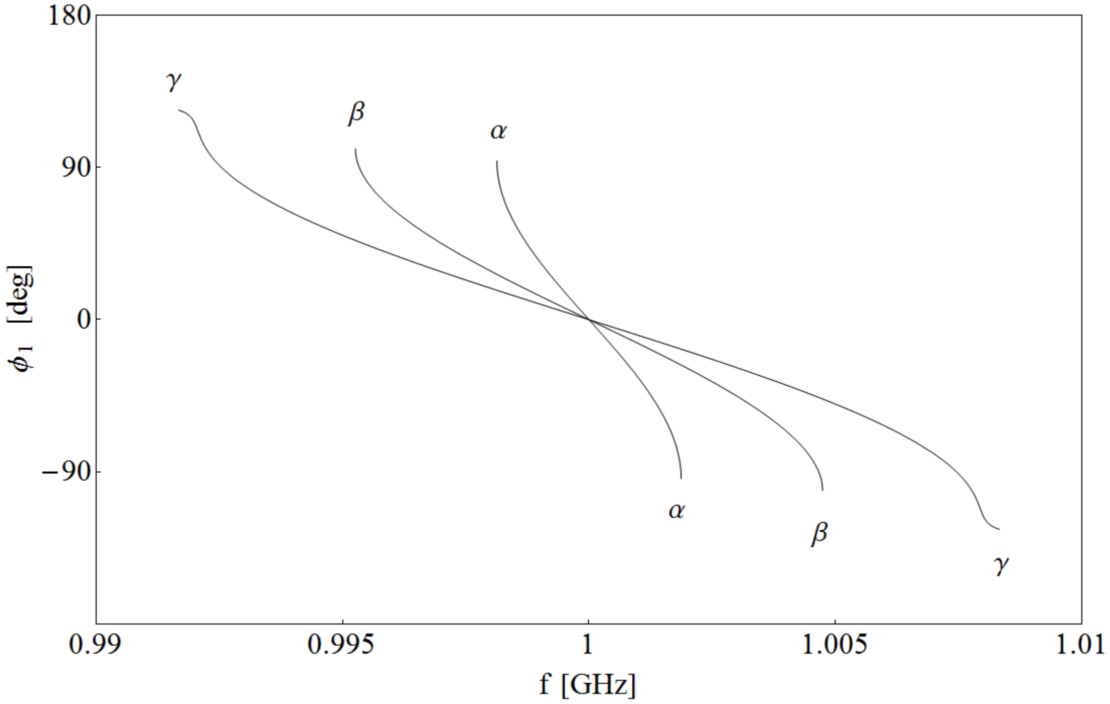

(b)

Fig. 4.5 – Steady-state curves of: ***(a)*** $V_1[\omega_S, I_S]$ *with stability regions superimposed;* ***(b)*** $\phi_1[\omega_S, I_S]$ *for stable branches only. Set#1:* $V_{00} = 1.4$ *V,* $R_0 = 50\ \Omega$*,* $R_r = 200\ \Omega$*.* I_S *= (α) 1.50 mA, (β) 3.75 mA, (γ) 6.00 mA.*

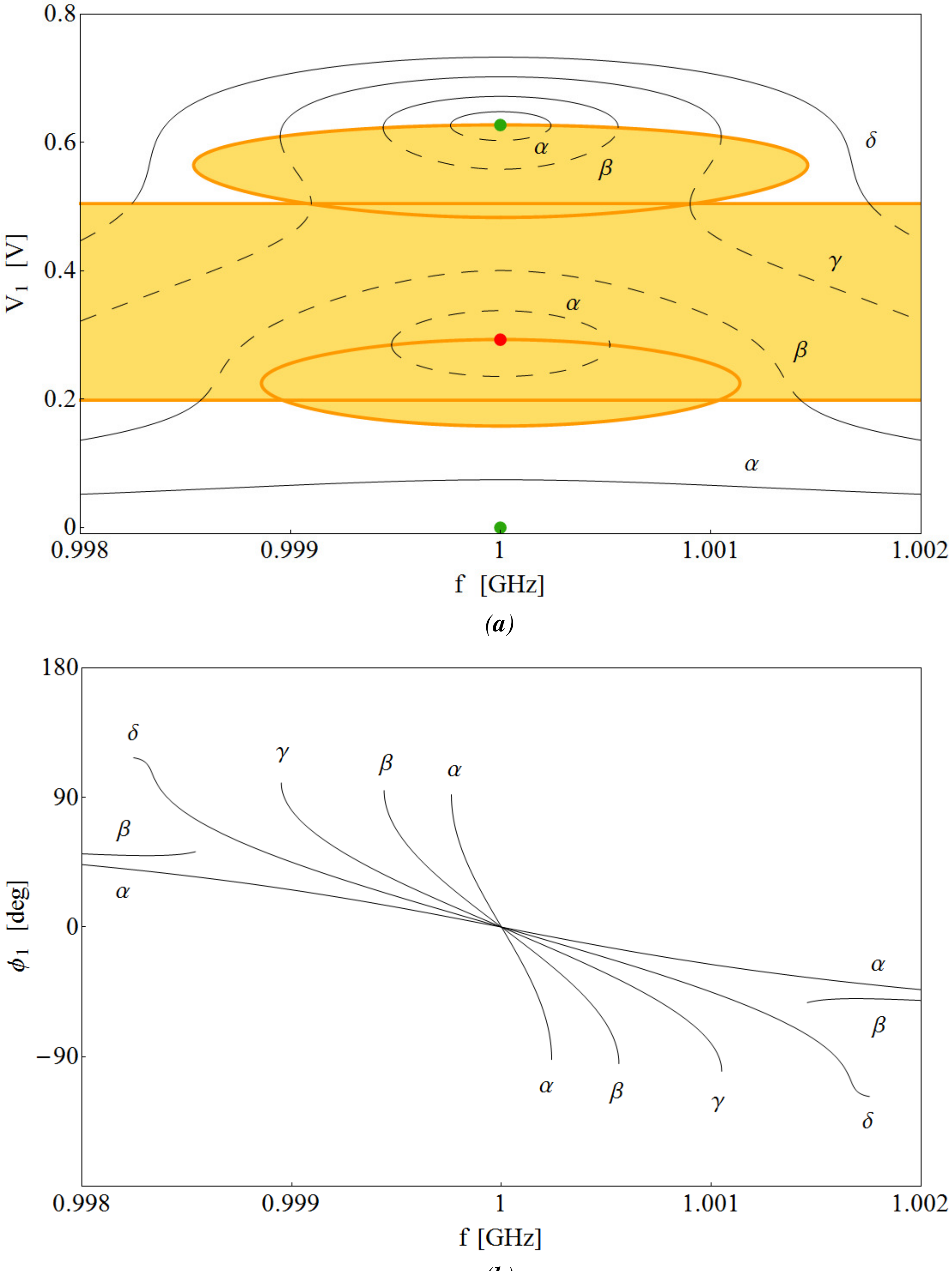

*(**a**)*

*(**b**)*

*Fig. 4.6 – Steady-state curves of: (**a**) $V_1[\omega_S, I_S]$ with stability regions superimposed; (**b**) $\phi_1[\omega_S, I_S]$ for stable branches only. Set#2: V_{00} = 1.4 V, R_0 = 50 Ω, R_r = 100 Ω. I_S = (α) 0.3 mA, (β) 0.7 mA, (γ) 1.3 mA, (δ) 2.0 mA.*

more complicated than expected from a single-tuned cubic-nonlinearity ILO. In fact, the Locus defines now two separated areas associated to the splitting of the curves that describe the steady-state regimes. Also the Boundary now has two straight borders inside the positive voltage region. As a consequence, while a free-running oscillation would not start, a driven one would, even if the injection signal amplitude is small. Being dynamically stable, the attraction basin of this forced oscillation would capture initial conditions starting from low initial voltage values inside it. In addition to these "low output voltage" forced oscillations, a more conventional injection-locked regime would occur at higher voltages (above the upper border of the Locus or Boundary, depending on frequency detuning), but only if the initial conditions are inside its attraction basin.

It is possible to observe the stability plane as a section of a "stability surface", as a function of R_r. With such view, a global analysis becomes much easier, permitting to estimate where and how much stability margin is possible to consider, as a safe region. Extended Locus and Boundary regions, in this stability space, is drawn in Fig. 4.7, where the second Locus area is manifest as the lower cyan region.

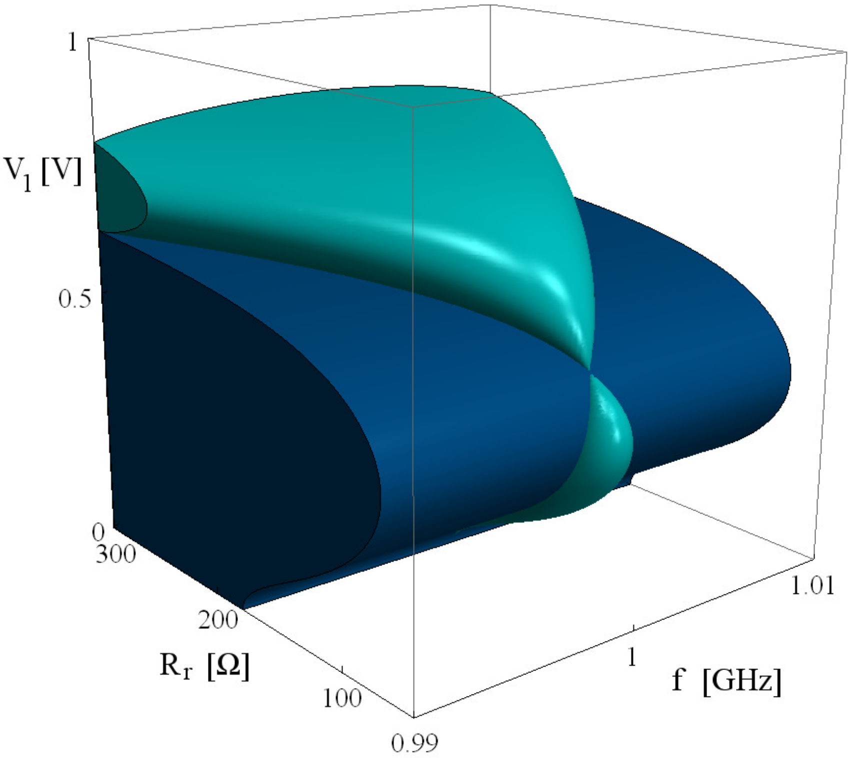

Fig. 4.7 – Stability surfaces, R_r dependent, for R_0 = 50 Ω:
*(**a**) Locus surface (cyan), Boundary surface (dark blue).*

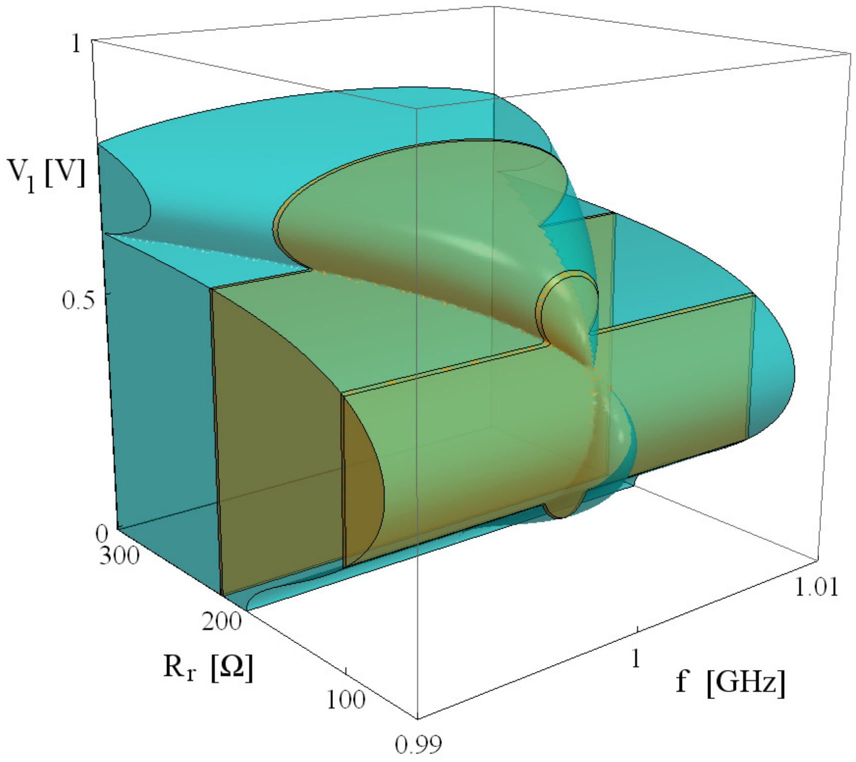

(b)

Fig. 4.8 – Stability surfaces, R_r dependent, for R_0 = 50 Ω:
Locus/Boundary surfaces (transparent cyan), with orange sections at R_r = 200 Ω and 100 Ω.

Last figure (Fig. 4.8) highlights very well the specific cases handled in this section, i.e., R_r = 200 Ω and R_r = 100 Ω. It is noticeable that when the equivalent load resistance decrease below the limit value of about 178 Ω, the trivial zero voltage oscillation becomes stable, causing the free-running oscillation to be unable to self-start.

5. Application on Transmission-Type ILOs

5.1 Injection Locking in TILOs

The celebrated paper published by R. Adler back in 1946 was written with reference to a vacuum tube triode oscillator [26]. In spite of its simplicity and seemingly specific applicability, the formula he derived expresses a quite general feature of injection phase-lock phenomenon when the drive signal strength can be considered a small perturbation of the undriven regime. This behavior has been theoretically and experimentally verified in a very wide range of injection-locking systems (also in the microwave range, for reflection or transmission type [2,31]), not necessarily of circuital nature, as pointed out in Sec. 1.1. This led, over the years, the scientific community to adopt, for the general expression of LBW under low-level injection, the celebrated Adler's formula (2.3).

The problem is now the definition of the various parameters appearing in it: it remains critical the definition of the Q-factor. In the past, but also recently, a number of research work has been devoted to the generalization of the Adler's Q-factor [27,28]. While such studies have greatly improved the applicability of the original theory to different and more complex circuit topologies, the search for a truly general and accurate definition of Adler's equation Q-factor is still not fully accomplished. In particular, TILOs using transistor as active devices need further investigation (like the one here exposed) in order to better fit their behavior.

Initially, the typical design of an ILO was made by modifying an already existing oscillator with the addition of the circuit elements needed for input signal injection and output signal extraction. In the microwave range, this goal was typically achieved by connecting the output of a negative resistance diode oscillator (Gunn, IMPATT, etc.) to the bi-directional interaction port of a non-reciprocal three-port (usually a ferrite circulator), as depicted in Fig. 2.3a. This topological structure of an ILO, referred to as reflection-type (Sec. 2.1), has some advantages: the oscillator can be designed standalone through conventional techniques, or an already built oscillator can be “upgraded” to become an ILO. But the injection efficiency is very low and the achievable LBW is consequently very small, at least for reasonable values of the injection ratio. This can make RILOs unattractive even for the narrow band applications in which it is commonly adopted. More recently, with the pervasive adoption of transistors for most low- and medium-power applications (also in the higher microwave range), the presence of separate input and output ports has permitted to adopt more efficient circuit structures. In this case, the ILO is designed as a whole, incorporating the injection signal mechanism into the oscillation one, in circuit configurations usually referred to as transmission-type, as schematically depicted in Fig. 2.3b, hence the name TILO.

Appropriately exploited, the degrees of freedom so achieved permit to obtain much better performances for TILOs, especially in terms of band widening. On the other hand, the design phase is more complicated, especially when the more flexible feedback type topologies are adopted in place of the more conventional negative-resistance ones, with a structure which can often be cast in the equivalent block diagram illustrated in Fig. 5.1.

In this regard, it has to be noted that, for a truly optimized design of ILOs with innovative topologies, the circuit dimensioning problem can became a hard one. Indeed, the typical nowadays design approach, involving repeated circuit simulations in an iterative loop (often based on numerical optimization algorithms), is not well suited for this case. Because of the stiff nonlinear nature of the problem at hand, the calculation of ILO performances (notably, the LBW) are extremely time

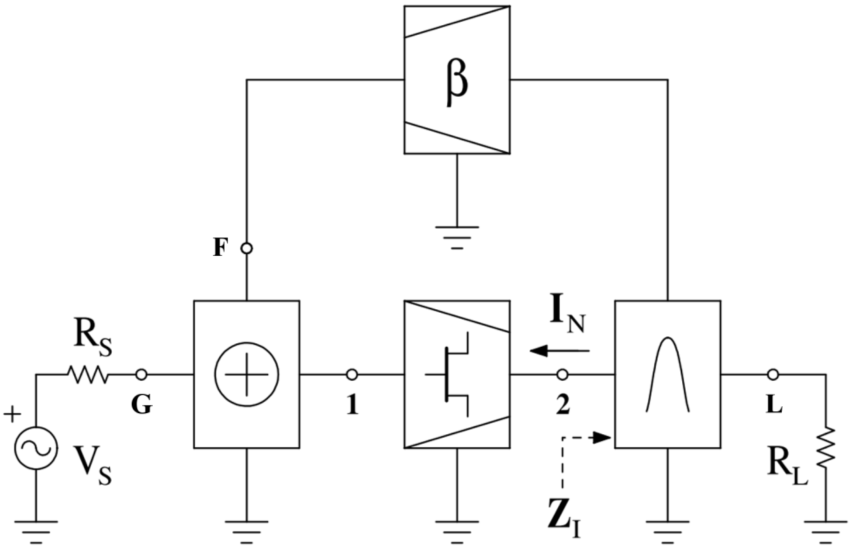

Fig. 5.1 – Equivalent circuit block structure of the class of analyzed injection-locked oscillators.

consuming and not easily automatable, even if most advanced EDA software is adopted. In fact, the intrinsic slowness of the locking phenomenon makes impractical all time domain simulation techniques, and anyhow slow also the use of the faster numerical transient envelope based ones [41] (see Appendix A1).

To solve this design-oriented analysis problem, it is proposed here an approach in the fundamental frequency dynamical phasor domain which, because of its semi-analytical nature, can permit evaluation of all TILO performances in a fraction of time with respect to all other approaches, without limiting the range of applicability to over-simplified circuit topologies or models, as elsewhere proposed.

5.2 Dynamical LLI System Model for Analyzed TILO Structure

The circuit block structure of the transmission type, transistor equipped, oscillating amplifiers under investigation here is illustrated in Fig. 5.1. There is evidenced the single-loop topology comprising the ideal summing network and the feedback block “β”, the amplifying transistor, and the selective tank and load-coupling network. Although not arguable from the figure, it is assumed here that a generic circuit with the shown topology belongs to the class of treatable systems only if it satisfies appropriate conditions. In particular, it's here assumed that the scheme represents a properly designed, self-starting monochromatic oscillator, when no input locking signal is applied ($V_S = 0$). This means that the resonator must possess adequate high selectivity characteristics. Consequently, we can assume that all node voltages will be quasi-sinusoidal quasi-static waveforms under transient operation. They can thus be characterized in terms of the relevant first-harmonic components (amplitude and phase: $\mathbf{V}_X = V_X[t]\ e^{j\phi_X[t]}$; with X = {1, 2, G, F, L}), which result slowly varying functions of time. Therefore, we can develop the analysis in the previously described dynamical fundamental-frequency complex-envelope domain. In particular, after deep investigation of the problem, the equivalent system block structure depicted in Fig. 5.2 have been selected [67]. It can be derived from its circuital counterpart of Fig. 5.1 after proper identification of the various functional blocks. For the purpose of this analysis, it is important to evidence the presence of the $\mathbf{Y}_N$ block which represents the active device. Unlike Section 3.2 in which the nonlinearity is modeled using a SIDF, or other treatments

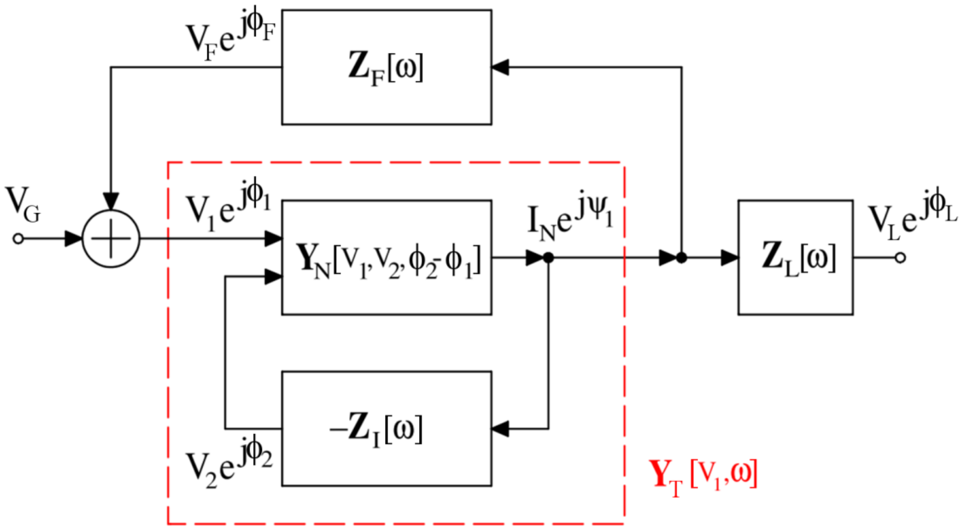

Fig. 5.2 – Equivalent system block structure in the fundamental-frequency complex-envelope domain.

employing equivalent single I/O element [24,25,27,28], here a TSIDF (Two-Sinusoid Input Describing Function) will be adopted, similar to the one employed in Sec. 4.2, but notably different in terms of circuital interpretation. In fact, while a SIDF model is serviceable to describe in the frequency-domain the instantaneous nonlinear relationship between voltage and current of a one-port active element (such as a negative resistance diode), this is not the case when two-port active elements (such as transistors) are involved. Such variation of the system block scheme is the key point that will permit, in the end, to achieve the desired accuracy in the simulation of the TILO response. In fact, the use of the TSIDF allows to account for the nonlinear dependence of the current $\mathbf{I}_N$ not only on the input phasor $\mathbf{V}_1$, but also on the output phasor $\mathbf{V}_2$. In formulas, we have:

$$\mathbf{I}_N[\mathbf{V}_1, \mathbf{V}_2] = \mathbf{Y}_N[V_1, V_2, \phi_2-\phi_1] \cdot \mathbf{V}_1 \qquad (5.1)$$

which recalls that the dependence of $\mathbf{Y}_N$ on node voltage phases is a differential and not an absolute one and, more important, that the TSIDF associated to a memoryless nonlinearity is a complex quantity.

Now, since the voltage phasor $\mathbf{V}_2$ is related to the transistor output current via the input impedance $\mathbf{Z}_I$ of the resonator:

(5.2) $$\mathbf{V}_2 = -\mathbf{Z}_I[\omega] \cdot \mathbf{I}_N[\mathbf{V}_1, \mathbf{V}_2]$$

we can combine (5.1) and (5.2) into an implicit set of equations which defines an overall, equivalent, TSIDF admittance $\mathbf{Y}_T[V_1, \omega]$ of the active block (the dashed box in Fig. 5.2), implicitly defined through the relationship:

(5.3) $$\mathbf{I}_N[V_1, \omega] = \mathbf{Y}_T[V_1, \omega] \cdot \mathbf{V}_1$$

Such nonlinear and frequency dependent mutual admittance $\mathbf{Y}_T$ is capable of accounting, in an unabridged way, for all the nonlinear interaction phenomena occurring between the active device and its passive, resonant, load. In particular, it can model the practically observed dependence of the open loop gain (OLG) on the drive voltage amplitude V_1 not only in terms of its mid-band magnitude but also of its selectivity characteristics (see subsequent Section 5.4, for a numerical example of such effect, with Fig. 5.6):

(5.4) $$\mathbf{A}[V_1, \omega] \equiv \mathbf{OLG}[V_1, \omega] = \frac{\mathbf{V}_F}{\mathbf{V}_1} = \mathbf{Z}_F[\omega] \cdot \mathbf{Y}_T[V_1, \omega]$$

By combining (5.4) with the summing element constitutive equation

(5.5) $$\mathbf{V}_1 = \mathbf{V}_G + \mathbf{V}_F$$

after setting $\phi_G = 0$ as a reference, and rearranging, we get:

(5.6) $$(1 - \mathbf{A}[V_1, \omega]) \cdot \mathbf{V}_1 = V_G$$

At this point, we can particularize the subsequent steps of this analysis to the specific case of low-level injection here considered. If the injection signal V_G is “small”, we can take advantage of perturbation analysis methods and develop further calculations using incremental quantities (with respect to the free-running oscillating regime). In particular, for the nonlinear drive voltage amplitude V_1 we set:

(5.7) $$V_1[t] = V_{1,OSC} + \Delta V_1[t]$$

In last and following equations, the subscript “OSC” indicates evaluation in correspondence of the free-running oscillating condition, as calculable from (5.6) setting $V_G = 0$, and then solving the resulting nonlinear equation $\mathbf{A}[V_{1,OSC}, \omega_{OSC}] = 1$, either analytically or numerically. When (5.7) is applicable, it is also convenient to linearize the open loop gain definition:

$$\mathbf{A}[V_1, \omega]\Big|_{V_1=V_{1,OSC}+\Delta V_1} \cong \mathbf{A}[V_{1,OSC}, \omega] + \Delta V_1 \cdot \frac{d\mathbf{A}[V_1, \omega]}{dV_1}\Big|_{V_1=V_{1,OSC}} \tag{5.8}$$

If we make the additional assumption that the transistor nonlinearity, while causing a marked dependence on V_1 of the OLG’s mid-band magnitude and selectivity, does not appreciably changes its resonant frequency, we can adopt for it the following abridged relationship:

$$\mathbf{A}[V_1, \omega] \cong \frac{\omega_{OSC}\,(1+\Delta V_1 \cdot A_{d,OSC})}{\omega_{OSC}+2j(Q_{OSC}+\Delta V_1 \cdot Q_{d,OSC})(\omega - \omega_{OSC})} \tag{5.9}$$

where

$$A_{d,OSC} \equiv \frac{dA}{dV_1}\Big|_{V_1=V_{1,OSC}\ ,\ \omega=\omega_{OSC}} \quad ; \qquad Q_{d,OSC} \equiv \frac{dQ}{dV_1}\Big|_{V_1=V_{1,OSC}} \tag{5.10}$$

As easily recognizable, this approximation corresponds to a single-tuned like, reduced-order model for $\mathbf{Z}_F$, as introduced in (3.8), but with a variable Q-factor. This single-tuned approximation has been found to be adequate in most practical cases. Replacing (5.9) into (5.6) provides the incremental algebraic model which describes, in the frequency-domain, the oscillating amplifier regime under continuous-wave (non-modulated) low-level injection operation.

On this basis, we can now make use of the perturbation-refined approach based on BLDO algebra [24] to derive the incremental differential model which describes, in the complex-envelope domain, the oscillating amplifier dynamics under general low-level injection operation.

As a first step, we quantitatively specify the smallness of the injection signal, setting for it the order defining condition:

$$V_G = \mathcal{O}\left[\frac{V_{1,OSC} \cdot A_{d,OSC}}{Q_{OSC}}\right] \tag{5.11}$$

Under above assumptions, and taking for grant also that $A_{d,OSC}$ and $Q_{d,OSC}/Q_{OSC}$ will be both $\mathcal{O}[1]$, as commonly occurs, the consequential order defining relationships can be shown to hold:

$$\frac{\Delta V_1}{V_{1,OSC}} = \mathcal{O}\left[\frac{1}{Q_{OSC}}\right] \quad ; \qquad \frac{\omega - \omega_{OSC}}{\omega_{OSC}} = \mathcal{O}\left[\frac{1}{Q_{OSC}{}^2}\right] \tag{5.12}$$

Making use of (5.11) and (5.12) to truncate, to the same order of magnitude, all terms appearing into the unabridged CW regime equation (5.6), provides its first-approximation-exact abridged counterpart:

$$\left(2jQ_{OSC}\frac{\omega - \omega_{OSC}}{\omega_{OSC}} - \Delta V_1 \cdot A_{d,OSC}\right) \cdot V_{1,OSC}\, e^{j\phi_1} = V_G \tag{5.13}$$

which analytically defines steady-state values of ΔV_1 and ϕ_1 under CW injection ($\Delta V_{1,SS}$ and $\phi_{1,SS}$), as a function of the injection signal amplitude (V_G) and frequency (ω), and of the abridged system parameter set $\{\omega_{OSC}, Q_{OSC}, A_{d,OSC}\}$.

To obtain the differential system model we can follow an analogous perturbation-refined procedure, starting from the dynamical analogue of (5.9) that is obtained simply by replacing the term $j\omega$ with its symbolic counterpart ($j\omega$ + d/dt) and then performing the necessary calculations and higher order terms truncations. This way, we firstly obtain:

$$\begin{aligned} &\frac{\Delta V_1'[t]}{V_{1,OSC}} + j\left(\omega - \omega_{OSC} + \left(1 + \frac{\Delta V_1[t]}{V_{1,OSC}}\right)\phi_1'[t]\right) + \\ &\qquad - \frac{\omega_{OSC}}{2Q_{OSC}} \cdot A_{d,OSC} \cdot \Delta V_1[t] = \frac{\omega_{OSC}}{2Q_{OSC}} \cdot \frac{V_G}{V_{1,OSC}} e^{-j\phi_1[t]} \end{aligned} \tag{5.14}$$

where $\Delta V_1'[t]$ and $\phi_1'[t]$ correspond to derivatives with respect to time. Note that $A_{d,OSC}$ and $Q_{d,OSC}$ represent instead quantities differentiated with respect to V_1 variable (cf. equation 5.10). After manipulation and truncation, the normal form differential set of equations is obtained:

$$(5.15)\qquad \begin{aligned} \Delta V_1'[t] &= \frac{\omega_{OSC}}{2Q_{OSC}}\left(V_G \cos\left[\phi_1[t]\right] + A_{d,OSC}\, V_{1,OSC}\, \Delta V_1[t]\right) \\ \phi_1'[t] &= -(\omega - \omega_{OSC}) - \frac{\omega_{OSC}}{2Q_{OSC}} \cdot \frac{V_G}{V_{1,OSC}} \sin\left[\phi_1[t]\right] \end{aligned}$$

Equations (5.15) do provide solution to the stated analysis problem. In fact, they not only permit to simulate with great computational efficiency the dynamical response of the driven transmission-type ILO directly in terms of amplitude and phase transients (in a scaled time-domain), but also provide the mean to perform the phase-lock stability investigation, i.e., to evaluate the LBW, in a fully analytical manner.

5.3 Stability Analysis and Locking Bandwidth

Steady-state equation (5.13) provides, in general, more than one solution, i.e., more than one possible regime. Whether a given equilibrium point is stable or not has to be ascertained via a dynamical stability analysis. Having at one's disposal the differential system equations directly in terms of the complex-envelope components, as here provided by (5.15), such analysis can be straightforwardly carried out via a local linearization technique, as performed in Sec. 3.5. The LLI linearization here performed provide a simpler expression, despite the more complex treatable circuit structure. More precisely, we firstly evaluate the 2x2 Jacobian matrix in the equilibrium point considered:

$$(5.16)\qquad \underline{\underline{J}} = \begin{bmatrix} \frac{\omega_{OSC}}{2Q_{OSC}} A_{d,OSC}\, V_{1,OSC} & (\omega - \omega_{OSC})\, V_{1,OSC} \\ 0 & \frac{\omega_{OSC}}{2Q_{OSC}} A_{d,OSC}\, \Delta V_{1,SS} \end{bmatrix}$$

The coefficients of the associated characteristic polynomial are then obtained:

$$p_0 = \left(\frac{\omega_{OSC}}{2Q_{OSC}} A_{d,OSC}\right)^2 V_{1,OSC} \cdot \Delta V_{1,SS} \tag{5.17}$$
$$p_1 = -\frac{\omega_{OSC}}{2Q_{OSC}} A_{d,OSC} \left(V_{1,OSC} + \Delta V_{1,SS}\right)$$

The locking stability criteria are eventually obtained by setting the condition that both the zero (p_0) and first degree (p_1) coefficients must be positive, corresponding to the Locus and Boundary conditions, respectively. Since the coefficient $A_{d,OSC}$ is required to be negative (for the free-running oscillation stability), and the locked oscillation amplitude ($V_{1,OSC} + \Delta V_{1,SS}$) positive, the unique condition remains: $\Delta V_{1,SS} > 0$. The minimum/maximum (angular) frequency for which phase-lock can occur at the given value of injection signal is thus provided by the limit condition: $\Delta V_{1,SS} = 0$. In view of equation (5.13), this is tantamount to saying that:

$$\left|2jQ_{OSC} \frac{\omega - \omega_{OSC}}{\omega_{OSC}}\right| = \frac{V_G}{V_{1,OSC}} \tag{5.18}$$

from which we get:

$$LBW_{LLI} = \omega_{MAX} - \omega_{MIN} = \frac{\omega_{OSC}}{Q_{OSC}} \cdot \frac{V_G}{V_{1,OSC}} \tag{5.19}$$

Notice that the low-level injection bandwidth expressed by (5.19) is seemingly the same to the well known expression derived by Adler (cf. eq. 2.3a), and their most recent extension [27,28], with one significant difference: the fact the OLG quality factor is evaluated at the oscillation amplitude $V_{1,OSC}$ rather than at $V_1 = 0$ (i.e., coincident with the loaded quality-factor of the linearized transfer function). This fact explains the better numerical agreement achieved by this theory with respect to previous methods. It can also be remarked that presented treatment has derived stability borders (5.19) without requiring the fictitious assumption of a hard-limiting of the oscillation amplitude in order to eliminate (5.15a) from calculations, as done in [26] and most of the other subsequent related works.

5.4 Example #1: a Meissner TILO

To better illustrate the features of the devised approach, a lumped-elements Meissner oscillating amplifier is analyzed here as an example of application. The circuit structure is illustrated in Fig. 5.3, while the elements values are indicated in Tab. 5.1. For the sake of simplicity a purely resistive Shichman-Hodges nonlinear model has been adopted for the JFET. The resonant frequency and the loaded Q of the tank circuit were set to 160MHz and to 100, respectively. The turn ratio of the coils was set to 10 and the OLG margin for oscillation buildup set to +1.6 dB.

To get started, the nonlinear transfer function $\mathbf{A}[V_1, \omega]$ has to be evaluated. Notwithstanding the simplicity of model at hand, its analytical derivation is not

$V_{TO} = -2$ V	$\beta = 0.6$ mA·V^{-2}	$\lambda = 0$	$I_S = 10$ fA
$L_1 = 100$ nH	$L_2 = 1$ nH	$K = 1$	$C_0 = 10$ pF
$C_L = 100$ nF	$R_L = 10$ kΩ	$V_{DD} = 3$ V	$V_{GG} = -1$ V

Tab. 5.1 – Parameters of example circuit of Fig. 5.3.

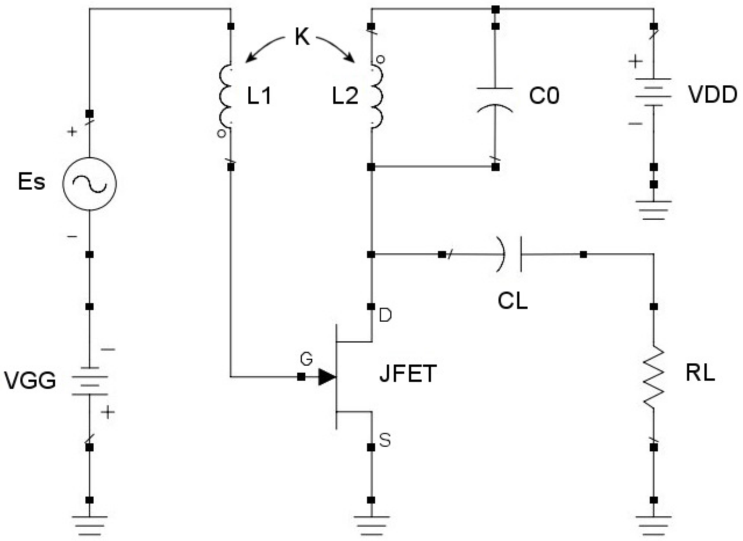

Fig. 5.3 – Meissner type oscillating amplifier.

practicable. Therefore a numerical approach has been adopted, resorting to a frequency-domain, Harmonic-Balance based, RF circuit simulator (above cited ADS, by Agilent EEsof [22]) to analyze the open-loop counterpart of the circuit of Fig. 5.3, by sweeping both frequency and amplitude of the sinusoidal "input" drive signal V_1 ($\equiv V_{gs}$), and recording the "output" voltage V_F ($\equiv V_{L1}$). The corresponding graphs of the magnitude at ω_{OSC} and Q-factor of the open loop gain $\mathbf{A}[V_1, \omega]$ are reported in Fig. 5.4a and Fig. 5.4b, respectively. As evident from the figure, these graphics show a very similar trend, though not identical as it may seem. There are evidenced the free-running oscillation point (brown dot) and the associated derivatives (red dashed line). The relevant numerical values turn out to be: $V_{1,OSC} \cong 0.235$ V (which corresponds to an output oscillation amplitude of $V_{L,OSC} \cong 2.35$ V); $Q_{OSC} \cong 84.4$; $A_{d,OSC} \cong -2.77$; $Q_{d,OSC} / Q_{OSC} \cong -2.50$.

With such numerical values, solution of (5.13) as function of injection signal amplitude V_G provides the family of steady-state response curves illustrated in Fig. 5.5, where the shaded region indicates the Locus unstable locking region. The stable regime is thus unique for a given pair $\{V_G, \omega\}$, and corresponds to the point on the top most branch. Black dots indicate the related LBW limits, as calculated with a full numerical solution of the circuit of Fig. 5.3, obtained by means of a circuital simulation. Aside from observing that they are practically coincident with the

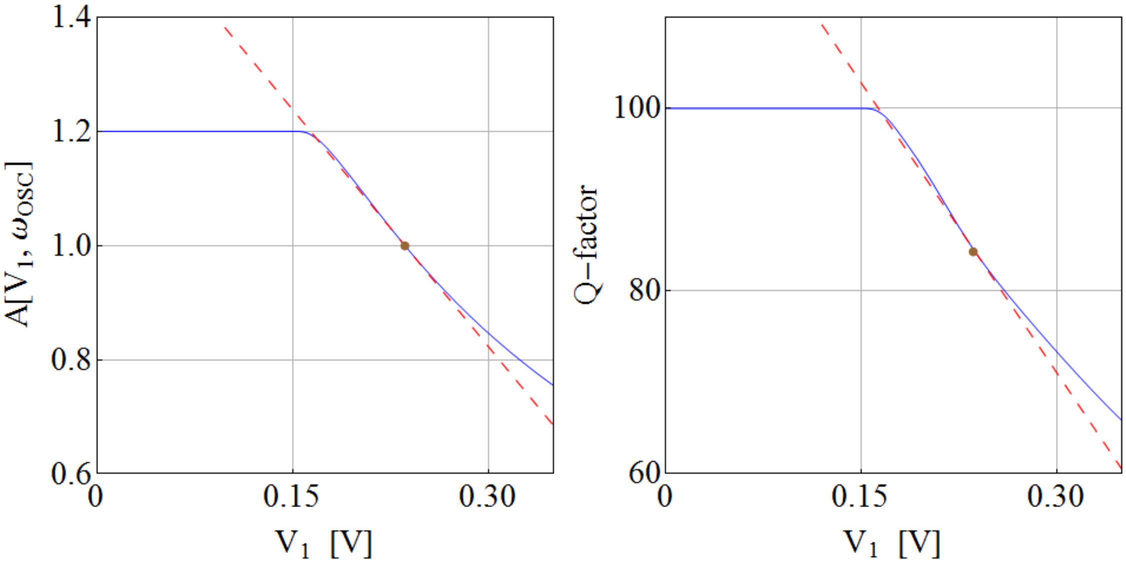

(a) ***(b)***

Fig. 5.4 – Dependence of (a) $|\mathbf{A}[V_1, \omega_{OSC}]|$*, (b) Q-factor, on the transistor drive voltage* V_1*.*

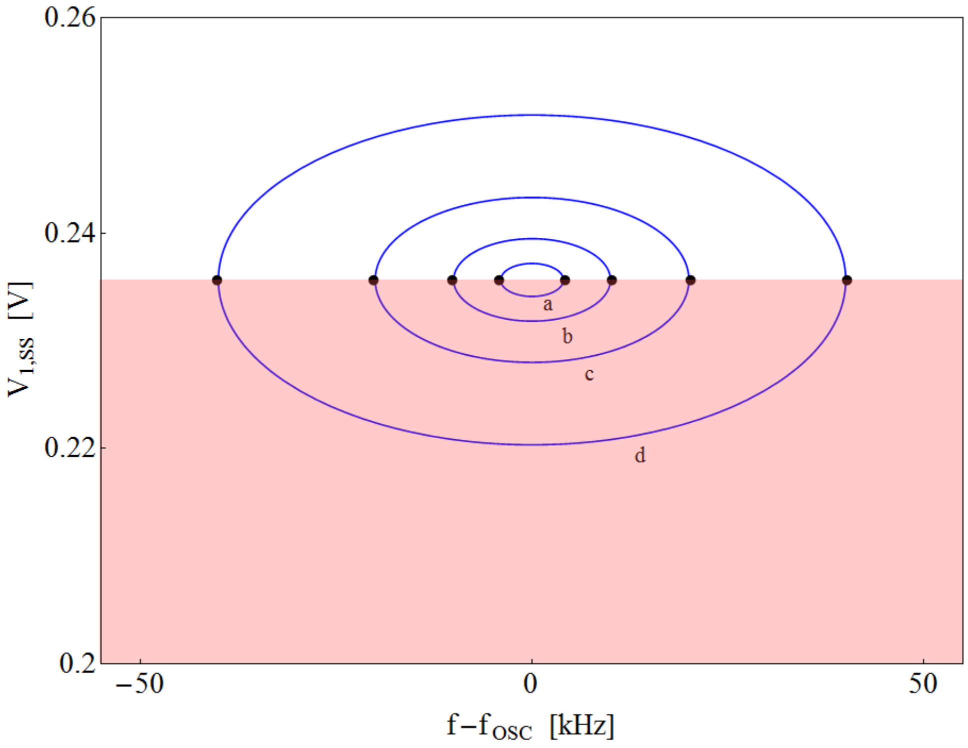

Fig. 5.5 – Analytically evaluated steady-state regime curves $V_{1,SS}[\omega]$ *for injected* V_G *amplitudes of: (a) 1 mV, (b) 2.5 mV, (c) 5 mV, (d) 10 mV. The pink shaded area indicates unlocked regimes. Black dots are locking extremes calculated through ADS simulation.*

analytical solution provided by (5.19), i.e., the vertical tangent points of elliptical curves defined by (5.13), it must be remarked that such evaluation has been extremely time-consuming. In fact, to numerically determine LBW borders, Circuit Envelope option of ADS (ADS/CE) had to be adopted, in a man-assisted iterative search procedure, based on bracketing stable and unstable operating conditions, discriminated via long-term run phase-locking transients. The simulation time spent, of course, was orders of magnitude greater than the one necessary to apply formulas derived by proposed method. An example in Appendix A1 shows the comparison between the two required time durations.

Before going on, it must be stressed (see Fig. 5.4b) the non-negligible difference between the “linear” value of the Q-factor (= 100) with respect to the “nonlinear” one evaluated at the oscillation regime ($Q_{OSC} \cong 84$). Using the former instead of the second would have caused an error in the evaluated locking bandwidth of more than 15%.

The nonlinear behavior of the OLG function is well displayed by the three-dimensional Fig. 5.6, where amplitude and phase of $\mathbf{A}[V_1, \omega]$ are illustrated.

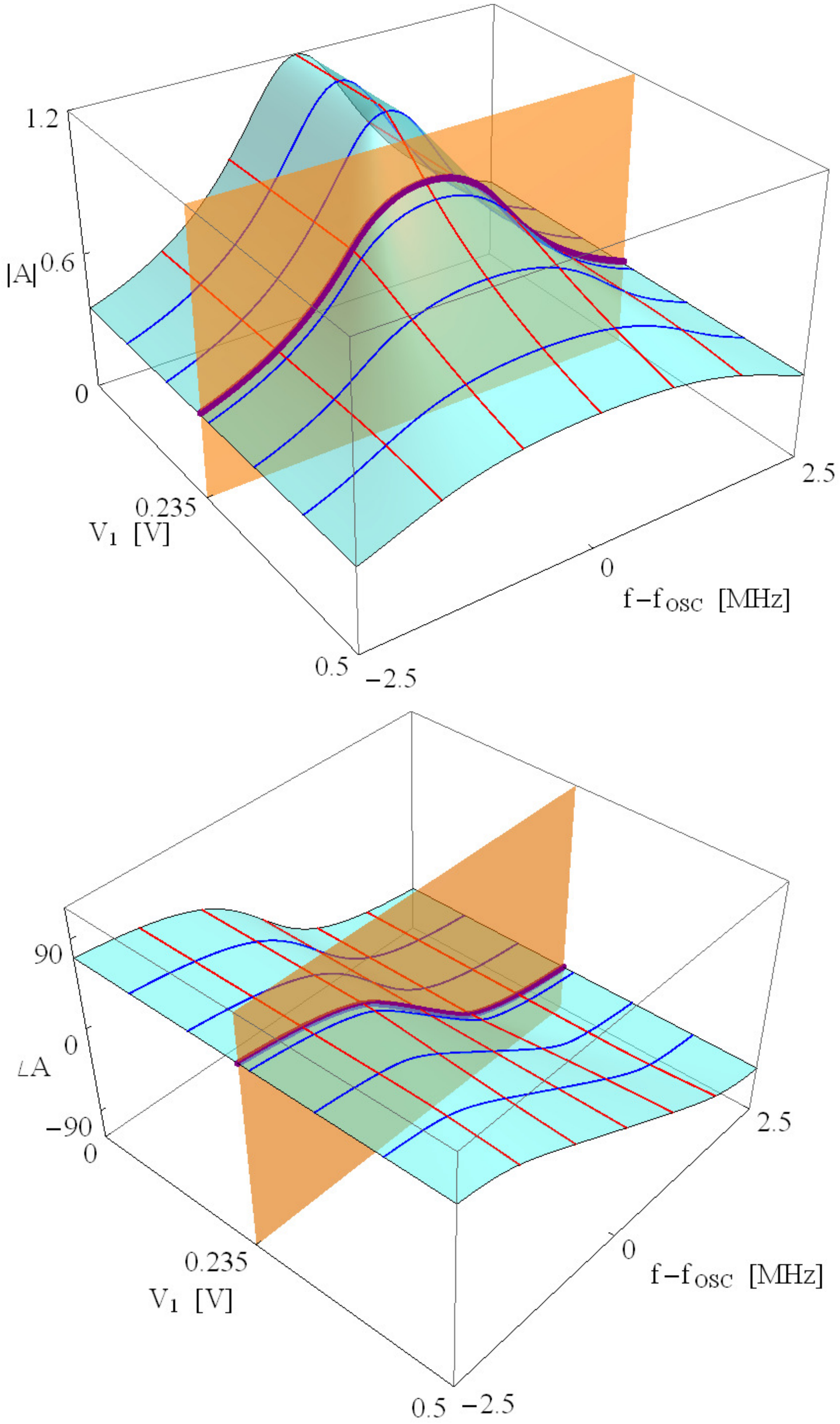

Fig. 5.6 – Three-dimensional dependence of amplitude (upper graphic) and phase (lower graphic) of ***A****[V_1, 2πf] on its variables, for circuit in Fig.5.3. Orange sections are at $V_{1,OSC}$.*

The upper 3D graphic shows that the section of the open-loop gain, at a given voltage, is shaped as a single-tuned resonator with little or no variation until nonlinearities comes in place and (at the oscillation voltage) the middle-band gain reaches unity. As well, the phase figure exhibits a nonlinear trade, moving its middle-band derivative, as a detailed observation can grant.

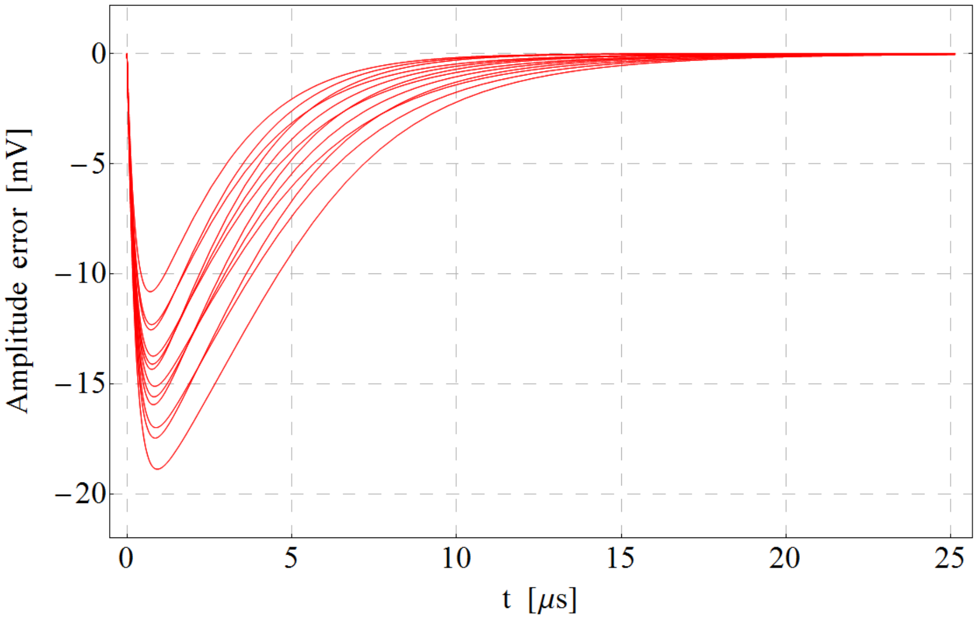

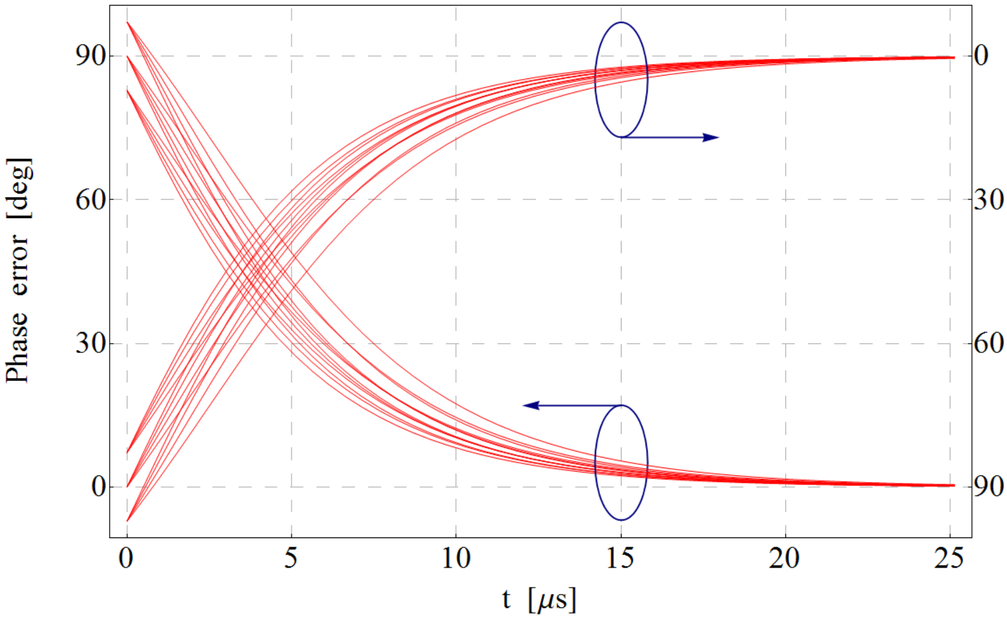

Fig. 5.7 – Influence of a residual FM on the transient response of the example circuit to an OQPSK signal: evolution of amplitude ($\Delta V_1[t] - \Delta V_{1,SS}$, upper graphic) and phase ($\phi_1[t] - \phi_{1,SS}$, lower graphic) errors.

As example of use of the dynamical equations (5.15), the effect of a residual FM of 12 kHz (peak) on the transient response of the example oscillating amplifier to an OQPSK input signal is illustrated. The evolution of the amplitude and phase error corresponding to a ± 90º phase transition is shown in Fig. 5.7. While analogous curves could have been obtained via ADS/CE the convenience and the insightfulness of a semi-analytical approach, as the one provided by (5.15), has to be anyhow remarked, especially in view of design optimization purposes.

5.5 Example #2: a Colpitts TILO

A different example (Fig. 5.8) is represented by a classical Colpitts scheme with a gate driving source and a third capacitor (C_0) accounting for both the inductor and

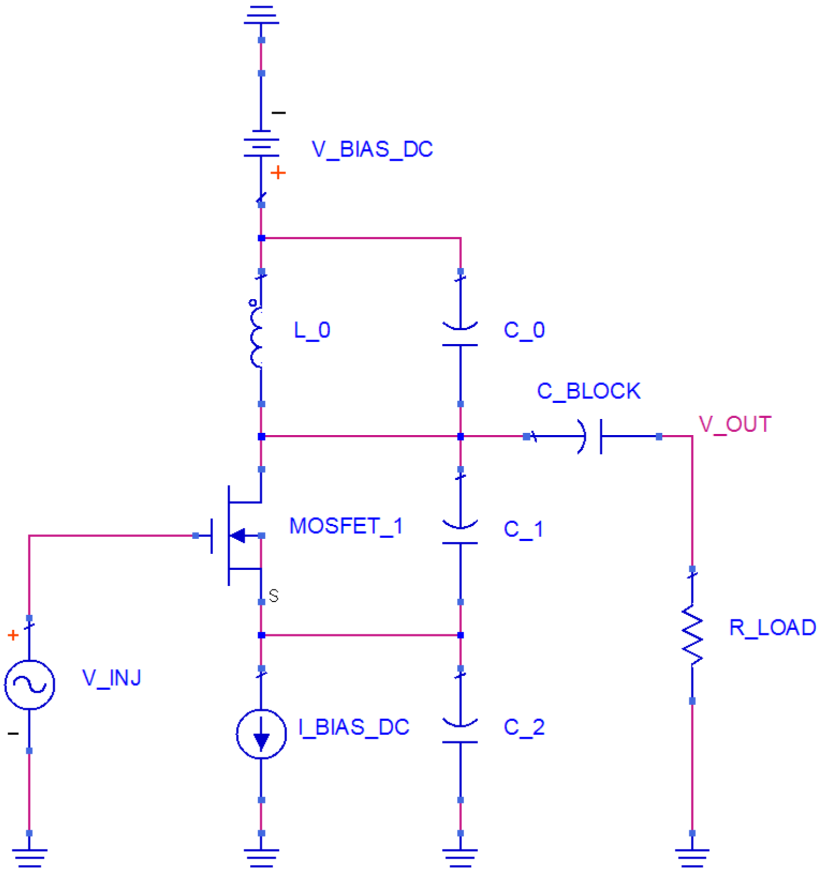

Fig. 5.8 – Example circuit: a MOSFET Colpitts injection-locked oscillator.

V_{TO} = 2 V	KP = 1 mA·V^{-2}	λ = 0	W/L = 1
C_0 = 1.2 pF	C_1 = 150 pF	C_2 = 150 pF	C_{BLOCK} = 10 nF
L_0 = 133 nH	R_{LOAD} = 12 kΩ	$V_{BIAS,DC}$ = 5 V	$I_{BIAS,DC}$ = 1 mA

Tab. 5.2 – Parameters of example circuit of Fig. 5.8.

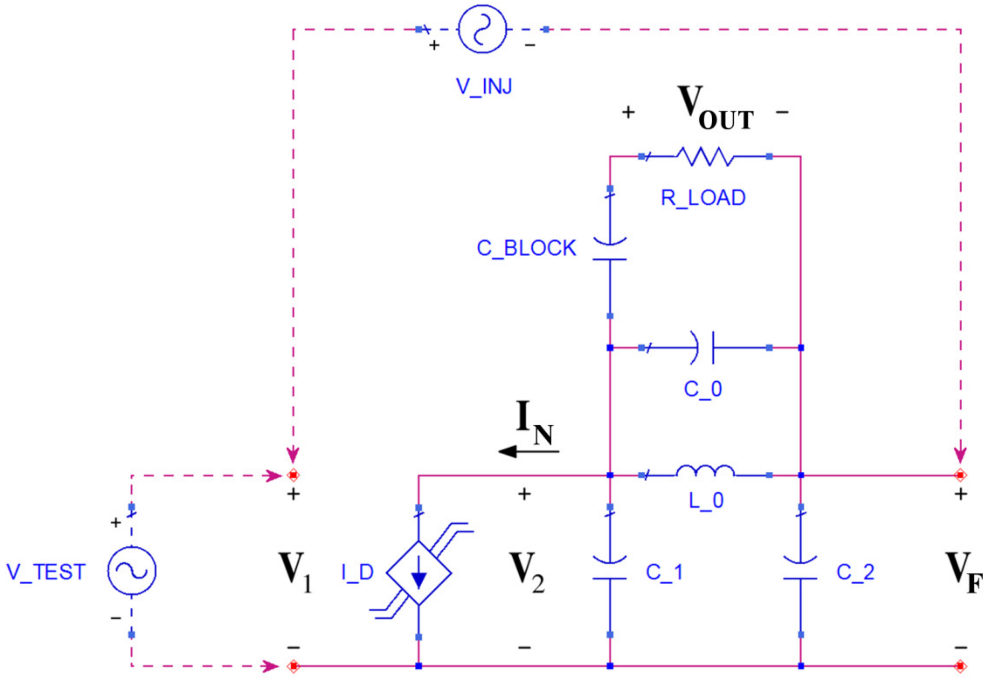

Fig. 5.9 – Fundamental-frequency equivalent scheme of the example ILO circuit.

the load parasitic [34]. The MOSFET active device is characterized via a simple SPICE/Lev.1 quadratic model with no parasitic elements, biased at 1 mA with a fixed DC current source. With the parameters values adopted (see Tab. 5.2), the free running oscillation amplitude and frequency result approximately 5V (peak), and 50 MHz, respectively. Notice the selection of a zero value for λ, purposely made in order to better evidence that the differences that will be observed between Q and Q_{OSC} are not attributable to the small-signal output conductance of the transistor (includable in both), and cannot thus be accounted for by any pseudo-linear analysis of the circuit, as in [27,28].

For such a topology, the system quantities can be identified as follows: $\mathbf{V}_G = \mathbf{V}_{INJ}$, $\mathbf{V}_1 = \mathbf{V}_{gs}$, $\mathbf{V}_2 = \mathbf{V}_{ds}$, $\mathbf{I}_N = \mathbf{I}_d$, $\mathbf{V}_L = \mathbf{V}_{OUT}$. The corresponding open-loop fundamental frequency dynamical equivalent circuit is illustrated in Fig. 5.9, where the double non-linearity mark on the VCCS representing the TSIDF current $\mathbf{I}_N[V_{gs}, V_{ds}, \phi_{dg}]$ graphically recalls the dependence of the transistor drain current i_D on both v_{GS} and v_{DS} (v_{BS} is fixed at 0 V).

Notwithstanding the simplicity of the transistor model adopted, analytical determination of the associated $\mathbf{Y}_T[V_{gs}, \omega]$ is not viable. Therefore, for the determination of Q_{OSC}, the numerical alternative of using a HB simulator was adopted. To this purpose, firstly, the oscillation frequency (f_{OSC}) and amplitude

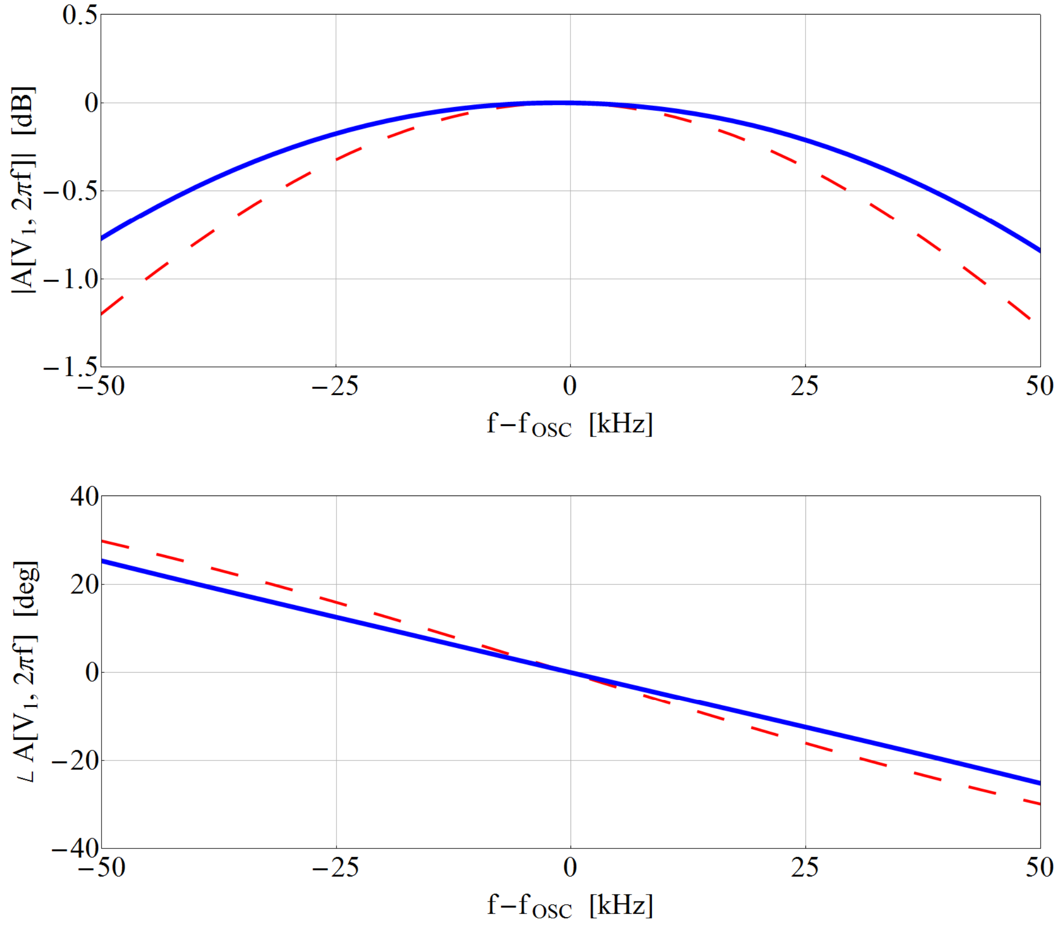

Fig. 5.10 – Magnitude (upper graphic) and phase (lower graphic) of the simulated open-loop nonlinear transfer function $\mathbf{A}[V_1, f - f_{OSC}]$*, normalized to 1, for the limit value of* $V_1 \cong 0$ *(dashed red line) and for* $V_1 = V_{1,OSC} \cong 5V$ *(solid blue line).*

($V_{gs,OSC}$) have been obtained from the closed-loop circuit with no driving signal (see Fig. 5.9), using the HB-based nonlinear oscillator analysis tool of ADS simulator. Then, the open-loop circuit associated to the one in Fig. 5.8 (see Fig. 5.9) was simulated with the standard HB analysis tool of ADS, obtaining the frequency response of the open-loop transfer function corresponding to the oscillation amplitude above determined. The result of this procedure is graphically depicted in Fig. 5.10, where magnitude and phase of $\mathbf{A}[V_{1,OSC}, \omega]$ are shown (solid blue curves) in comparison with the analogous quantities that would be obtained neglecting the nonlinear load effect associated to the dependence of i_D on v_{DS} (dashed red curves), corresponding to the plot of $\mathbf{A}[0, \omega]$, as obtained from a small-signal (AC) simulation. Both curves are scaled to 1 (i.e., 0 dB) at free-run oscillation frequency.

From above simulation data, the group delay can be easily numerically determined and the value of Q_{OSC} calculated with the relationship $\tau_{g,OSC} \cdot \omega_{OSC}/2$ (cf. equations 2.3). In this example $Q_{OSC} \cong 221$, while the conventional loaded $Q \cong 287$, i.e., around 30% lower. To confirm that this result is the correct value to adopt for Q-factor in LBW_{LLI} equation (5.19), an iterative man-assisted search for the determination of the locking-bandwidth bounds has been then carried out in this example too, resorting to multiple phase-locking transient-envelope simulations by means of the ADS/CE.

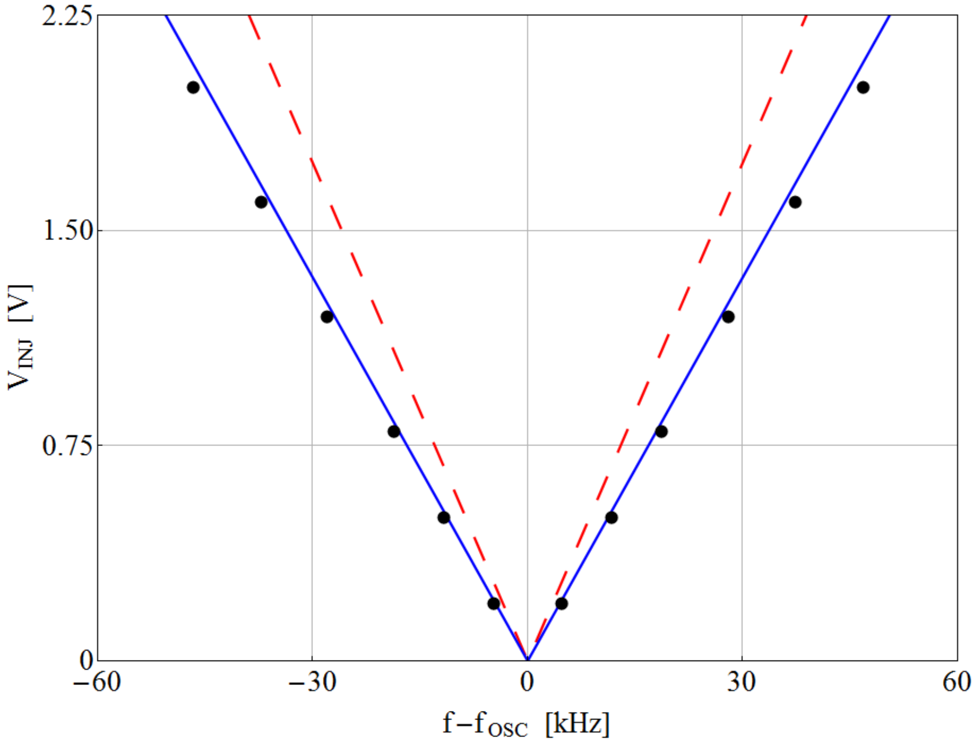

Fig. 5.11 – Comparison of locking-bandwidth calculations: previous theory (dashed red), this theory (solid blue), ADS/CE simulations (black dots).

The comparison of the LBW calculated with the standard and the proposed procedure (dashed red, and blue solid line, respectively) is illustrated in Fig. 5.11, where the additional black dots indicate the transient-envelope simulation data. As can be seen, the locking stability limits stemming from the proposed approach fit very well with the full-simulation (ADS/CE) derived ones, while the use of the Q-factor as previously defined in the literature would cause a non-negligible error in the LBW evaluation.

The proposed approach, not only exhibits equivalent accuracy at a fraction of time, but is also easily automatable. Therefore, it can be advantageously embedded into a numerical tuning or optimization loop and can thus become a useful tool for a meaningful optimization of the performances of injection-locked oscillators in performance-driven design-oriented applications.

5.6 Example #3: Designing an X-Band Microwave TILO

The initial motivation for the development of the presented theory was to have at one's disposal a design-oriented analysis method to be adopted for the correct dimensioning of a microwave TILO with a novel circuit structure which made no use of nonreciprocal input elements. A prototype of this configuration operating at 10.75 GHz was designed and built, and the results presented in [31]. This feedback-type TILO [35] is adopted here also to illustrate the application of the proposed method and to highlight some design and simulation aspects. The structure of the circuit realized is illustrated in Fig. 5.12. There are evidenced: the (50 Ω matched) 3 dB hybrid Branch-Line Coupler (BLC) committed to the coupling of the in/out power, the delay line feeding the transistor amplifier, and the Dielectric Resonator transmission-type filter closing the loop. The microwave amplifier was made using a single PHEMT device (ATF-36077), out-of-band stabilized and input matched to 50 Ω (under large signal operation). The output matching network was designed to provide reasonable gain under small signal operation and full power under large signal operation into 50 Ω. The *dielectric resonator* (DR) filter was dimensioned

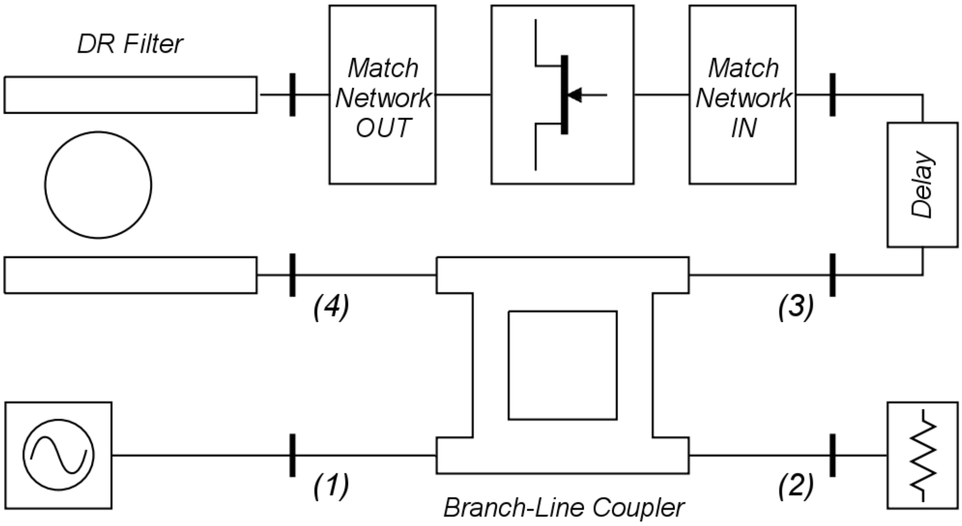

Fig. 5.12 – Circuit diagram of the X-band example TILO.

using advanced electromagnetic simulation tools after having determined its specs on the basis of the results of the application of the proposed method.

During the design phase of this TILO, the theory presented in Sections 5.2-5.3 was adopted cyclically for the initial dimensioning and subsequent refining of the DR filter and delay line structures to satisfy project specifications. This procedure was greatly simplified by the semi-analytic nature of the method which permits to enucleate critical design parameters and use them for their approximate direct dimensioning. For the purpose of this example the details of this nested design loops will be skipped over, while focusing mainly on application of the analysis method. To this end, we can refer to the TILO simplified behavioral macro-model shown in

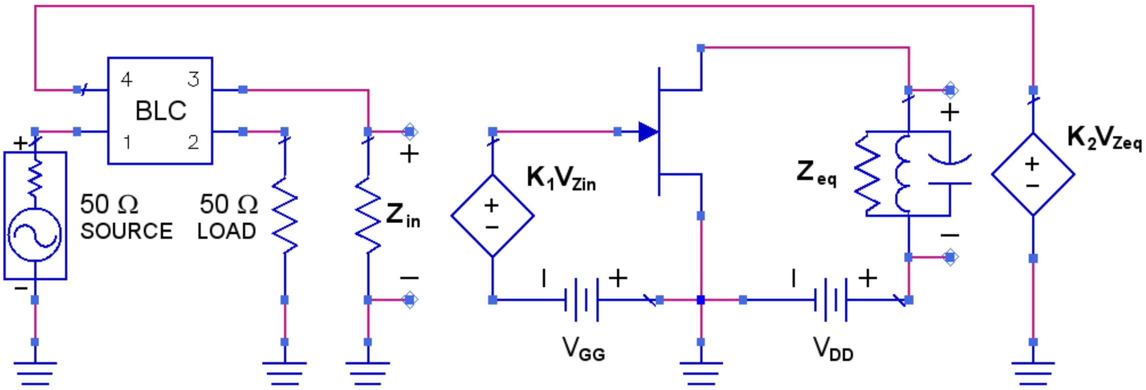

Fig. 5.13 – Macro-model of the example TILO analyzed.

Fig. 5.13. The equivalent RLC parallel resonator models the resonant impedance Z_{eq} associated to the DR filter, as seen by the "intrinsic" transistor, described as a memoryless nonlinear 2D-VCCS element. All the remaining parasitic elements and losses/delays are absorbed (as amplitude and phase of the coefficients $\mathbf{K}_1$ and $\mathbf{K}_2$) into the two VCVS elements which model the stages preceding and following the transistor. Though not evident from the figure, in present case Z_{in}, i.e., the amplifier large-signal input impedance, was dimensioned to 50 Ω, for modularity purposes. To achieve the desired locking bandwidth (~4.5 MHz) for the nominal value (–20 dBm) of the injection signal, in view of (5.19), one has to obtain the correct value of the product $Q_{OSC} \cdot V_{1,OSC}$ acting on the free design parameter set. In this design, features selected are the insertion losses and the loaded Q-factor of the DR filter block, which, together with the constraint set on its in/out 50 Ω match, determine the position and the distance of the DR puck with respect to the two coupled microstrip lines. In our model this induces a parametric dependence of $\mathbf{K}_2$ and $Q_{00} \equiv Q(V_1)|_{V1\approx 0}$ on filter geometry. As previously remarked, knowing Q_{00} does not suffice to compute Q_{OSC}, and thus to evaluate LBW_{LLI}. Therefore, even if a global, parametric, analytical or numerical model of all components (e.g., the DR filter) is available, a few design iterations are still required to achieve the targeted

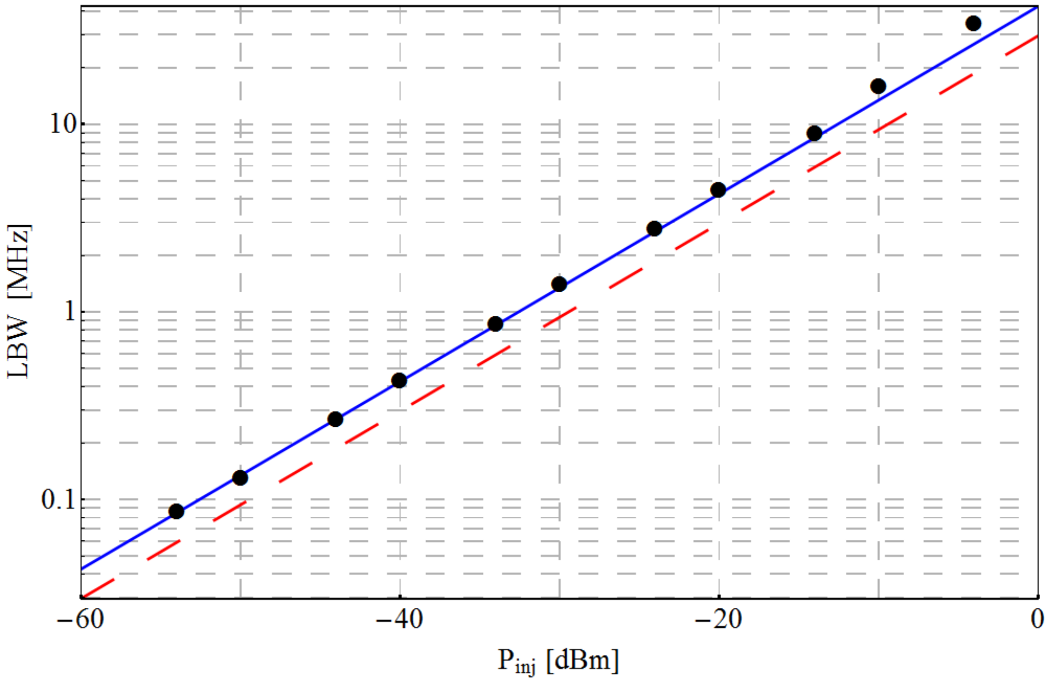

Fig. 5.14 – Comparison of locking-bandwidth calculations: previous theory (dashed red), this theory (solid blue), measurements (black dots).

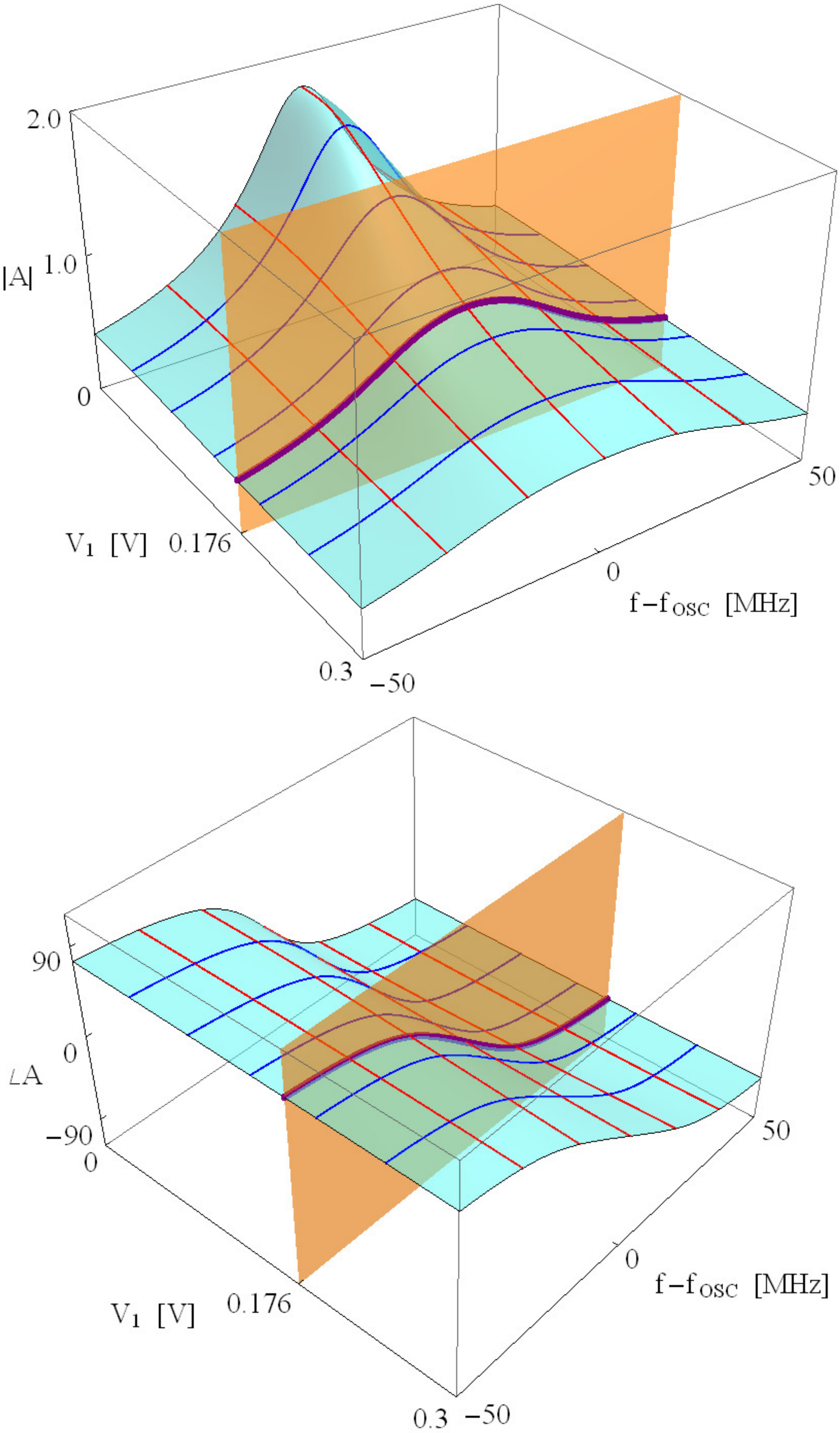

Fig. 5.15 – Three-dimensional dependence of amplitude (upper graphic) and phase (lower graphic) of $\mathbf{A}[V_1, 2\pi f]$ *on its variables, for circuit in Fig.5.12. Orange sections are at* $V_{1,OSC}$*.*

value of LBW_{LLI}. The situation corresponding to final design is depicted by Figs. 5.14 and 5.15. In the latter one, the dependence of amplitude and phase of $\mathbf{A}[V_1, \omega]$ on drive voltage V_1 and frequency $f = \omega/(2\pi)$ is illustrated, and oscillation amplitude of $V_1 \cong 0.176$ V is reported. Notice that the amplitude of the open-loop gain at free-running frequency and $V_1 \cong 0$ is around 1.78, leaving around +5 dB as gain margin for a robust oscillation buildup. The final value of the RLC Q-factor is ≈480, which corresponds to a loaded Q-factor of the linearized circuit of ≈435 (Q_{00} in present terminology), which further reduces, because of the nonlinear effects here accounted for, to ≈300 (Q_{OSC} in our terminology), i.e., 30% less than predicted by current theories adopting Adler's equation [28]. Such improvement in accuracy is clearly seen in the graph of Fig. 5.14, which compares the measured locking bandwidth (see [31]) with the simulated ones obtained adopting formula (5.19) or the classical one (with Ohira's Q-factor). A good agreement between prediction and experiments can be observed only in the first case.

Once more, it must be noticed that to achieve analogous accuracy in the locking bandwidth prediction, the only alternative is to adopt a transient envelope numerical simulation tool, such as the cited Circuit Envelope [41], which would require several repeated simulations in order to determine, by bracketing stable and unstable points, the band limit to within a reasonably tight tolerance. Furthermore, each one of these searches involves a long transient, even in a stroboscopic time scale, leading to an extremely long aggregate simulation time.

6. Semi-Numerical Analysis of High-Order ILOs

6.1 Overview on Presented Semi-Numerical Method

This chapter deals with the analysis of resonant structures different from simple single-tuned (or approximable as single-tuned) ones. As previously discussed, the employment of multiple tuned resonators can be exploited to achieve wider locking-bandwidths [37], and in those cases a ST-like approximation can lead to significant inaccuracies, both in terms of a quantitative respect and in terms of qualitative effects, not predictable without a proper resonator model.

For this purpose, a semi-numerical approach can be performed, modeling the oscillator tank and all linear subcircuits through numerical transfer functions, built from zeroes and poles, and developing a convenient procedure. This method permits to easily collect the required data even when the internal topology of the circuit is not known, or suitable models are not available, but the only chance (or the simpler one) is to identify data on the basis of direct measurements. The nonlinear element is represented through a polynomial multidimensional equation, exploiting nonlinear measurements provided by instrumentation or acquiring the data by means of regime simulations (HB).

This feature of proposed method has to be remarked, for design purposes in particular, in the microwave circuits field, where a trial and error design process is often demanded.

Furthermore, this approach permits a detailed study - also in the case of more complex circuits - of oscillator's behavior exhibited when the injection level is not low, providing information that is uncomfortable to be obtained through circuit's simulation. Semi-analytical prediction of well-known Arnold Tongues, in non-LLI conditions, has thus been drawn, while normally determined in ILOs only with experimental measurements.

An example clarifies in the end that presented formulas, though apparently complicated, are actually much simpler to apply than it may seem.

6.2 Analyzed ILO System Description and Specific Class Defining Conditions

The block-diagram of the system, introduced in Section 3.3, representing the generic ILO that will be here considered, is drawn again for convenience in Fig. 6.1. It features a general single-loop feedback structure. It comprises four linear blocks representing (appropriately grouped) the various passive elements of the system, and one nonlinear block representing the (unique) active device.

In the case of circuital systems, of principal interest in this environment, the structure of figure covers most of the ILOs: the nonlinear active one-port equipped RILOs, and several practical configurations of TILOs as well, in fact the active element there employed can be usually well approximated by a SISO nonlinearity. More precisely, it can be shown that all RILO circuits can be fit in the structure of Fig. 6.1, after proper identification of the $\mathbf{L}_x$ (with x = G, F, S, O) blocks. While not all TILO circuits are covered by the structure of figure, as better detailed later, many configurations of practical relevance can be. The main limitation is, in fact, the assumption of a single control variable for the nonlinear active device $\mathbf{N}[X_I]$, which can be considered a reasonable approximation in many feedback-type high-frequency TILOs designed exploiting modular/matched structures and nearly unilateral active devices.

Of course, the generality of the depicted structure has to be further specified in order to specifically address the class of fundamental-mode injection-locked oscillators here considered, in addition to class defining conditions already set in Sec. 3.3. Broadly speaking, such class can be identified as the class of "properly

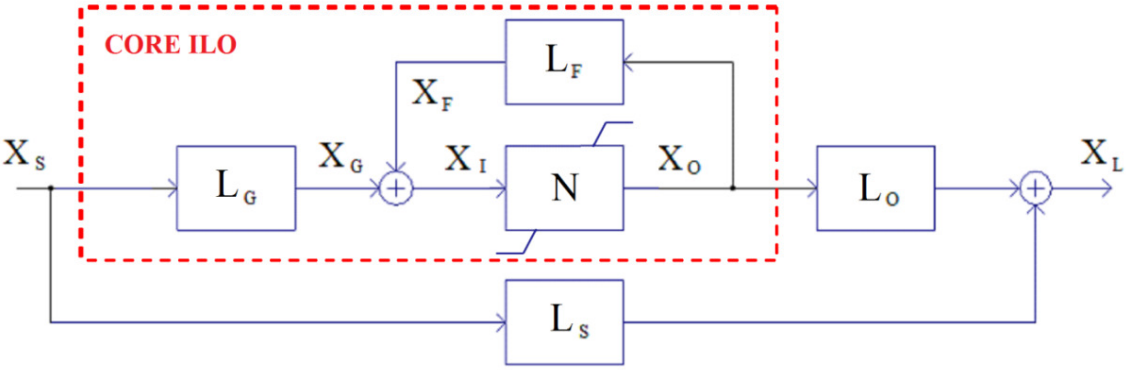

Fig. 6.1 – General block-diagram of the ILO system class considered, in the DCE domain.

designed" fundamental-mode ILOs, i.e., systems based on a quasi-sinusoidal (unimodal and self-starting) "core-oscillator" driven by a narrowband-modulated injection signal, with a carrier frequency in the neighborhood of the free-run oscillation one. Such requirement implicates, primarily, that the filtering block in the feedback path ($\mathbf{L}_F$) has to possess a "dominant resonance" with adequate selectivity and, also, that such quality is not compromised by the frequency response of the active block.

Above cited class-defining conditions, which will be formally defined in a perturbationally-rigorous manner in the following, guarantee a *quasi sinusoidal* (QS) behavior of both free running or entrained oscillation under steady-state locked operation and a *quasi sinusoidal quasi static* (QS^2) one under transient operation. Consequently, it is possible to develop present analysis in the fundamental-frequency DCE domain, as implicitly assumed in Fig. 6.1. In fact, all $\mathbf{X}_n$ (n = I, O, G, F, S, L) quantities appearing in this diagram are to be interpreted as generalized time-varying phasors: $\mathbf{X}_n = X_n[t] \cdot e^{j\phi_n[t]}$, where $X_n[t]$ and $\phi_n[t]$ are slowly-varying amplitude quantities in the scaled time t/T_O, and T_O is the period of the free-running oscillation. This is equivalent to considering their variations as "small" in the period of the fundamental of the oscillation under both free-running and phase-locked operation, which doesn't represent an actual restriction in usual cases.

As a first consequence, we can characterize the nonlinear active element directly in the frequency domain, by generalizing the classical SIDF concept to allow for an imaginary part, as well as a frequency dependence in addition to the amplitude one:

$$\mathbf{N}[X_I, \omega] = N_r[X_I, \omega] + j \cdot N_i[X_I, \omega] \tag{6.1}$$

The complex nature of such *Frequency-Dependent Describing Function* (FDDF) permits to model more accurately active devices adopted in high-frequency circuits, in which the non-negligible influence of parasitic (reactive, both linear and nonlinear) elements has to be adequately accounted for (consider, e.g., the negative-resistance diodes adopted in microwave RILOs [64,65], or parasitics in microwave common drain Colpitts circuits [68]).

Notice that the use of the SIDF (and therefore also of above defined FDDF) in the circuital context implicitly assumes that variations of the active device bias in the various operating conditions investigated is negligibly small or none. In addition to this rather common assumption, here we set a further one, i.e., that the active nonlinear block has an intrinsic bandwidth much wider than the one associated to the filtering linear block in the feedback path ($\mathbf{L}_F$). As obvious, in the case in view, in which the block diagram illustrated represents a properly designed/dimensioned quasi sinusoidal oscillator entrained by a nearly-synchronous sinusoidal injection signal, the associated high selectivity of the resonator $\mathbf{L}_F$ makes this assumption automatically verified in all practical situations. In fact, with respect to the main resonator, in a standard ILO design the parasitic elements associated to the active device will certainly turn out to be a minor perturbation of the dominant resonance associated to the main filter.

As a matter of fact, this last assumption would not be strictly required for the development of this theory, but will be declared anyhow since it doesn't imply an actual constraint on the class of treatable circuits/systems, while it simplifies considerably method's application in practice.

It is now possible to proceed further with the description of the class of systems under investigation, which can be broadly indicated as the ILO systems characterized by resonant structures of *Multiple-Tuned Nearly-Synchronous* (MTNS) dominant-resonance type, as formally defined below.

The four linear blocks $\mathbf{L}_x$ appearing in Fig. 6.1 are supposed to be characterized in the Laplace domain, through their transfer functions of polynomial rational nature in the complex-frequency "**s**" variable:

$$(6.2) \qquad \mathbf{L}_x[\mathbf{s}] = K_x \frac{\prod_{h=1}^{H_{xz}} (\mathbf{s}-\mathbf{s}_{xzh})}{\prod_{h=1}^{H_{xp}} (\mathbf{s}-\mathbf{s}_{xph})} \qquad \text{(where x = G, F, S, O)}$$

with the associated zeroes/poles described by their respective real and imaginary parts:

$$(6.3) \qquad \mathbf{s}_{xyh} = \sigma_{xyh}+j\cdot\omega_{xyh} \qquad (x = G, F, S, O;\; y = z, p;\; h = 1, ..., H_{xy})$$

As a matter of fact, two possible situations arise when dealing with actual circuits. One possibility is that the topology (and element values) of the circuits constituting the various blocks are known, i.e., the $\mathbf{L}_x$ are of "glass-box" type. The other possibility is that the various blocks are characterized as a whole, i.e., the $\mathbf{L}_x$ are of "black-box" type. In the first case, if the circuit elements of a given block are all of lumped nature, the model described by (6.2) follows directly. On the other hand, if one or more distributed elements are present, or if the block is of black-box type, the casting of the transfer function associated to it into the form (6.2) would require a proper identification in the complex-frequency **s**-domain. However, it can be noticed that the subsequent development of our procedure will simplify this step significantly, that can be developed in a narrowband way, directly with reference to a real-frequency ω-domain characterization of the block.

In order to express in a perturbatively rigorous manner our QS^2 class-defining conditions on linear and nonlinear blocks, it is first necessary to determine the value of a normalizing, reference frequency ω_R ("a priori" estimate of oscillation frequency), as well as to identify the "smallness parameter" ε which characterizes our weakly nonlinear system. Since such choices are not critical (to within reasonable tolerance limits detailed later), they can be made in several ways, depending also on which type of information on the system is available when performing this step.

Indeed, such initial guess can exploit, in addition to the stated high-selectivity of the loop filter $\mathbf{L}_F$, the here assumed parasitic nature of the reactive components of the nonlinearity $\mathbf{N}[X_I, \omega]$, by referring either to the Nyquist diagram of the open-loop gain of the linearized system ($\mathbf{OLG}_0 = \mathbf{L}_F[\omega]\cdot\mathbf{N}[0, \omega]$), or directly to the poles of $\mathbf{L}_F[\mathbf{s}]$. Notice that these quantities are anyhow required for other purposes, first of all the preliminary verification of the correct stability properties of the linearized system. In fact, the assumed unimodal quasi-sinusoidal oscillation startup from noise for the core-oscillator implies the existence of a unique unstable resonant mode, i.e., two complex-conjugate natural frequencies $s_U = \sigma_U \pm j\omega_U$ with $\sigma_U > 0$, and $\sigma_U/\omega_U \ll 1$. In the "glass-box" case, direct (numerical) determination of eigenvalues is possible, and such verification step is straightforward. Also, both ω_R and ε can be defined directly in terms of this unstable mode, through the relationships:

$$(6.4) \qquad \textit{glass-box case:} \begin{cases} \omega_R = \omega_U \\ \varepsilon = \dfrac{2\sigma_U}{\omega_U} = \dfrac{1}{Q_U} \end{cases}$$

the latter grounding on the common association of ε to the inverse of a quality factor.

In the "black-box" case, the simplest solution, but usually adequate, is to designate the reference frequency ω_R as the (unique) "decreasing-phase" crossover frequency of the Nyquist diagram of (1-$\mathbf{OLG}_0$). As to ε, we can associate it to the group delay of $\mathbf{OLG}_0$ (τ_g) evaluated at ω_R, leading to these relationships:

$$(6.5) \qquad \textit{black-box case}: \begin{cases} \omega_R = \omega : \mathrm{Im}[\mathbf{OLG}_0[\omega]] = 0, \text{ with } \dfrac{d[\arg[1\text{-}\mathbf{OLG}_0]]}{d\omega} < 0 \\[2ex] \varepsilon = \dfrac{2}{\tau_g[\omega_R] \cdot \omega_R} \end{cases}$$

$$\tau_g[\omega] = -\frac{d[\arg[\mathbf{OLG}_0]]}{d\omega}$$

We can now continue our analysis by introducing an expedient partitioning of all poles/zeroes, observing that they can always be subdivided into three types, in relation to their position in the complex plane. Such subdivision, whose justification will be explained in next section, relies on whether a given pole/zero contributes to the dominant resonance (type-1) or to "out of band" parasitic resonances (type-2) or aperiodic modes (type-3), all typically present in practical systems also in case of correctly dimensioned ILOs.

Type-1 poles and zeroes, appearing in complex-conjugate pairs ($\sigma_{xyh} \pm j\omega_{xyh}$), will be in number of $2 \cdot H_{xp1}$ and $2 \cdot H_{xz1}$, respectively. Similarly, type-2 pairs of poles or zeroes are in number of $2 \cdot H_{xp2}$ and $2 \cdot H_{xz2}$. Type-3 poles and zeroes will be in number of H_{xp3} and H_{xz3} respectively. Of course, $H_{xy} = 2 \cdot H_{xy1} + 2 \cdot H_{xy2} + H_{xy3}$.

It is now possible to formally state the specific QS^2 class-defining (sufficient) conditions. About linear blocks, we require that all type-1 poles/zeroes of $\mathbf{L}_F$ and $\mathbf{L}_G$ satisfy the following asymptotic relationships:

$$(6.6) \qquad \begin{array}{l} \left| \dfrac{\omega_{xyh} - \omega_R}{\omega_R} \right| = O[\varepsilon] \\[2ex] \left| 2 \dfrac{\sigma_{xyh}}{\omega_R} \right| = O[\varepsilon] \end{array} \qquad (x = G, F;\ \ y = z, p;\ \ h = 1, \ldots, H_{xy1})$$

with $H_{Fp1} > 0$, which guarantee their grouping in two square clusters nearby the imaginary axis in the neighborhoods of $\pm j\omega_R$, and therefore a dominant resonance in $\mathbf{L}_F$, at least. Equations (6.6) can be also considered as a formal definition of the MTNS tank and coupling circuits characterizing the extended class of ILOs being considered.

For the nonlinear element it is required, in the frequency band associated to type-1 poles/zeroes:

$$\left|\mathbf{N}[X_I,\omega]\cdot\mathbf{L}_F[\omega]\right| = O[1] \tag{6.7a}$$

$$\left|\frac{\partial\,\mathrm{Im}[\mathbf{N}[X_I,\omega]]}{\partial\,\omega}\right| \ll \left|\frac{\partial\,\mathrm{Im}[\mathbf{L}_F[\omega]^{-1}]}{\partial\,\omega}\right| \tag{6.7b}$$

$$\left|\frac{\partial\,\mathbf{N}[X_I,\omega]}{\partial\,\omega}\cdot\frac{\omega_R}{\mathbf{N}[X_I,\omega_R]}\right| = O[1] \tag{6.7c}$$

which guarantee that the active device has a "level" compatible with the assumed weakly-nonlinear nature of the overall system, and that it is adequately wideband and does not interfere with the dominant resonance of the filter $\mathbf{L}_F$.

As to the constraints on injection signal, already qualitatively indicated as narrowband-modulated with a carrier in the neighborhoods of the free-running oscillation frequency, they will be detailed in next section, since relying on quantities still to be introduced.

6.3 Dynamical System Model Derivation

Let's start the derivation of the ILO-system dynamical model with a standard steady-state analysis in the fundamental ω-frequency domain, assuming an entrained operation under the action of a CW synchronizing signal. From the block diagram of Fig. 6.1, stem the basic relationships:

$$\begin{aligned}
&\mathbf{X}_G + \mathbf{X}_F = \mathbf{X}_I\\
&\mathbf{X}_G = \mathbf{L}_G[\omega]\cdot\mathbf{X}_S\\
&\mathbf{X}_F = \mathbf{L}_F[\omega]\cdot\mathbf{X}_O\\
&\mathbf{X}_G = \mathbf{L}_O[\omega]\cdot\mathbf{X}_O + \mathbf{L}_S[\omega]\cdot\mathbf{X}_S\\
&\mathbf{X}_O = \mathbf{N}[X_I,\omega]\cdot\mathbf{X}_I
\end{aligned} \tag{6.8}$$

Combining above equations, we obtain the frequency-domain nonlinear phasor equation:

$$(1 - \mathbf{L}_F[\omega] \cdot \mathbf{N}[X_I, \omega]) \cdot \mathbf{X}_I = \mathbf{L}_G[\omega] \cdot \mathbf{X}_S \tag{6.9}$$

characterizing the "core-ILO" subsystem (delimited by dashed red rectangle in Fig. 6.1), to which can be added the auxiliary equation:

$$\mathbf{X}_L = \mathbf{L}_O[\omega] \cdot \mathbf{N}[X_I, \omega] \cdot \mathbf{X}_I + \mathbf{L}_S[\omega] \cdot \mathbf{X}_S \tag{6.10}$$

which permits to evaluate the overall ILO output variable $\mathbf{X}_L$, once $\mathbf{X}_I$ is calculated.

For the purpose of subsequent development, it is convenient to introduce a frequency scaling with respect to ω_R, by replacing $\mathbf{L}_F[\omega]$ and $\mathbf{L}_G[\omega]$ with their normalized counterparts, appropriately partitioned in order to highlight the three types of poles/zeroes above introduced:

$$\begin{aligned}
&\mathcal{L}_x[\Omega] \equiv \mathcal{K}_x \cdot \mathcal{L}_{x1}[\Omega] \cdot \mathcal{L}_{x2}[\Omega] \cdot \mathcal{L}_{x3}[\Omega] \\
&\mathcal{L}_{x1}[\Omega] \equiv \frac{\prod_{h=1}^{H_{xz1}} (j\Omega-\mathscr{s}_{xzh})(j\Omega-\mathscr{s}_{xzh}{}^{*})}{\prod_{h=1}^{H_{xp1}} (j\Omega-\mathscr{s}_{xph})(j\Omega-\mathscr{s}_{xph}{}^{*})} \\
&\mathcal{L}_{x2}[\Omega] \equiv \frac{\prod_{h=H_{xz1}+1}^{H_{xz1}+H_{xz2}} (j\Omega-\mathscr{s}_{xzh})(j\Omega-\mathscr{s}_{xzh}{}^{*})}{\prod_{h=H_{xp1}+1}^{H_{xp1}+H_{xp2}} (j\Omega-\mathscr{s}_{xph})(j\Omega-\mathscr{s}_{xph}{}^{*})} \\
&\mathcal{L}_{x3}[\Omega] \equiv \frac{\prod_{h=H_{xz1}+H_{xz2}+1}^{H_{xz1}+H_{xz2}+H_{xz3}} (j\Omega-\mathscr{s}_{xzh})}{\prod_{h=H_{xp1}+H_{xp2}+1}^{H_{xp1}+H_{xp2}+H_{xp3}} (j\Omega-\mathscr{s}_{xph})}
\end{aligned} \tag{6.11}$$

where:

$$\begin{aligned}
&\Omega \equiv \frac{\omega}{\omega_R} \\
&\mathscr{s}_{xyh} \equiv \frac{s_{xyn}}{\omega_R} \quad (x = G, F;\ \ y = z, p;\ \ h = 1, ..., H_{xy1}+ H_{xy2}+ H_{xy3};\ \ n = 1, ..., H_{xy}) \\
&\mathcal{K}_x \equiv \frac{K_x}{\omega_R{}^{H_{xp}-H_{xz}}}
\end{aligned} \tag{6.12}$$

The frequency normalization now performed is particularly useful to avoid numerical issues (e.g., overflow or underflow) during practical implementation of the theory. Notice the reordering of the scaled poles/zeroes s_{xyh} (implied by h≠n) to account for the adopted numbering of complex-conjugate pairs. According to (6.6), the type-1 s_{xyh} can be rearranged to highlight the intrinsic dependence on ε quantity:

$$s_{xyh} = \varepsilon\,\Gamma_{xyh} + j(1 + \varepsilon\,\Delta\Omega_{xyh}) \quad (x = G, F;\ \ y = z, p;\ \ h = 1, \ldots, H_{xy1}) \tag{6.13}$$

where:

$$\begin{aligned} &\Gamma_{xyh} \equiv \frac{\sigma_{xyh}}{\varepsilon\,\omega_R} \\ &\Delta\Omega_{xyh} \equiv \frac{\omega_{xyh} - \omega_R}{\varepsilon\,\omega_R} \\ &\left|\Gamma_{xyh}\right| = O[1] \\ &\left|\Delta\Omega_{xyh}\right| = O[1] \end{aligned} \tag{6.14}$$

We can now perform a main step of presented approach toward the derivation of the dynamical equations of our MTNS ILO class starting from the frequency-domain phasor equation (6.9). In so doing, we can adapt to this more general system the perturbation-refined technique introduced in [21] by Calandra and Sommariva, formalizing a semi-numerical method with easier application. The unique "order truncation" step there performed had a twofold role: the elimination of spurious modes that arise in the time-domain to dynamical-phasor transformation of network variables, and the order-equalization all other quantities. While the first target, associated to frequency related terms, is a required one, the second one is not. More important, the original procedure adopted for high-order circuits, corresponding to our subclass of MNTS-RILOs, though rigorous, is rather cumbersome to apply in practice, precisely because of this combined goal which requires to apply order-truncation only after an intermediate dynamical model is derived from the (glass-box type) circuit equations.

Here, with the purpose of extending the method to black-box systems and to simplify practical usage, the separation of the two above cited steps is proposed, by developing a generalized "*one side band*" (OSB) version of the BLDO algebra introduced in [24]. This goal is achieved, first, by observing that, in force of the above stated class-defining conditions, it is possible to investigate the dynamics of the system focusing on the fundamental frequency band alone. We can thus exploit the separation of poles/zeroes into three types and employ only type-1 roots. Moreover, we will apply only the mandatory frequency-truncation step, directly replacing the $\{\mathbf{L}_x,\ x = G, F\}$ set with its one side band counterpart:

$$\overline{\mathcal{L}_x}[\Omega] \equiv \mathcal{K}_{x0} \cdot \overline{\mathcal{L}_{x1}}[\Omega] \tag{6.15}$$

with:

$$\overline{\mathcal{L}_{x1}}[\Omega] \equiv \frac{\prod_{h=1}^{H_{xz1}} (j\Omega - \mathcal{s}_{xzh})}{\prod_{h=1}^{H_{xp1}} (j\Omega - \mathcal{s}_{xph})} \tag{6.16}$$
$$\mathcal{K}_{x0} \equiv \mathcal{L}_x[1]/\overline{\mathcal{L}_{x1}}[1]$$

For the purpose of practical application of our method, such $\{\overline{\mathcal{L}_x}\}$ set can be considered as the starting point in the setup of an OSB counterpart of the block diagram of the core-ILO in Fig. 6.1.

Through the above definitions, the truncated counterpart of (6.9) can be written:

$$\left(1 - \mathcal{K}_{F0} \frac{\prod_{h=1}^{H_{Fz1}} (j\Omega - \mathcal{s}_{Fzh})}{\prod_{h=1}^{H_{Fp1}} (j\Omega - \mathcal{s}_{Fph})} \mathbf{N}[X_I, \omega]\right) \mathbf{X}_I = \left(\mathcal{K}_{G0} \frac{\prod_{h=1}^{H_{Gz1}} (j\Omega - \mathcal{s}_{Gzh})}{\prod_{h=1}^{H_{Gp1}} (j\Omega - \mathcal{s}_{Gph})}\right) \mathbf{X}_S \tag{6.17}$$

It is now convenient to introduce the *Least Common Polynomial Multiple* (LCPM) in the $j\Omega$ variable between the denominators of $\overline{\mathcal{L}_F}[\Omega]$ and $\overline{\mathcal{L}_G}[\Omega]$, and its associated maximum order $H \leq H_{Fp1} + H_{Gp1}$:

$$\mathcal{P}_{LCPM}[\Omega] = \mathrm{LCPM}\left[\prod_{h=1}^{H_{Fp1}} (j\Omega - \mathcal{s}_{Fph}), \prod_{h=1}^{H_{Gp1}} (j\Omega - \mathcal{s}_{Gph})\right] = \prod_{h=1}^{H} (j\Omega - \mathcal{s}_{ph}) \tag{6.18}$$

Introducing a renaming (into $\mathcal{s}_{Ah}$ and $\mathcal{s}_{Bh}$) of the residual roots of the two polynomials in $j\Omega$ obtained by the divisions:

$$\prod_{h=1}^{H-H_{Fp1}} (j\Omega - \mathcal{s}_{Ah}) \equiv \frac{\mathcal{P}_{LCPM}[\Omega]}{\prod_{h=1}^{H_{Fp1}} (j\Omega - \mathcal{s}_{Fph})} \tag{6.19a}$$

$$\text{(6.19b)}\qquad \prod_{h=1}^{H-H_{Gp1}}(j\Omega-\mathscr{s}_{Bh}) \equiv \frac{\mathcal{P}_{LCPM}[\Omega]}{\prod_{h=1}^{H_{Gp1}}(j\Omega-\mathscr{s}_{Gph})}$$

and after rearranging, we obtain the in-line equation:

(6.20)

$$\left(\left(\prod_{h=1}^{H}(j\Omega-\mathscr{s}_{ph})\right)-\mathcal{K}_{F0}\left(\prod_{h=1}^{H-H_{Fp1}}(j\Omega-\mathscr{s}_{Ah})\right)\left(\prod_{h=1}^{H_{Fz1}}(j\Omega-\mathscr{s}_{Fzh})\right)\mathbf{N}[X_I,\Omega]\right)\cdot \mathbf{X}_I e^{j\phi_I} =$$

$$= \mathcal{K}_{G0}\left(\prod_{h=1}^{H-H_{Gp1}}(j\Omega-\mathscr{s}_{Bh})\right)\left(\prod_{h=1}^{H_{Gz1}}(j\Omega-\mathscr{s}_{Gzh})\right)\cdot \mathbf{X}_S e^{j\phi_S}$$

After explicitation of the ε quantity embedded into $\{\mathscr{s}_{Ah}\}$, $\{\mathscr{s}_{Bh}\}$ and $\{\mathscr{s}_{ph}\}$ in analogy to what done in (6.13), and introduction of the normalized detuning $\Delta\Omega = (\Omega-1)/\varepsilon$, we can rearrange (6.20) in its order-equalized counterpart:

(6.21)

$$\left(\left(\prod_{h=1}^{H}\left(-\Gamma_{ph}+j(\Delta\Omega-\Delta\Omega_{ph})\right)\right)-\mathcal{K}_{A}\left(\prod_{h=1}^{H-H_{Fp1}}(-\Gamma_{Ah}+j(\Delta\Omega-\Delta\Omega_{Ah}))\right)\cdot\right.$$

$$\left.\cdot\left(\prod_{h=1}^{H_{Fz1}}(-\Gamma_{Fzh}+j(\Delta\Omega-\Delta\Omega_{Fzh}))\right)\mathcal{N}[X_I]\right)\cdot \mathbf{X}_I e^{j\phi_I} =$$

$$= \mathcal{K}_{B}\left(\prod_{h=1}^{H-H_{Gp1}}(-\Gamma_{Bh}+j(\Delta\Omega-\Delta\Omega_{Bh}))\right)\left(\prod_{h=1}^{H_{Gz1}}(-\Gamma_{Gzh}+j(\Delta\Omega-\Delta\Omega_{Gzh}))\right)\cdot \mathbf{X}_S e^{j\phi_S}$$

where :

$$\text{(6.22)}\qquad \begin{aligned} \mathcal{K}_A &\equiv \frac{\mathcal{K}_{F0}\varepsilon^{H_{Fz1}-H_{Fp1}}}{|\mathcal{L}_F[1]|} \\ \mathcal{K}_B &\equiv \mathcal{K}_{G0}\varepsilon^{H_{Gz1}-H_{Gp1}} \\ \mathcal{N}[X_I] &\equiv |\mathcal{L}_F[1]|\cdot \mathbf{N}[X_I,1] \end{aligned}$$

Notice that, in force of above assumptions, $|\mathcal{K}_A|$, $|\mathcal{K}_B/\mathcal{L}_G[1]|$ and $|\mathcal{N}[X_I]|$ are all O[1].

It has also to be remarked that, in the intermediate calculations that led to (6.21), $\mathcal{N}[X_I]$, the normalized counterpart of $\mathbf{N}[X_I, \omega]$, has lost its dependence on frequency since its wideband nature (6.7) causes the additional terms stemming from such dependence, being all of smaller order than the other terms, which ones only are thus retained. This fact has an important practical consequence, in that it simplifies significantly the nonlinear modeling of the active device for our purposes. Indeed, just a simple 1D fitting of fixed-frequency, swept-amplitude CW measurements (or simulations) is involved.

Setting $X_S=0$ into (6.21), provides the algebraic homogeneous equation whose equilibrium points define the set of possible free-running regimes, identified by one or more pairs $\{X_{IO}, \Delta\Omega_O\}$, whose individual dynamical stability will be investigated later. However, for the sake of simplicity, this treatment will usually suppose a single free-running regime.

Notice that, while no order constraints apply to the unnormalized oscillation amplitude X_{IO}, the normalized detuning $\Delta\Omega_O$ between the free-run oscillation and reference frequencies is bound to be O[1].

It is now convenient to formally state the "proper injection" conditions for the fundamental mode of operation investigated, which actualize in:

$$\text{(6.23)}\qquad \begin{aligned} &\frac{\left|\mathcal{L}_G[\Omega]\cdot\mathcal{D}^m X_S\right|}{X_{IO}} = O[1] \;\;;\;\; (m = 1, \ldots, M) \\ &\left|\mathcal{D}^m \phi_S\right| = O[1] \qquad\qquad ;\;\; (m = 1, \ldots, M) \\ &\frac{\left|\mathcal{L}_G[\Omega]\right|\cdot X_S}{X_{IO}} = O[1] \\ &\left|\Delta\Omega\right| = O[1] \\ &M = H - H_{Gp1} + H_{Gz1} \end{aligned}$$

where $\mathcal{D} = d/d\tau$ is the symbolic differentiation operator in the scaled time $\tau = \varepsilon\cdot\omega_R\cdot t$. Qualitatively, they correspond to the assumption of a narrow-band modulated (or unmodulated) drive signal, of amplitude commensurate to the oscillation strength and carrier frequency in the neighborhoods of the free-running one.

Regularity conditions (6.6), (6.7) and (6.23) are sufficient to guarantee the QS^2 nature of the system investigated, quantitatively corresponding to the asymptotic constraints:

(6.24)
$$\frac{|\mathcal{D}^n X_I|}{X_{I0}} = O[1] \;\; ; \quad (n = 1, ..., N)$$
$$\left|\mathcal{D}^n \phi_I\right| = O[1] \;\; ; \quad (n = 1, ..., N)$$
$$N = \max[H, H - H_{Fp1} + H_{Fz1}]$$

where N is the stroboscopic order of the system at hand.

In force of (6.24) and of the OSB frequency-truncations above performed, it can now be derived the dynamical equation governing the entrained oscillation simply by replacing into (6.21) the scaled injection frequency detuning $\Delta\Omega$ with $\Delta\Omega - j\mathcal{D}$, which is the equivalent of the $j\omega$ replacement into $j\omega + d/dt$:

(6.25)
$$\left(\left(\prod_{h=1}^{H}(\mathcal{D} - \Gamma_{ph}+j(\Delta\Omega-\Delta\Omega_{ph}))\right) - \mathcal{K}_A\left(\prod_{h=1}^{H-H_{Fp1}}(\mathcal{D} - \Gamma_{Ah}+j(\Delta\Omega-\Delta\Omega_{Ah}))\right)\cdot\right.$$
$$\left.\cdot\left(\prod_{h=1}^{H_{Fz1}}(\mathcal{D} - \Gamma_{Fzh}+j(\Delta\Omega-\Delta\Omega_{Fzh}))\right)\mathcal{N}[X_I]\right)\cdot \mathbf{X}_I e^{j\phi_I} =$$
$$= \mathcal{K}_B\left(\prod_{h=1}^{H-H_{Gp1}}(\mathcal{D} - \Gamma_{Bh}+j(\Delta\Omega-\Delta\Omega_{Bh}))\right)\left(\prod_{h=1}^{H_{Gz1}}(\mathcal{D} - \Gamma_{Gzh}+j(\Delta\Omega-\Delta\Omega_{Gzh}))\right)\cdot \mathbf{X}_S e^{j\phi_S}$$

Quantities $\{X_I, \phi_I, X_S, \phi_S, \mathcal{N}[X_I]\}$, although not explicitly indicated, are meant to be functions of the scaled time τ.

Above OSB-DCE equation (6.25) is a main result of our study. It permits the complete investigation of the behavior (steady-state, dynamical stability and transient operation) of a large class of ILOs under all operating conditions of practical meaningfulness. On its basis, in next section a specific application will highlight some behavioral aspects of the phenomena occurring in ILOs of high-order, or under high-level injection (HLI), which received so far minor attention in the literature compared to second-order systems or low-level injection (LLI) operation.

It can be remarked that the complex equation (6.25) can be always split into two coupled ODEs, solved for the maximum degree derivatives, of the form:

$$(6.26)\qquad \begin{aligned} \mathcal{D}^N X_I &= \mathcal{F}_X\left[X_I, \{\mathcal{D}^n X_I\}, \phi_I, \{\mathcal{D}^n \phi_I\}; \{n = 1, ..., N\text{-}1\}\right] \\ \mathcal{D}^N \phi_I &= \mathcal{F}_\phi\left[X_I, \{\mathcal{D}^n X_I\}, \phi_I, \{\mathcal{D}^n \phi_I\}; \{n = 1, ..., N\text{-}1\}\right] \end{aligned}$$

in which, for compactness, the scaled time dependence and the injection-related quantities have been omitted.

System (6.26) can be rearranged in normal form:

$$(6.27)\qquad \mathcal{D} \cdot \underline{y} = \underline{f}[\underline{y}]$$

where

$$(6.28)\qquad \begin{aligned} \underline{y} &= \left[X_I,\ \phi_I, \mathcal{D}^1 X_I, \mathcal{D}^1 \phi_I, ..., \mathcal{D}^{N\text{-}1} X_I, \mathcal{D}^{N\text{-}1} \phi_I\right]^T \\ \underline{f}[\underline{y}] &= \left[y_3, y_4, ..., y_{2N\text{-}1}, y_{2N}, \mathcal{F}_X, \mathcal{F}_\phi\right]^T \end{aligned}$$

which is more handy for the practical evaluation of transient response through numerical integration, as well as for the dynamical stability analysis.

Before concluding this section, an additional note can be mode. In those (rare) cases in which the maximum numerical precision obtainable by this method is required, an iterative approach can be adopted for the refinement of the value of ω_R, and, consequently, the value of $\mathcal{N}[X_I]$. The more reasonable choice is to set, in each cycle, the value of ω_R equal to the oscillation frequency calculated at the previous iteration. Notice that a good metric of the quality of the selected value of ω_R is constituted directly by the size of $\Delta\Omega_O$, zero value indicating that optimal choice has been made.

6.4 Locking Bandwidth Calculation and LLI operation

As discussed in previous chapters, locking-bandwidth is one of the principal features of an ILO. To ascertain if a given equilibrium point calculated by the fundamental mode spectral balance equation (6.21) under CW injection corresponds to locked or unlocked regime, a dynamical stability analysis has to be carried out. By exploiting the differential model (6.28), this step is easily performed through the associated Jacobian matrix:

$$\underline{\underline{J}} = \left[\begin{array}{cccc} \multicolumn{2}{c|}{\underline{\underline{0}}_{(2N-2)\times(2)}} & \multicolumn{2}{c}{\underline{\underline{I}}_{(2N-2)\times(2N-2)}} \\ \hline D_1\mathcal{F}_X & D_2\mathcal{F}_X & \ldots \; D_{2N-1}\mathcal{F}_X & D_{2N}\mathcal{F}_X \\ D_1\mathcal{F}_\phi & D_2\mathcal{F}_\phi & \ldots \; D_{2N-1}\mathcal{F}_\phi & D_{2N}\mathcal{F}_\phi \end{array}\right] \qquad (6.29)$$

where:

$$D_n\mathcal{F}_X = \frac{\partial\, \mathcal{F}_X}{\partial\, y_n}$$

$$D_n\mathcal{F}_\phi = \frac{\partial\, \mathcal{F}_\phi}{\partial\, y_n} \qquad (6.30)$$

and then deriving the characteristic polynomial from (3.25), as previously described in chapter 3.

As it is well-known, its roots determine the eigenvalues, whose nature establishes whether a perturbation of the investigated equilibrium point will decay (i.e., stable regime) or increase (i.e. unstable regime) with time. Of course, actual evaluation of eigenvalues is not a required step, as already pointed out. Other common methods, such as Routh-Hurwitz stability criterion, can provide equivalent information and can be adopted as well.

It can be remarked that an important application of the above developed dynamical stability analysis is the one pertaining the analysis of equilibrium point(s) $\{\Delta\Omega_O, X_{IO}\}$ associated to the free-run operation, which is indeed the first one usually performed in an ILO analysis or design stage, as already seen in Sec. 3.5. To this purpose, the involved characteristic polynomial (p_{CO}) can be calculated from the free-run counterpart of (6.29-6.30), which is obtained by particularizing $\mathcal{F}_X$ and $\mathcal{F}_\phi$ for $X_S = 0$, and then dividing the resulting p_C by λ. Notice that, if more than one stable free-running equilibrium point is ascertained to exist, the ILO design has probably to be revised, to avoid potential multimodality problems, unless that situation was intentionally created, e.g., for band-widening purposes.

Only after this test, it can be investigated the stability analysis of the driven oscillator, in a given point $\{\Delta\Omega, X_{I,SS}\}$, performing a "locking stability" study. A wider look at stability properties of the system can be observed if evaluating Locus and Boundary conditions, in the response space $\{X_S, \Delta\Omega, X_{I,SS}\}$, equivalent to a "parametric" investigation of stable regimes.

Therefore, joining steady-state equation (6.21) together with Locus and Boundary

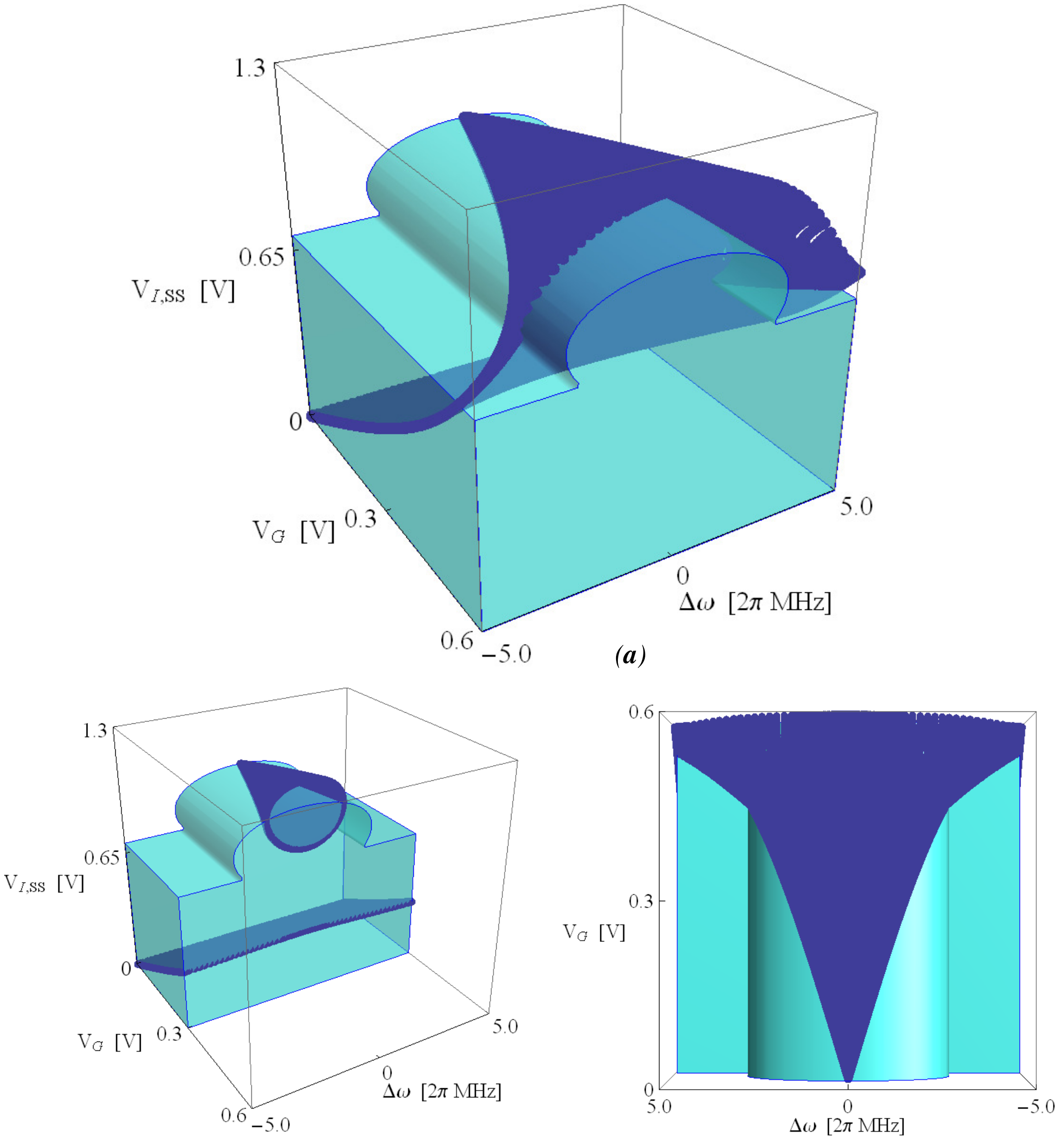

(a)

(b)

(c)

Fig. 6.2 – 3D space $\{X_S, \Delta\omega, X_{I,SS}\}$ with stability borders (transparent cyan color) and superimposed steady-state curves (dark blue), with reference to example of Fig. 3.3 (i.e., space is $\{V_G, \Delta\omega, V_{I,SS}\}$). (a) full 3D graphic; (b) low-level injection only, emphasizing linear region; (c) view from the top, showing locking-bandwidth limits (Arnold Tongue).

conditions, we can finally obtain the graphical representation of stability limits in the response space, and Arnold Tongues as the projection of the intersection points on $\{\Delta\Omega, X_S\}$ plane.

A simple single-tuned case (the same analyzed in chapter 3) of this 3D illustration is depicted in Fig. 6.2, where 3D curves pertaining with regime points (dark blue color), and Locus/Boundary stability borders (transparent cyan color) graphically outline the whole LBW, under low- and high-level injections. This illustration shows the mentioned stability space $\{X_S, \Delta\omega, X_{I,SS}\}$ of this basic example including a main graphic (Fig. 6.2a), a second one limited to lower injection levels (Fig. 6.2b), which emphasizes the linear dependence of LBW_{LLI} from X_S, while last one (Fig. 6.2c) provides a view from the top of the main picture, highlighting the profile of the Arnold Tongue.

With such a global picture of the locking bandwidth, it is possible to realize that, especially in cases different from ST-like ones, like MTNS systems, a simple LLI analysis can prove absolutely unsatisfactory. Usually, this type of simplified investigation is considered a good approximation until HLI is reached (that is, with definition introduced in Sec. 3.6, where the maximum frequency detuning is determined by the Boundary limit), but examples in following sections will point out that it is not always true, i.e., in some cases an intermediate region must be considered. This leads to the need of the introduction of a *medium-level injection* (MLI), as the region where the LBW is not well approximated by the LLI standard analysis (i.e., a linear one), but where the injection is not "high" yet. This novel definition, from a practical perspective, obviously means different algorithms need to be implemented, but a much better agreement with actual results will demonstrate its usefulness, since arbitrarily extending LLI up to HLI region can produce relevant errors.

In order to deepen this new approach, and make a clear comparison, the study of LLI approximation must be performed first. To obtain the LLI version of the dynamical equations that lead to the Adler-type (linear) relationship between LBW and Xs, we can apply a proper perturbative "secondary simplification".

In particular, the following order conditions are to be supposed:

$$\begin{aligned} & X_S = O[\varepsilon] \\ & \Delta\Omega_{SO} = O[\varepsilon] \\ & \mathcal{D}^n \Delta X_I = O[\varepsilon^{n+1}] \\ & \mathcal{D}^n \phi_I = O[\varepsilon^n] \end{aligned} \tag{6.31}$$

where the incremental variables $\Delta\Omega_{SO} = \Delta\Omega - \Delta\Omega_O$ and $\Delta X_I = X_I - X_{IO}$ have been introduced, which express the scaled detuning between the injection source and oscillation frequencies, and the difference between entrained and free-running oscillation amplitude, respectively.

Making use of (6.31) into DCE equation (6.25), and truncating it to the minimum ε-order (i.e., eliminating all higher order terms), after appropriate rearranging, we eventually get an algebraic-differential system of the form:

$$\begin{aligned} & \Delta X_I[\tau] = X_S\left(K_{Xc}\cos\left[\phi_I[\tau]\right] + K_{Xs}\sin\left[\phi_I[\tau]\right]\right) \\ & \mathcal{D}\phi_I[\tau] = -\Delta\Omega_{SO} + X_S\left(K_{\phi c}\cos\left[\phi_I[\tau]\right] + K_{\phi s}\sin\left[\phi_I[\tau]\right]\right) \end{aligned} \tag{6.32}$$

where the four $K_{(\cdot)(\cdot)}$ coefficients are real valued numbers, all O[1].

Equation set (6.32) generalizes the classical Adler-type differential model adopted for the LLI operation analysis. Unlike other derivations, the above proposed one provides a consistent and rigorous theoretical basis for the LLI model calculation. An LLI locking-bandwidth novel formula is then derived, first solving above equations under steady-state conditions, then performing some further calculations. It finally results, employing above defined normalized quantities:

$$\mathcal{LBW}_{LLI} = 2\sqrt{K_{\phi c}{}^2 + K_{\phi s}{}^2}\; X_S \tag{6.33}$$

Although (6.33) correctly describes the initial part of ILO Arnold Tongues, characterized by an ω_O-centered, symmetrical and linearly dependent on X_S locking bandwidth, it has to be remarked that it cannot be safely adopted outside the validity range defined by conditions (6.31). So far, the LLI range has been defined in a rather qualitative manner, and LBW_{LLI} usually extrapolated to X_S values well above the ones guaranteeing a reasonably accurate calculation. This practitioner's habit can be partly justified by the fact that the separation between LLI and HLI is rather sharp in single-tuned like systems, and arbitrary extension of LLI range up to this switchover point does not involve excessive inaccuracy in such simple systems. On the other hand, as shown in next example section, when more complex tank and coupling circuits are involved, as in the general MTNS case, the MLI range that joins LLI and HLI is characterized by a LBW with a nonlinear dependence on X_S. Blindly using LBW_{LLI} in place of the correct LBW can thus involve significant inaccuracies, especially considering the fact that the useful range of injection values adopted in practical situations often falls in that MLI range. Summing up, notwithstanding the attractive simplicity of the LLI analysis, a full analysis (MLI and HLI) is thus necessary to determine, at least, if the range of X_S values to be handled permits to adopt the LLI simplification without excessive errors or not.

Overall theory has been tested and verified by applying it to several examples. In following section, a "not quite simple" circuit is presented, as it will be clear soon.

6.5 Example of Application

1) General Analysis and Nonlinear Block

As example of application of the exposed method, it has been chosen a double-tuned circuit employing a tunnel diode (depicted in Fig. 6.3, values in Tab. 6.1), similar to the circuit structure proposed by Kurokawa in [37] to obtain a wider locking bandwidth, where several parasitics elements have been added. In picture, a biasing and stabilizing network is visible, followed by the fourth order tank-and-coupling network, while R_0 load resistor, together with V_S injection voltage, represents the simplest model of an ideal circulator (at the right side of section "B"). The two resonators (L_1/C_1 parallel, L_2/C_2 series) carry two natural frequencies in the surrounding of 1 GHz, with a relative asynchronicity between them of 7.5 MHz. In this example, L_X linear functions have been chosen to be obtained from circuit white-box topology, with an analytical method, to achieve a wider generality. It would be equally possible to start from numerical L_X transfer functions, which would obviously lead to simpler steps. Nonlinear resistor is represented by a polynomial function (see eq. 3.16) of an high degree (seventh), in order to better fit the trend of a tunnel diode. For nonlinear capacitance, classic Nanavati tunnel diode

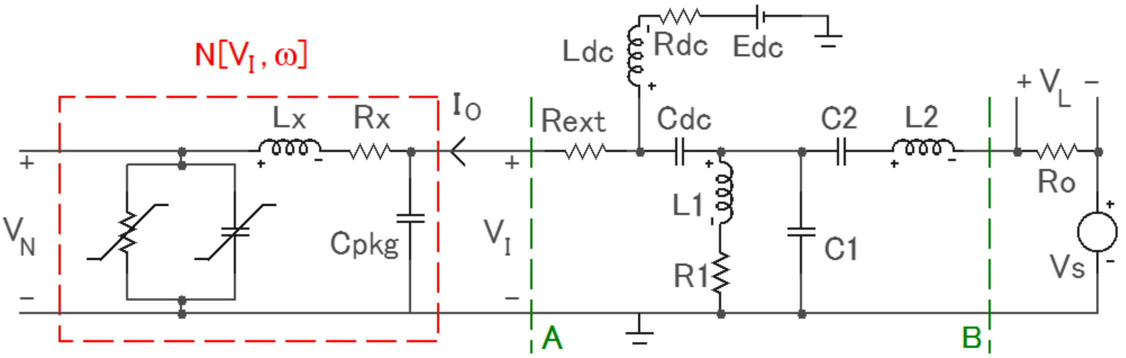

Fig. 6.3 – Double-tuned tunnel diode injection locked oscillator circuit diagram.

$g_{n0} = 0$	$g_{n1} = 0.124113$	$g_{n2} = -0.37968$	$g_{n3} = 0.783802$
$g_{n4} = -7.58186$	$g_{n5} = 27.3113$	$g_{n6} = -37.0946$	$g_{n7} = 17.6641$

$C_{J0} = 1.5$ pF	$V_\phi = 0.67$ V	FC = 0.85
$R_X = 0.3\ \Omega$	$L_X = 0.15$ nH	$C_{PKG} = 1$ pF

*(**a**)*

$E_{DC} = 0.39$ V	$R_{DC} = 10\ \Omega$	$L_{DC} = 22\ \mu$H	$C_{DC} = 220$ nF	$R_{EXT} = 4.7\ \Omega$

*(**b**)*

$L_1 = 52.85$ pH	$R_1 = 1.11$ mΩ	$C_1 = 475.7$ pF
$L_2 = 599$ nH	$C_2 = 0.0426$ pF	$R_0 = 50\ \Omega$

*(**c**)*

*Tab. 6.1 – Parameters of example circuit of Fig. 6.3. (**a**) tunnel diode with parasitics, (**b**) biasing and stabilization network, (**c**) tank and coupling network and circulator.*

model [69] has been instead employed:

$$C[v_N[t]] = C_{J0} \Big/ \left(1 - \frac{v_N[t]}{V_\phi}\right)^2 \qquad (6.34)$$

where the (conventional) limiting in its derivative has been added, fixed when $v_N[t]$ exceeds $FC \cdot V_\phi = 0.5695$ V. The capacitance corresponding to tunnel bias point (bias fixed at $v_{N,DC} = 0.3$ V, $i_{N,DC} = 6$ mA) is about 4.92 pF.

Since we suppose to have at disposition the "real" element, including its parasitics, we chose to proceed to a black-box approach for $\mathbf{N}[V_I, \omega]$, fitting what is seen at the left of section "A" in figure with a polynomial function of two variables, i.e., seventh degree function of V_I, fifth degree function of ω. The employment of such an high degree guarantees an optimal match of numerical results with the ones that could be obtained by an analytical approach. Since of their large quantity, those 48 complex coefficients are not reported here, and has been preferred a graphical representation (Fig. 6.4).

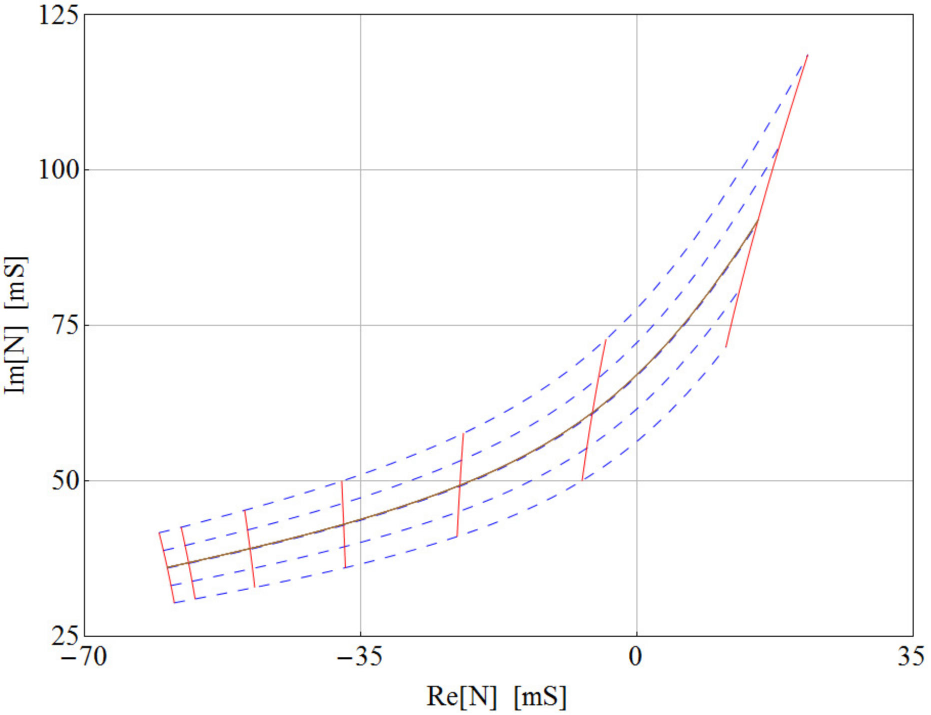

Fig. 6.4 – Graphical representation of $\mathbf{N}[V_I, \omega]$*: red lines have constant* V_I *(from 0 to 0.3 V, a step every 50 mV), with f swept from 0.85GHz a 1.15GHz; dashed blue lines have constant f (from 0.85GHz to 1.15GHz, a step every 75MHz), with* V_I *swept from 0 to 0.3 V. Brown curve corresponds to constant frequency value of* $\omega_R/(2\pi)$*.*

2) *Linear Blocks*

From circuit topology, some involved voltages and currents are directly identified ($\mathbf{X}_I = \mathbf{V}_I$, $\mathbf{X}_O = \mathbf{I}_O$, $\mathbf{X}_S = \mathbf{V}_S$), while the remaining ones are indirectly found ($\mathbf{X}_G = \mathbf{X}_I|_{X_O=0}$, $\mathbf{X}_F = \mathbf{X}_I|_{X_S=0}$). This way, $\mathbf{L}_G$ and $\mathbf{L}_F$ are calculated through the relationships $\mathbf{X}_G/\mathbf{X}_S$ and $\mathbf{X}_F/\mathbf{X}_O$, respectively. Notice that $\mathbf{L}_F$ here corresponds to impedance seen by section "A", looking at right hand side, in absence of any injection signal. Similarly, $\mathbf{L}_S$ and $\mathbf{L}_O$ are obtained, producing on the whole the following transfer functions:

(6.35)

$$\mathbf{L}_G = \frac{0.00008889\, s_G^2(0.00007234 + s_G)(0.003346 + s_G)}{5.233\cdot 10^{-9} + 0.00007235\, s_G + s_G^2 + 0.01685\, s_G^3 + 2\, s_G^4 + 0.01670\, s_G^5 + s_G^6}$$

$$\mathbf{L}_F = -\frac{4.7(1.637\cdot 10^{-8} + 0.0002263 s_G + s_G^2 + 0.08782\, s_G^3 + 2.001 s_G^4 + 0.08804\, s_G^5 + s_G^6)}{5.233\cdot 10^{-9} + 0.00007235\, s_G + s_G^2 + 0.01685\, s_G^3 + 2\, s_G^4 + 0.01670\, s_G^5 + s_G^6}$$

$$\mathbf{L}_S = \frac{0.5(5.233\cdot 10^{-9} + 0.00007235 s_G + s_G^2 - 0.009917 s_G^3 + 2\, s_G^4 - 0.009865 s_G^5 + s_G^6)}{5.233\cdot 10^{-9} + 0.00007235\, s_G + s_G^2 + 0.01685\, s_G^3 + 2\, s_G^4 + 0.01670\, s_G^5 + s_G^6}$$

$$\mathbf{L}_O = -\frac{0.004444\, s_G^2(0.00007234 + s_G)(0.003346 + s_G)}{5.233\cdot 10^{-9} + 0.00007235\, s_G + s_G^2 + 0.01685\, s_G^3 + 2\, s_G^4 + 0.01670\, s_G^5 + s_G^6}$$

where $s_G = \mathbf{s}/(2\pi\cdot 10^9)$ has been introduced for compactness. A graphical representation of these functions is depicted in Fig. 6.5.

3) *Angular Reference Frequency*

For the choice of ω_R, we firstly calculate $\mathbf{OLG}_0$ (see Section 6.2) and, after some calculations, we obtain $\omega_R = 2\pi\cdot 1.00315$ GHz and $\varepsilon = 0.01346$. As described in the theory, $\mathbf{OLG}_0$ has been evaluated also because it can be adopted to verify the wideband linear stability, therefore ensuring that system under analysis has only one possible self-starting oscillation. In this example, treatable as a white-box since its topology is known, eigenvalues are found, as a comparison, producing $\omega_R = 2\pi\cdot 0.99250$ GHz and $\varepsilon = 0.01601$. The difference in ε value is not relevant, since its value is not critical, but only its order of magnitude.

About the goodness of the choice of ω_R, it must be remarked that, if high precision is required, its value can be improved with iterations of the whole

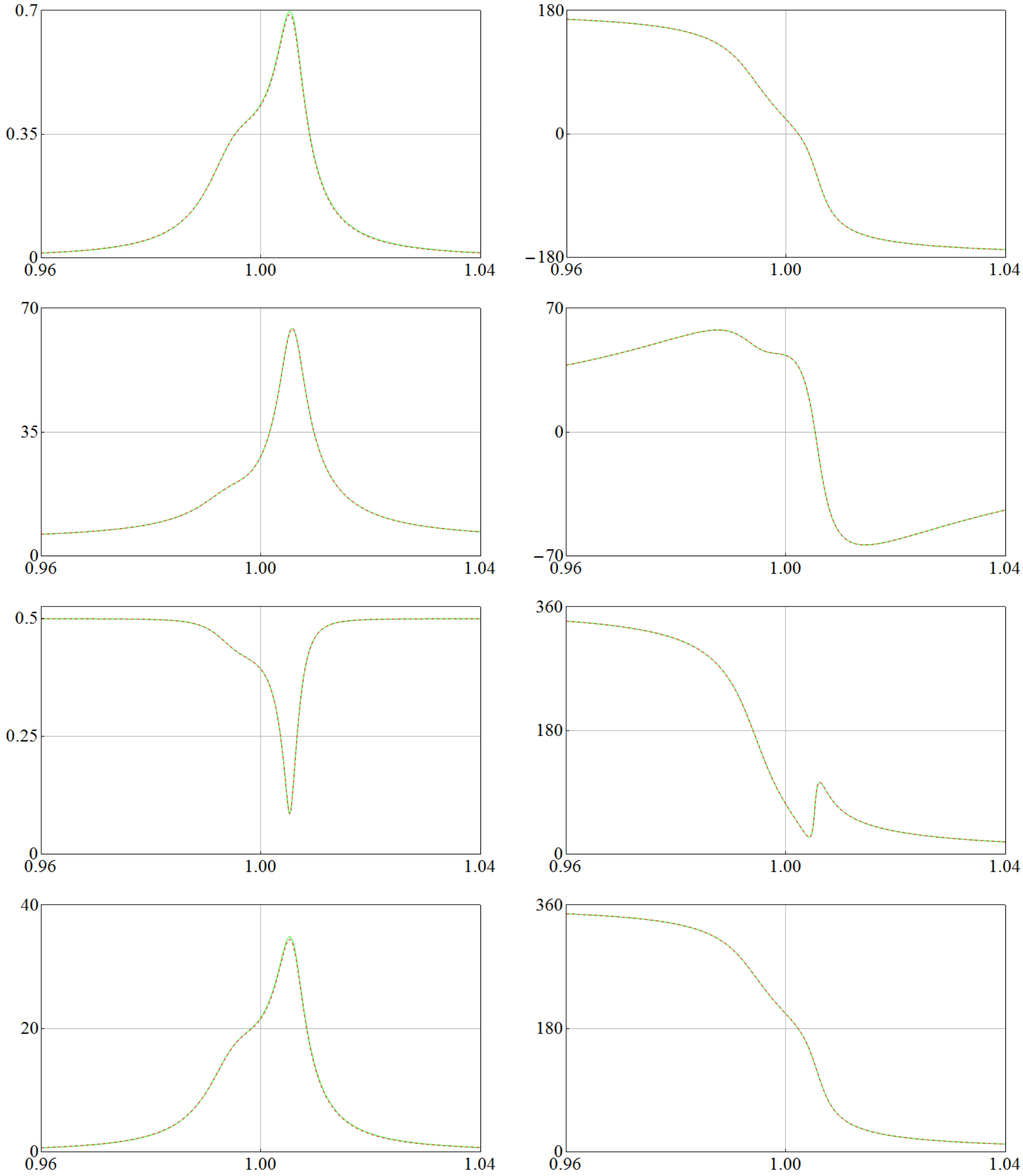

Fig. 6.5 – Linear blocks transfer functions over frequency (GHz), amplitude (left) and phase (right, in degrees). From top to bottom: L_G, L_F, L_S, L_O. Superimposed to L_X functions (green lines) are OSB $\overline{\mathcal{L}_X}$ functions (dashed red lines), even though differences are imperceptible.

procedure. In this case, as second iteration, the f_{OSC} value obtained below can be employed as the new starting $\omega_{R(2)} = 2\pi\cdot 0.99251$ GHz, which immediately converges to definitive value: $2\pi\cdot f_{OSC(2)} = 2\pi\cdot f_{OSC(\infty)} = \omega_{R(\infty)} = 2\pi\cdot 0.99264$ GHz. As easily noticeable, value provided by eigenvalues is significantly more precise, but this doesn't compromise method's validity.

In following accounts, it has been employed the set provided by black-box analysis, in order to evaluate all results in the worst case.

4) N-Block Conditions

Now, conditions (6.7) for block **N** are verified, observing a positive validation. Please note that these inequalities are generally respected in practical cases. In this example, inside observation bandwidth, the following values are obtained:

$$\text{(6.36a)}\qquad \max\left[\left|\mathbf{N}[V_I,\,\omega]\cdot\mathbf{L}_F[\omega]\right|\right]\approx 4.5 = O[1]$$

$$\text{(6.36b)}\qquad \max\left[\left|\frac{\partial\,\mathrm{Im}[\mathbf{N}[V_I,\,\omega]]}{\partial\,\omega}\right|\right]\approx 8\cdot 10^{-12}\ll 3\cdot 10^{-10}\approx \min\left[\left|\frac{\partial\,\mathrm{Im}[\mathbf{L}_F[\omega]^{-1}]}{\partial\,\omega}\right|\right]$$

$$\text{(6.36c)}\qquad 0.5<\left|\frac{\partial\,\mathbf{N}[V_I,\,\omega]}{\partial\,\omega}\cdot\frac{\omega_R}{\mathbf{N}[V_I,\,\omega_R]}\right|<1.9$$

5) Normalized Linear Functions and Types Identification

Once ω_R is defined, normalized $\mathcal{L}_F[\mathcal{S}]$ and $\mathcal{L}_G[\mathcal{S}]$ functions can be obtained, where $\mathcal{S} = \mathbf{s}/\omega_R$ (thus similar to 6.35 representation), and zeroes and poles can be partitioned into three types, as previously described:

$\mathcal{L}_F[\mathcal{S}]$	*zeroes*	*type-1*	-0.03646 ± j 1.00023 -0.007314 ± j 0.9929
		type-2	-0.000113 ± j 0.00006
		type-3	*(none)*
	poles	*type-1*	-0.005760 ± j 0.9911 -0.002528 ± j 1.0026
		type-2	-0.000036 ± j 0.00006
		type-3	*(none)*
$\mathcal{L}_G[\mathcal{S}]$	*zeroes*	*type-1*	*(none)*
		type-2	*(none)*
		type-3	-0.003335 -0.000072 0 0

$\mathcal{L}_G[\mathcal{S}]$	*poles*	*type-1*	$-0.005760 \pm j\,0.9911$ $-0.002528 \pm j\,1.0026$
		type-2	$-0.000036 \pm j\,0.00006$
		type-3	*(none)*

6) *L-Blocks Conditions*

Conditions (6.6) are easily validated:

$$\begin{aligned} &\max\left[\left|\frac{\omega_{xyh} - \omega_R}{\omega_R}\right|\right] = 0.008851 \cong 0.7\varepsilon = O[\varepsilon] \\ &\max\left[\left|2\frac{\sigma_{xyh}}{\omega_R}\right|\right] = 0.07291 \cong 5\varepsilon = O[\varepsilon] \end{aligned} \tag{6.37}$$

7) *OSB-Truncated Functions*

It's finally possible to describe $\overline{\mathcal{L}_{F1}}[\Omega]$ and $\overline{\mathcal{L}_{G1}}[\Omega]$, which, respectively multiplied for $\mathcal{K}_{F0}$ and $\mathcal{K}_{G0}$, produce $\overline{\mathcal{L}_F}[\Omega]$ and $\overline{\mathcal{L}_G}[\Omega]$ OSB functions:

$$\begin{aligned} &\overline{\mathcal{L}_{F1}}[\Omega] = \frac{(0.9929 + j\,0.04351) - (1.993 + j\,0.04377)\,\Omega + \Omega^2}{(0.9937 + j\,0.008281) - (1.994 + j\,0.008288)\,\Omega + \Omega^2} \\ &\overline{\mathcal{L}_{G1}}[\Omega] = \frac{1}{(0.9937 + j\,0.008281) - (1.994 + j\,0.008288)\,\Omega + \Omega^2} \\ &\mathcal{K}_{F0} = -\,4.699 + j\,84.08\cdot 10^{-3} \\ &\mathcal{K}_{G0} = -\,22.15 - j\,18.17\cdot 10^{-9} \end{aligned} \tag{6.38}$$

8) *LCPM*

The Least Common Polynomial Multiple, whose function is simply to transform (6.17) in an in-line equation, results, in this example where $\overline{\mathcal{L}_F}[\Omega]$ and $\overline{\mathcal{L}_G}[\Omega]$ share the same denominator (as usual for circuital cases), equal to either of the two:

$$\mathcal{P}_{LCPM}[\Omega] = (0.9937 + j\,0.008281) - (1.994 + j\,0.008288)\,\Omega + \Omega^2 \tag{6.39}$$

9) *Steady-State Equation*

Equation (6.20), characterizing the steady-state regime, results for this example:

$$\begin{aligned}&\left(\mathcal{P}_{LCPM}[\Omega] - \mathcal{K}_{F0}\cdot \mathrm{Num}[\overline{\mathcal{L}_{F1}}[\Omega]] \cdot \mathbf{N}[V_I, \Omega]\right) \cdot \mathbf{V}_I e^{j\phi_I} = \\ &\qquad = \mathcal{K}_{G0} \cdot \mathrm{Num}[\overline{\mathcal{L}_{G1}}[\Omega]] \cdot \mathbf{V}_S e^{j\phi_S}\end{aligned} \tag{6.40}$$

where (6.38-6.39) provide numerical values for above quantities, and $\mathrm{Num}[\overline{\mathcal{L}_{x1}}[\Omega]]$ has been adopted to indicate the numerator of $\overline{\mathcal{L}_{x1}}[\Omega]$ (with x = F, G). The normalized counterpart of this equation, corresponding to (6.21), is reported in Appendix A3 (equation A3.2), and is employed for graphics drawn in Fig. 6.6.

10) *Normalized Function for N-Block*

From (6.22) we can proceed to the determination of $\mathcal{N}[V_I]$, which, on the basis of what has been so far described, obviously emerge as a polynomial function of seventh degree in the only V_I variable:

$$\begin{aligned}\mathcal{N}[V_I] &= (-2.727 + j\,1.654) + (0.05886 + j\,0.1032)V_I + \\ &+ (46.41 + j\,6.394)V_I^2 + (96.59 + j\,208.4)V_I^3 - (1398 + j\,2765)V_I^4 + \\ &+ (7288 + j\,18702)V_I^5 - (21851 + j\,62556)V_I^6 + (28213 + j86344)V_I^7\end{aligned} \tag{6.41}$$

Similarly, last coefficients are found:

$$\begin{aligned}\mathcal{K}_A &= -0.1026 + j\,1.835\cdot 10^{-3} \\ \mathcal{K}_B &= 0.1222 + j\,0.1002\cdot 10^{-3}\end{aligned} \tag{6.42}$$

11) *Injection Conditions*

Equations (6.23) define the conditions for maximum injection amplitude and maximum (normalized) acceptable detuning. In particular:

$$\begin{aligned}\max[V_S] &= O[0.233\ \mathrm{V}] \\ \max[|\Delta\Omega|] &= O[1]\end{aligned} \tag{6.43}$$

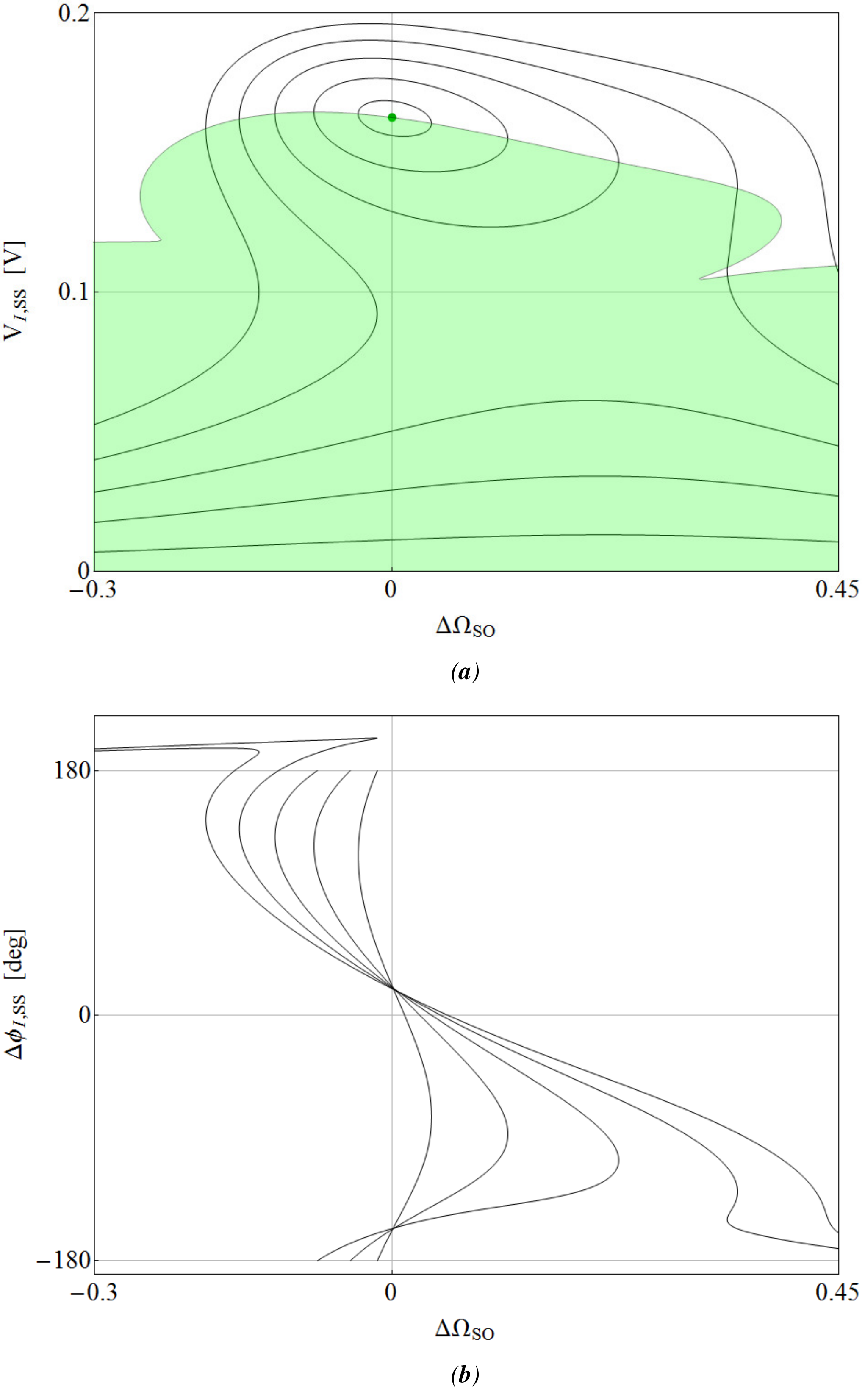

*Fig. 6.6 – Steady-state curves of: (**a**) $V_{I,SS}[\Delta\Omega_{SO}, V_S]$ with stability regions superimposed; (**b**) $\phi_{I,SS}[\Delta\Omega_{SO}, V_S]$ for stable branches only. V_S = 20 mV, 50 mV, 80 mV, 110 mV, 140 mV.*

establish that maximum injection amplitude must be order of 0.233 V, e.g. $V_S = 1$ V would be acceptable, while $V_S = 10$ V would not. Maximum corresponding unnormalized detuning frequency is order of 13.5 MHz.

12) DCE Equations

DCE system, corresponding to (6.26) equation set, was obtained from the numericized (6.25) counterpart with some simple steps, but since it results extremely long (several pages) it is here omitted for the sake of brevity, though it is detailed in Appendix A3 (see equation A3.3). This formula is employed for the study of transient evolutions.

13) Locking Stability

From previous equation we can calculate Jacobian matrix and, by its means, we can immediately ascertain that the only free-running oscillation ($V_{IO} = 0.1626$ V, $\Delta\Omega_O = -0.7877$, equivalent to an oscillation frequency of 0.99251 GHz) is stable, because associated eigenvalues' real parts are all negative quantities:

$$\lambda_1 = -0.4159; \quad \lambda_2 = -0.4139 + j\,0.4853; \quad \lambda_3 = -0.4139 - j\,0.4853 \tag{6.44}$$

Afterwards, steady-state curves and stability borders are drawn, achieved by numerical means. These pictures are in Fig. 6.6, where both amplitude and phase regimes have been displayed.

14) Locking Bandwidth (HLI, MLI, LLI)

Solving numerically the intersection of stability equations and steady-state equations, locking bandwidth bound to Locus (MLI) and Boundary (HLI) limits are eventually obtained. The LLI approximation is given by the equation set:

$$\begin{aligned} \Delta V_I[\tau] &= V_S\left(0.254311\cos\left[\phi_I[\tau]\right] + 0.193757\sin\left[\phi_I[\tau]\right]\right) \\ \mathcal{D}\phi_I[\tau] &= -\Delta\Omega_{SO} + V_S\left(0.689621\cos\left[\phi_I[\tau]\right] - 1.69507\sin\left[\phi_I[\tau]\right]\right) \end{aligned} \tag{6.45}$$

resulting therefore:

$$\mathcal{LBW}_{\mathrm{LLI}} = 2\sqrt{K_{\phi c}{}^2 + K_{\phi s}{}^2}\ V_S = 3.66 \cdot V_S \tag{6.46}$$

which, unnormalized, corresponds (in Hertz) to:

$$\mathrm{LBW}_{\mathrm{LLI}} = 49.432 \cdot 10^6 \cdot V_S \tag{6.47}$$

Graphic of all of these locking limits is illustrated in Fig. 6.7, where the upper part of the Locus limit, i.e., the only influent at LLI level (see lower injection steady-state curves in Fig. 6.6), is drawn in green color. It is manifest from picture that LLI approximation (dashed magenta line) is not accurate beyond about 40 mV.

The other half of the Locus limit (the lower part) is the red curve. The orange line corresponds to the Boundary border, while the black dots were obtained through laborious ADS/CE simulation, whose disadvantages have already been profusely discussed in previous chapters. It must be remarked that the slight difference noticeable at high injection level is due to a different value in the central (oscillation) frequency, i.e., the overall bandwidth is approximately correct since it is mainly a shift in evaluated frequencies.

Comparison with Ohira's $\mathrm{LBW}_{\mathrm{LLI}}$ value [28] is not possible in this example, since the parasitic nonlinear capacitance inside the nonlinear element is not covered by its theory.

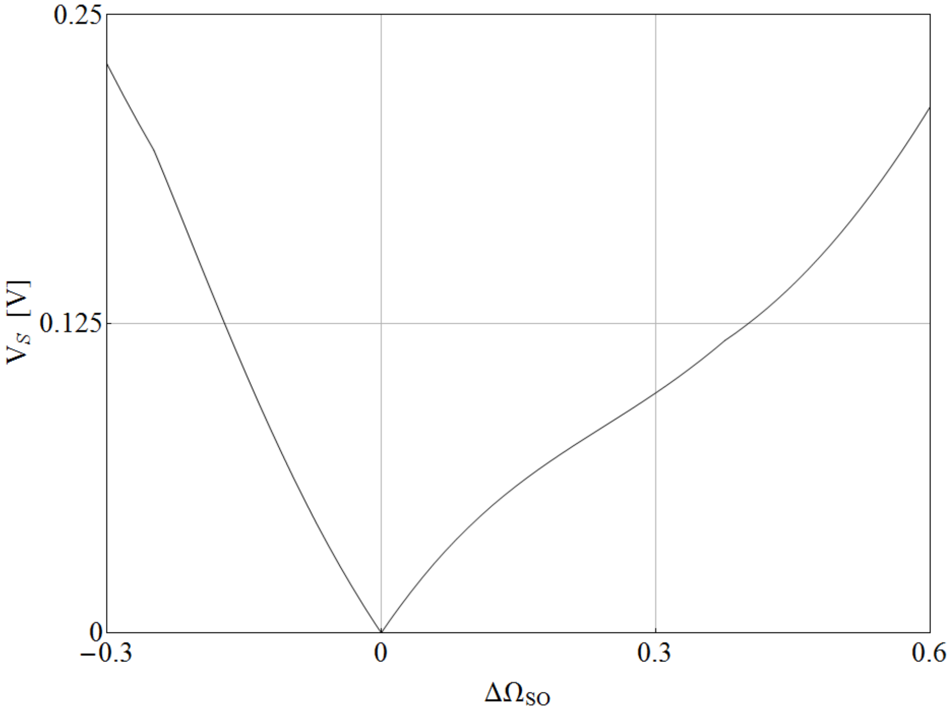

*(**a**)*

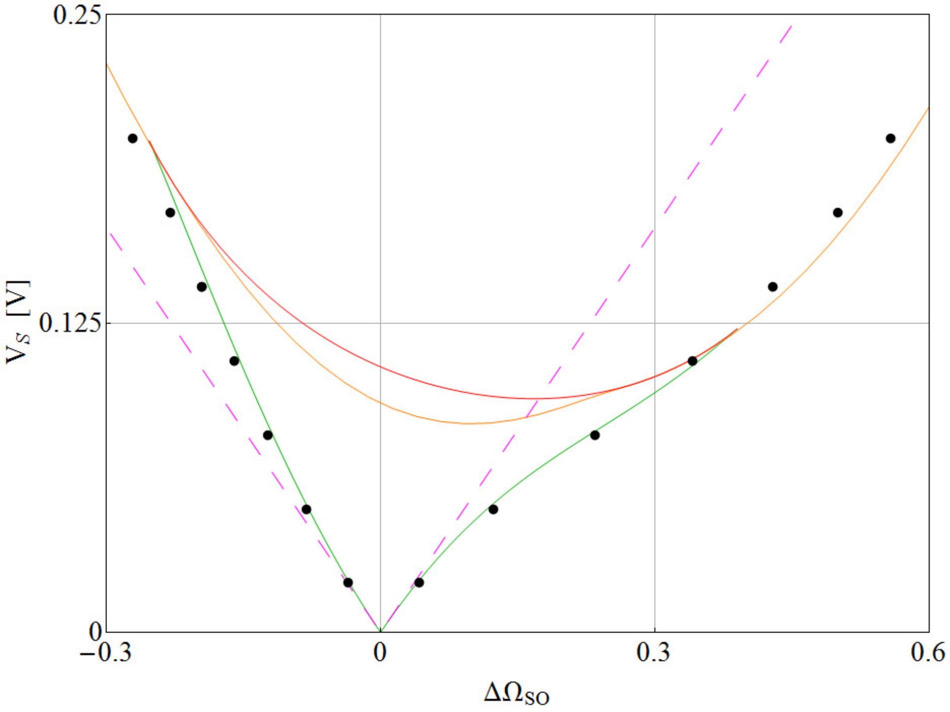

*(**b**)*

*Fig. 6.7 – Locking bandwidth for example of Fig 6.3. Figure (**a**) depicts overall bandwidth, while in figure (**b**) single branches for MLI/HLI limits are represented: Lower Locus limit (red), Upper Locus limit (green), Boundary limit (orange). LLI approximation is the dashed magenta line. Black dots represent ADS/CE simulations.*

7. Conclusions and Future Work

In this thesis work, the problem of developing a unified analysis method for computer-assisted simulation, in the frequency domain, of the steady-state and dynamical response of fundamental mode injection-locked oscillators was addressed and, to a good extent, solved. The key point has been a proper combination of analytical, perturbation-theory based, and numerical techniques, so that the high order differential model associated to the complex practical circuit structures characterizing modern ILOs can be treated in a semi-analytical way. In fact the "reduced" stroboscopic nonlinear differential model that approximates, in a perturbationally rigorous first-order exact manner, the dynamics of the entrained oscillation can be built directly in terms of an accurate, measurement or simulation based, characterization of the resonant structure and of the active element, with no need for over-simplification of the actual data, as instead required by other analytical methods of the literature, making the proposed technique, among all available ones, the most suitable in various cases.

On the other hand, with respect to purely numerical approaches employing state of the art simulation techniques in the frequency domain (as it is discussed in introduction, time-domain simulators are not at all suited for such stiff class of circuits), as the "Circuit Envelope" available in the Agilent EEsof ADS suite, the semi-analytical method proposed has the advantage of giving a better insight into phenomena and is thus more adapt to design-oriented use. It can also be noticed that, while the class of treatable circuits is not so wide as for the general-purpose CE simulation engine of ADS, this limitation is more theoretical than practical for the specific design task of ILOs here being focused on, since all "well-designed" real-world RILO configurations are treatable, and so are most of the TILO configurations currently adopted in the technical practice. It has also to be remarked that ADS/CE shares with all other purely numerical approaches the specific disadvantage of not landing to an efficient evaluation of the locking-bandwidth of an ILO, and even less to its optimization. This feature is instead embedded into the stability analysis of the proposed approach which permits a direct numerical evaluation of LBW no matter the injection signal amplitude, with no need for time-consuming iterated analysis for the search of the locking boundaries. A further positive feature of such stability analysis is that, in case of low-level injection, it transits in a smooth way into an explicit LBW calculation, in a manner similar to the Adler-like simplified methods commonly applied in the technical practice but without the associated applicability limitations.

Of course, with respect to the use of ADS/CE – or other analogous general-purpose simulation software tools in the dynamical complex envelope domain that could be developed in the future – the non purely-numerical nature of the proposed approach requires some additional preliminary steps to determine the "one side band" (OSB) model of the resonant structure and the fundamental frequency domain model of the active device. However, as the method application to practical circuits has shown, in performing such tasks, one can take a significant advantage of the use of any of the several EDA tools (e.g., an HB-based one, for best efficiency and integration) and/or of the symbolic-analysis software packages nowadays available in the market. As discussed above, such additional effort appears more than balanced by the availability of a semi-analytic explicit and compact nonlinear differential model describing the ILO dynamics, as the presented examples testify.

Among the several indirect results coming out from the extensive application of the method (in its various development phases) to the investigation of practical ILO configurations, at least one has to be highlighted. It is the importance of introducing, between the classical "low-level" and "high-level" injection a third range: the "medium-level" of injection. In its regard, it can be first noticed that this operating mode is not evident in "single-tuned like" configurations where the error in bandwidth evaluation extending the LLI simplified calculation up to the HLI limits is quite small, and can thus be neglected. A quite different situation occurs when the more modern MTNS tank and coupling network adopted for band-widening purposes are involved. In this case, as well illustrated by the example of Section 6.5, the LLI formula for LBW provides inaccurate predictions at injection levels quite lower than the HLI limits. Differently stated, the "normal" injection levels for such class of ILOs do require the use of an unabridged (MLI or HLI) formulation, if reliable results are sought for. The investigation performed has demonstrated that the common belief that an initial design of an ILO can be developed with reference to an Adler-like formulation is not grounded, not theoretically nor practically.

Before concluding, it can be pointed out that, notwithstanding the very encouraging results already achieved, some additional tasks are still required to bring to completion the work done, by aggregating the individual aspects of the developed theory into a unified one. In fact, the last months' investigation (not yet published) has clearly shown that not much additional work, with respect to what presented here, is needed to combine the semi-numerical generalized OSB devised analysis approach with a multiply-controlled nonlinear model of the active device. This would permit to extend to more general circuit topologies the preliminary work already done in accounting for the bias-shift phenomena as well as the (nonlinear) dependence of active two-ports not only on input but also on output signal amplitudes. As a matter of fact, with some more effort, it could be also possible to extend the proposed technique to account for lower/higher harmonics in addition to the fundamental one, not only to improve accuracy of simulation (which would not be required in case of properly designed ILOs, as previously remarked) but also, and more importantly, to extend the applicability to harmonic/subharmonic injection, thus permitting the investigation and the design of injection-locking based frequency dividers and multipliers, whose interest in practical application in low-power integrated circuits has greatly increased over the last few years.

Appendices

A1. Comparison Between Step-by-Step Procedures for LBW Evaluation: EDA Simulations vs. Proposed Method

With regards to algorithms of interest for the specific purpose, among the simulation techniques actually implemented on commercial EDA tools, the main ones are available in well-known *Agilent EEsof Advanced Design System* (ADS) simulation software [22]. It will be considered as the reference for comparisons in this section, also because it is the most widely used in its field, nevertheless.

In order to evaluate the locking-bandwidth of an ILO circuit, some steps are required when adopting an EDA tool, such as the one under test. First of all, of course, time is needed to set the system up by creating the schematic with desired models and instructing the correct simulation's parameters. Then, an Harmonic Balance simulation (in "oscillator mode") must be performed to find the free-running oscillation frequency, which is the reference for choosing next detuning frequencies.

After these preliminary steps are completed, it's time to try and guess the locking bandwidth. Let's suppose we already have an estimation of the LBW, therefore our job is eased by this projection. What we need to do is activating the injection source and - for every X_S defined injection level desired - launching a Circuit Envelope (CE) simulation [40] at the guessed frequency detuning. If an unlocking state is found, a periodic (or semi-periodic) movement of the regime envelope is observed. In this case, the corresponding $\{X_S, \Delta\omega\}$ couple can be marked as outside of the LBW, and a lower detuning must be tried next. But, if a constant regime value is reached for obtained envelope (corresponding to a sinusoidal regime, in time domain), there are two possibilities: either this is actually a locking condition, or it's necessary to repeat the simulation for a longer simulated time. In fact, it is frequent that an envelope transient seems to have reached a stable regime, but indeed it is about to show its unlocked state in next time steps, as it can be shown by increasing the simulated time. In Fig. A1.1, an example of an unlocked state (red) that exhibit

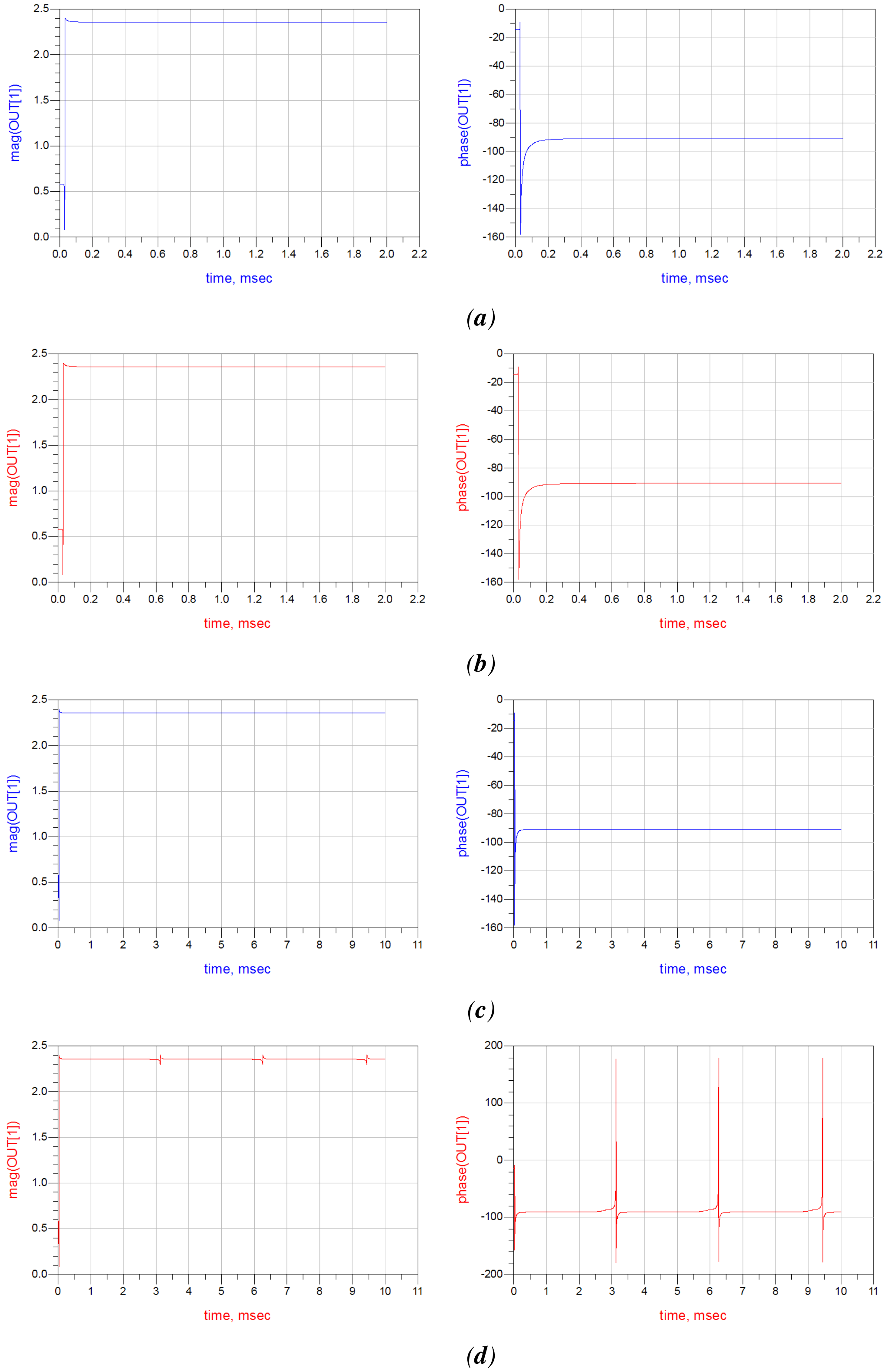

*Fig. A1.1 – Steady-state (magnitude and phase) simulations of circuit in Fig. 5.3, through ADS/CE simulation, exhibiting (**a, c**) a locked state; (**b, d**) an unlocked state. Graphics (**c, d**) show a longer time.*

the same behavior of a locked regime (blue) if observed for 2 ms instead of 10 ms, from a Circuit Envelope ADS simulation of example depicted in Fig. 5.3.

This behavior represents a problem slowing down the whole simulation process. Of course, a time-domain simulation would only produce even slower simulation steps, and is therefore not to be considered as a valid alternative.

A comparison between time durations required by ADS/CE simulation and application of presented technique (implemented in Wolfram Mathematica [54], see Chapters 3 and 5 for details) is finally reported in Tab. A1.1, related to above cited example. A huge difference clearly emerges, and an even bigger difference could be observed in more complex circuits, where the growth in single CE simulation time (e.g., 150 seconds) increases overall required EDA simulation time.

	ADS simulation	Proposed method *(implemented in Wolfram Mathematica)*
set-up time	drawing schematic, inserting parameters, HB simulation of f_{OSC}	describing circuit, inserting parameters, solving equations
	about 8 minutes	**about 14 minutes**
LBW evaluation time	Every CE simulation is approximately 35 sec (on an Intel Core i7 machine, with 8GB of RAM memory). On average 5 iterations needed every step. We consider 10 different injection values, where left and right band limits are required for each one.	Evaluation of complete (LLI/MLI/HLI) bandwidth through numerical integration.
	about 35 sec · 5 · 10 · 2 ≈ 58 min	**about 7 seconds**
TOTAL time	**about 1 hour 6 minutes**	**about 14 minutes**

Tab. A1.1 – Comparison between time durations for ADS/CE simulation vs. proposed method implemented in Wolfram Mathematica.

A2. Examination of a Possible Issue with Locus/Boundary

In some rare cases, Locus and Boundary limits, which must always be considered together as a whole, provide incorrect "holes". In fact, because of their definition [21], all stability borders are part of Locus/Boundary borders, but the converse is not always true, i.e., some Locus/Boundary limits can be not a stability limit. However, when this issue appears, it is easy to locate and adjust, since it shows itself as an "isolated" stable region, particularly unlikely to happen in reality.

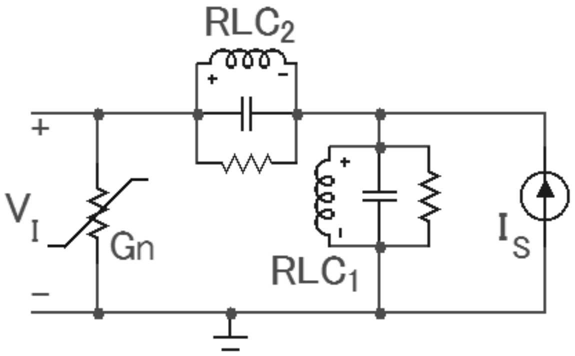

Fig. A2.1 – Double-tuned example circuit.

In Fig. A2.1 an example is provided to visualize such a behavior. It is an ideal injection-locked oscillator with a polynomial negative conductance and two simple RLC resonators. Its parameters are displayed in Tab. A2.1.

As manifest from figure A2.2a, there is a small area where Locus/Boundary conditions erroneously indicate a stable region, while (Fig. A2.2b) Routh-Hurwitz conditions display it as an unstable region. An ultimate verification test, performed through eigenvalues in a point inside that zone, confirms, as expected, that this tiny region is an unstable one.

$g_{N1} = -0.2\cdot 10^{-3}$	$g_{N2} = 0$	$g_{N3} = 0.1\cdot 10^{-3}$
$R_1 = 10\ \mathrm{k\Omega}$	$L_1 = 7.97\ \mathrm{nH}$	$C_1 = 3.19\ \mathrm{pF}$
$R_2 = 10\ \mathrm{k\Omega}$	$L_2 = 5.29\ \mathrm{nH}$	$C_2 = 4.77\ \mathrm{pF}$

Tab. A2.1 – Parameters of example circuit of Fig. A2.1.

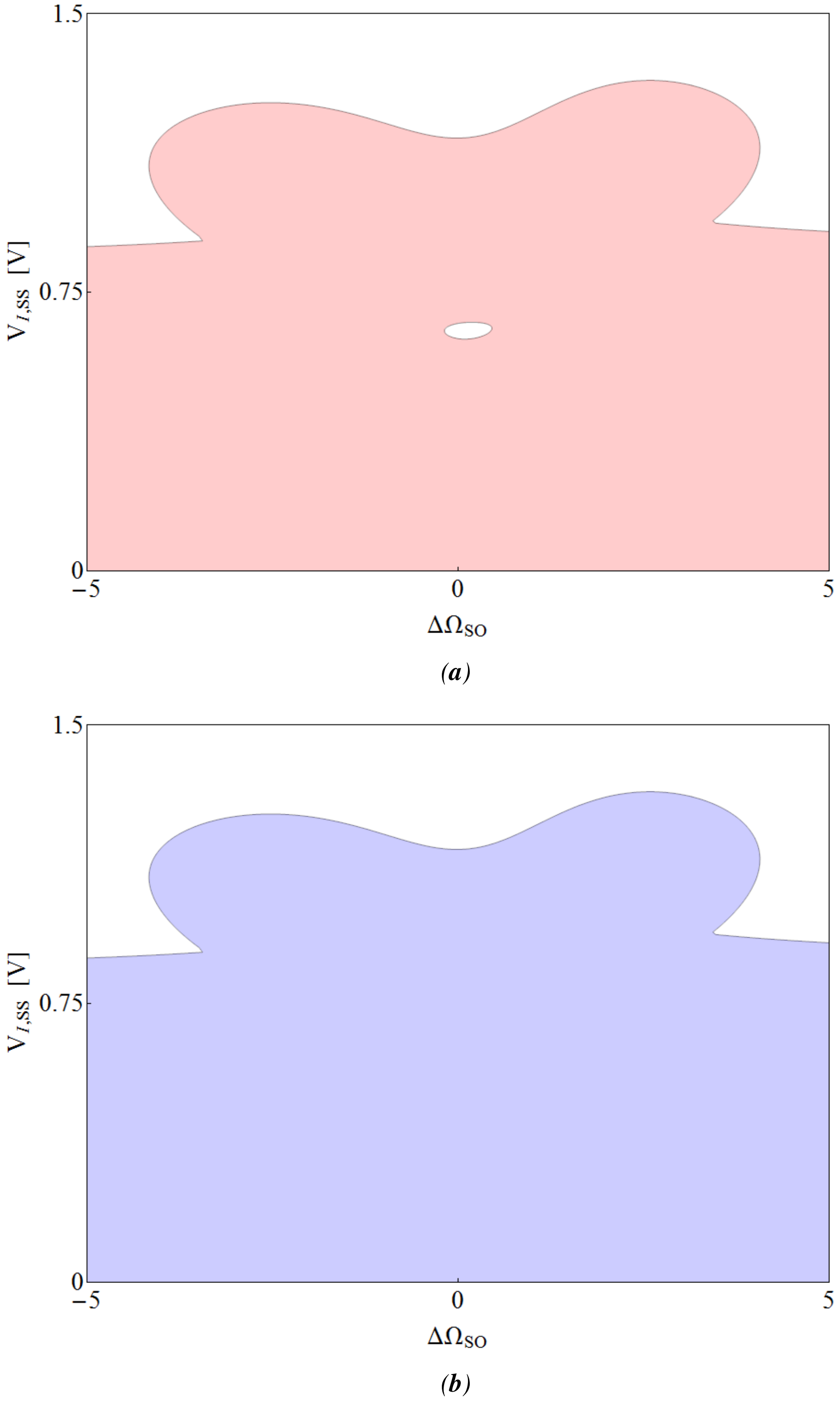

*(**a**)*

*(**b**)*

*Fig. A2.2 – Stability borders for example of Fig. A2.1, functions of the normalized detuning frequency $\Delta\Omega_{SO}$. Graphic (**a**) represents limits provided by Locus/Boundary conditions, while graphic (**b**) limits provided by Routh-Hurwitz conditions.*

A3. Extra Formulas

Among the ones excluded from the body of presented work, a few long formulas have been considered interesting enough to be included in this appendix section.

The first one is the negative conductance formula described in Sections 4.2-4.3:

(A3.1)

$$
\begin{aligned}
&\mathcal{G}_{\mathrm{N}}[\mathrm{V1}] == g_{N1} + 2\, g_{N2} \Big(-\frac{g_{N2}}{3\, g_{N3}} - \big(-4\, g_{N2}^2\, R_0^2 + 6\, g_{N3}\, R_0\, (2 + 2\, g_{N1}\, R_0 + 3\, g_{N3}\, R_0\, V_1^2)\big) \Big/ \\
&\quad \Big(3 \times 2^{2/3}\, g_{N3}\, R_0\, \Big(72\, g_{N2}\, g_{N3}\, R_0^2 + 216\, E_0\, g_{N3}^2\, R_0^2 - 16\, g_{N2}^3\, R_0^3 + 72\, g_{N1}\, g_{N2}\, g_{N3}\, R_0^3 + \\
&\qquad \surd\big(64\, R_0^4\, (27\, E_0\, g_{N3}^2 - 2\, g_{N2}^3\, R_0 + 9\, g_{N2}\, (g_{N3} + g_{N1}\, g_{N3}\, R_0))^2 + 4 \\
&\qquad\quad (-4\, g_{N2}^2\, R_0^2 + 6\, g_{N3}\, R_0\, (2 + 2\, g_{N1}\, R_0 + 3\, g_{N3}\, R_0\, V_1^2))^3\big)\Big)^{1/3}\Big) + \\
&\quad \frac{1}{6 \times 2^{1/3}\, g_{N3}\, R_0} \Big(72\, g_{N2}\, g_{N3}\, R_0^2 + 216\, E_0\, g_{N3}^2\, R_0^2 - 16\, g_{N2}^3\, R_0^3 + 72\, g_{N1}\, g_{N2}\, g_{N3}\, R_0^3 + \\
&\qquad \surd\big(64\, R_0^4\, (27\, E_0\, g_{N3}^2 - 2\, g_{N2}^3\, R_0 + 9\, g_{N2}\, (g_{N3} + g_{N1}\, g_{N3}\, R_0))^2 + \\
&\qquad\quad 4\, (-4\, g_{N2}^2\, R_0^2 + 6\, g_{N3}\, R_0\, (2 + 2\, g_{N1}\, R_0 + 3\, g_{N3}\, R_0\, V_1^2))^3\big)\Big)^{1/3}\Big) + \\
&\frac{3}{4}\, g_{N3} \Big(V_1^2 + 4 \Big(\frac{g_{N2}}{3\, g_{N3}} + \big(-4\, g_{N2}^2\, R_0^2 + 6\, g_{N3}\, R_0\, (2 + 2\, g_{N1}\, R_0 + 3\, g_{N3}\, R_0\, V_1^2)\big) \Big/ \\
&\quad \Big(3 \times 2^{2/3}\, g_{N3}\, R_0\, \Big(72\, g_{N2}\, g_{N3}\, R_0^2 + 216\, E_0\, g_{N3}^2\, R_0^2 - 16\, g_{N2}^3\, R_0^3 + 72\, g_{N1}\, g_{N2}\, g_{N3}\, R_0^3 + \\
&\qquad \surd\big(64\, R_0^4\, (27\, E_0\, g_{N3}^2 - 2\, g_{N2}^3\, R_0 + 9\, g_{N2}\, (g_{N3} + g_{N1}\, g_{N3}\, R_0))^2 + \\
&\qquad\quad 4\, (-4\, g_{N2}^2\, R_0^2 + 6\, g_{N3}\, R_0\, (2 + 2\, g_{N1}\, R_0 + 3\, g_{N3}\, R_0\, V_1^2))^3\big)\Big)^{1/3}\Big) - \\
&\quad \frac{1}{6 \times 2^{1/3}\, g_{N3}\, R_0} \Big(72\, g_{N2}\, g_{N3}\, R_0^2 + 216\, E_0\, g_{N3}^2\, R_0^2 - 16\, g_{N2}^3\, R_0^3 + 72\, g_{N1}\, g_{N2}\, g_{N3}\, R_0^3 + \\
&\qquad \surd\big(64\, R_0^4\, (27\, E_0\, g_{N3}^2 - 2\, g_{N2}^3\, R_0 + 9\, g_{N2}\, (g_{N3} + g_{N1}\, g_{N3}\, R_0))^2 + \\
&\qquad\quad 4\, (-4\, g_{N2}^2\, R_0^2 + 6\, g_{N3}\, R_0\, (2 + 2\, g_{N1}\, R_0 + 3\, g_{N3}\, R_0\, V_1^2))^3\big)\Big)^{1/3}\Big)^2\Big)
\end{aligned}
$$

Steady-state normalized equation (6.21), actualized for example of Sec. 6.5 (see step 9), descends from equation (6.40). Substituting with example quantities, and normalizing nonlinear functions, it results:

(A3.2)

$$
\begin{aligned}
& e^{j\phi_I} V_I \Big(-0.450764 - 0.0914664\,j - (0.893312 + 0.372725\,j)\,\Delta\Omega - \\
& \quad (0.723343 + 0.174627\,j)\,\Delta\Omega^2 + \big(-0.00561894 + 0.0243207\,j - \\
& \qquad (0.0372349 - 0.0149058\,j)\,\Delta\Omega - (0.00622626 + 0.0104781\,j)\,\Delta\Omega^2\big)\,V_I + \\
& \quad \big(6.25365 + 7.5992\,j - (4.28482 - 15.2217\,j)\,\Delta\Omega - (4.77154 + 0.570595\,j)\,\Delta\Omega^2\big)\,V_I^2 + \\
& \quad \big(-14.7827 + 45.937\,j - (74.1555 - 22.6545\,j)\,\Delta\Omega - (10.2889 + 21.1984\,j)\,\Delta\Omega^2\big)\,V_I^3 + \\
& \quad \big(178.163 - 626.08\,j + (989.282 - 339.508\,j)\,\Delta\Omega + (148.454 + 281.047\,j)\,\Delta\Omega^2\big)\,V_I^4 + \\
& \quad \big(-1539.36 + 3925.45\,j - (6590.2 - 1571.66\,j)\,\Delta\Omega - (781.782 + 1904.67\,j)\,\Delta\Omega^2\big)\,V_I^5 + \\
& \quad \big(5538.96 - 12\,769.7\,j + (21\,925.8 - 4411.89\,j)\,\Delta\Omega + (2355.7 + 6375.33\,j)\,\Delta\Omega^2\big)\,V_I^6 + \\
& \quad \big(-7945.72 + 17\,348.1\,j - (30\,173.2 - 5438.6\,j)\,\Delta\Omega - (3051.81 + 8803.16\,j)\,\Delta\Omega^2\big) \\
& \quad V_I^7\Big) == e^{j\phi_S}\,(0.122204 + 0.00010022\,j)\,V_S
\end{aligned}
$$

Similarly, DCE equation set (see Sec. 6.5, step 12) can be obtained from (6.25), performing some calculations and solving for $V_I''[\tau]$ and $\phi_I''[\tau]$. As already declared, it is quite long:

(A3.3a)

$$
\begin{aligned}
& V_I''[\tau] == \\
& \Big(1.2731\times10^{-10}\cos[\phi_I[\tau]]\,V_S - 3.06243\times10^{-11}\sin[\phi_I[\tau]]\,V_S + 1.63593\times10^{-10}\,V_I'[\tau] - \\
& \quad 1.82397\times10^{-11}\,V_I'[\tau]^2 + V_I[\tau]^{14}\,\big(0.269833 - 0.0928487\,\Delta\Omega - 0.182332\,\Delta\Omega^2 - \\
& \qquad 3.251\,V_I'[\tau] + (-0.0928487 - 0.364663\,\Delta\Omega)\,\phi_I'[\tau] - 0.182332\,\phi_I'[\tau]^2\big) + \\
& \quad V_I[\tau]^{12}\,\big(0.0720767 - 0.0248014\,\Delta\Omega - 0.0487037\,\Delta\Omega^2 + 8.93425\,V_I'[\tau]^2 + \\
& \qquad V_I'[\tau]\,(-2.7674 + 0.00615987\,\Delta\Omega + 0.00615987\,\phi_I'[\tau]) + \\
& \qquad (-0.0248014 - 0.0974075\,\Delta\Omega)\,\phi_I'[\tau] - 0.0487037\,\phi_I'[\tau]^2\big) + \\
& \quad V_I[\tau]^{10}\,\big(0.00337188 - 0.00116025\,\Delta\Omega - 0.00227845\,\Delta\Omega^2 + 1.77019\,V_I'[\tau]^2 + \\
& \qquad V_I'[\tau]\,(-0.251113 + 0.00193612\,\Delta\Omega + 0.00193612\,\phi_I'[\tau]) + \\
& \qquad (-0.00116025 - 0.0045569\,\Delta\Omega)\,\phi_I'[\tau] - 0.00227845\,\phi_I'[\tau]^2\big) + \\
& \quad V_I[\tau]^{7}\,\big(-2.51349\times10^{-6} - 0.0000290102\,\Delta\Omega - 9.74427\times10^{-6}\,\Delta\Omega^2 + \\
& \qquad 5.38287\times10^{-7}\cos[\phi_I[\tau]]\,V_S - 1.54862\times10^{-6}\sin[\phi_I[\tau]]\,V_S - 0.00481869 \\
& \qquad V_I'[\tau]^2 + V_I'[\tau]\,(0.0000192848 + 0.000192808\,\Delta\Omega + 0.000192808\,\phi_I'[\tau]) + \\
& \qquad (-0.0000290102 - 0.0000194885\,\Delta\Omega)\,\phi_I'[\tau] - 9.74427\times10^{-6}\,\phi_I'[\tau]^2\big) + \\
& \quad V_I[\tau]^{5}\,\big(-2.11944\times10^{-7} - 1.26948\times10^{-6}\,\Delta\Omega - 4.16515\times10^{-7}\,\Delta\Omega^2 + 1.37843\times10^{-7} \\
& \qquad \cos[\phi_I[\tau]]\,V_S - 3.35046\times10^{-7}\sin[\phi_I[\tau]]\,V_S + 0.000192168\,V_I'[\tau]^2 + \\
& \qquad V_I'[\tau]\,(-0.0000236041 + 0.0000181454\,\Delta\Omega + 0.0000181454\,\phi_I'[\tau]) + \\
& \qquad \big(-1.26948\times10^{-6} - 8.33029\times10^{-7}\,\Delta\Omega\big)\,\phi_I'[\tau] - 4.16515\times10^{-7}\,\phi_I'[\tau]^2\big) +
\end{aligned}
$$

$$
\begin{aligned}
&V_{I}[\tau]^{2}\,(5.15834\times10^{-12}+4.86672\times10^{-11}\,\Delta\Omega+1.82397\times10^{-11}\,\Delta\Omega^{2}+\\
&\quad 8.39715\times10^{-10}\cos[\phi_{I}[\tau]]\,V_{S}-9.97173\times10^{-11}\sin[\phi_{I}[\tau]]\,V_{S}-1.92976\times10^{-7}\\
&\quad V_{I}'[\tau]^{2}+V_{I}'[\tau]\,(-4.89703\times10^{-8}-2.42201\times10^{-9}\,\Delta\Omega-2.42201\times10^{-9}\,\phi_{I}'[\tau])+\\
&\quad (4.86672\times10^{-11}+3.64794\times10^{-11}\,\Delta\Omega)\,\phi_{I}'[\tau]+1.82397\times10^{-11}\,\phi_{I}'[\tau]^{2})+\\
&V_{I}[\tau]\,(4.92502\times10^{-10}+1.02417\times10^{-9}\,\Delta\Omega+7.97323\times10^{-10}\,\Delta\Omega^{2}+1.09713\times10^{-12}\\
&\quad \cos[\phi_{I}[\tau]]\,V_{S}-1.8429\times10^{-12}\sin[\phi_{I}[\tau]]\,V_{S}-3.06807\times10^{-8}\,V_{I}'[\tau]^{2}+\\
&\quad V_{I}'[\tau]\,(-5.99132\times10^{-11}+1.86961\times10^{-11}\,\Delta\Omega+1.86961\times10^{-11}\,\phi_{I}'[\tau])+\\
&\quad (1.02417\times10^{-9}+1.59465\times10^{-9}\,\Delta\Omega)\,\phi_{I}'[\tau]+7.97323\times10^{-10}\,\phi_{I}'[\tau]^{2})+\\
&V_{I}[\tau]^{3}\,(-5.25255\times10^{-9}+7.07945\times10^{-9}\,\Delta\Omega+1.0227\times10^{-8}\,\Delta\Omega^{2}+1.81357\times10^{-9}\\
&\quad \cos[\phi_{I}[\tau]]\,V_{S}-3.72873\times10^{-9}\sin[\phi_{I}[\tau]]\,V_{S}+4.30063\times10^{-6}\,V_{I}'[\tau]^{2}+\\
&\quad V_{I}'[\tau]\,(-1.91587\times10^{-7}+1.16821\times10^{-7}\,\Delta\Omega+1.16821\times10^{-7}\,\phi_{I}'[\tau])+\\
&\quad (7.07945\times10^{-9}+2.04539\times10^{-8}\,\Delta\Omega)\,\phi_{I}'[\tau]+1.0227\times10^{-8}\,\phi_{I}'[\tau]^{2})+\\
&V_{I}[\tau]^{4}\,(1.31643\times10^{-8}+9.62061\times10^{-8}\,\Delta\Omega+3.21969\times10^{-8}\,\Delta\Omega^{2}-2.61636\times10^{-8}\\
&\quad \cos[\phi_{I}[\tau]]\,V_{S}+4.94335\times10^{-8}\sin[\phi_{I}[\tau]]\,V_{S}-0.0000402599\,V_{I}'[\tau]^{2}+\\
&\quad V_{I}'[\tau]\,(2.96142\times10^{-6}-2.04307\times10^{-6}\,\Delta\Omega-2.04307\times10^{-6}\,\phi_{I}'[\tau])+\\
&\quad (9.62061\times10^{-8}+6.43938\times10^{-8}\,\Delta\Omega)\,\phi_{I}'[\tau]+3.21969\times10^{-8}\,\phi_{I}'[\tau]^{2})+\\
&V_{I}[\tau]^{6}\,(1.13029\times10^{-6}+8.58088\times10^{-6}\,\Delta\Omega+2.75151\times10^{-6}\,\Delta\Omega^{2}-4.15446\times10^{-7}\\
&\quad \cos[\phi_{I}[\tau]]\,V_{S}+1.12151\times10^{-6}\sin[\phi_{I}[\tau]]\,V_{S}-0.00020161\,V_{I}'[\tau]^{2}+\\
&\quad V_{I}'[\tau]\,(0.0000970721-0.00007977\,\Delta\Omega-0.00007977\,\phi_{I}'[\tau])+\\
&\quad (8.58088\times10^{-6}+5.50302\times10^{-6}\,\Delta\Omega)\,\phi_{I}'[\tau]+2.75151\times10^{-6}\,\phi_{I}'[\tau]^{2})+\\
&V_{I}[\tau]^{8}\,(0.0000187725+0.0000346779\,\Delta\Omega+2.86612\times10^{-6}\,\Delta\Omega^{2}+0.0575408\,V_{I}'[\tau]^{2}+\\
&\quad V_{I}'[\tau]\,(-0.00402076-0.000317127\,\Delta\Omega-0.000317127\,\phi_{I}'[\tau])+\\
&\quad (0.0000346779+5.73224\times10^{-6}\,\Delta\Omega)\,\phi_{I}'[\tau]+2.86612\times10^{-6}\,\phi_{I}'[\tau]^{2})+\\
&V_{I}[\tau]^{9}\,(-0.00035871+0.000123431\,\Delta\Omega+0.000242388\,\Delta\Omega^{2}-0.395646\,V_{I}'[\tau]^{2}+\\
&\quad V_{I}'[\tau]\,(0.0408068+0.00026294\,\Delta\Omega+0.00026294\,\phi_{I}'[\tau])+\\
&\quad (0.000123431+0.000484776\,\Delta\Omega)\,\phi_{I}'[\tau]+0.000242388\,\phi_{I}'[\tau]^{2})+\\
&V_{I}[\tau]^{11}\,(-0.0190891+0.00656851\,\Delta\Omega+0.0128989\,\Delta\Omega^{2}-5.16552\,V_{I}'[\tau]^{2}+\\
&\quad V_{I}'[\tau]\,(1.02783-0.00531275\,\Delta\Omega-0.00531275\,\phi_{I}'[\tau])+\\
&\quad (0.00656851+0.0257978\,\Delta\Omega)\,\phi_{I}'[\tau]+0.0128989\,\phi_{I}'[\tau]^{2})+\\
&V_{I}[\tau]^{13}\,(-0.180067+0.0619606\,\Delta\Omega+0.121675\,\Delta\Omega^{2}-7\,V_{I}'[\tau]^{2}+\\
&\quad V_{I}'[\tau]\,(4.44477-0.0036901\,\Delta\Omega-0.0036901\,\phi_{I}'[\tau])+\\
&\quad (0.0619606+0.24335\,\Delta\Omega)\,\phi_{I}'[\tau]+0.121675\,\phi_{I}'[\tau]^{2})+\\
&V_{I}[\tau]^{15}\,(-0.184988+0.0636537\,\Delta\Omega+0.125\,\Delta\Omega^{2}+\\
&\quad (0.0636537+0.25\,\Delta\Omega)\,\phi_{I}'[\tau]+0.125\,\phi_{I}'[\tau]^{2}))\,/\\
&(7.97323\times10^{-10}+2.73595\times10^{-11}\,V_{I}[\tau]+2.04539\times10^{-8}\,V_{I}[\tau]^{2}+\\
&\quad 8.04922\times10^{-8}\,V_{I}[\tau]^{3}-1.24954\times10^{-6}\,V_{I}[\tau]^{4}+\\
&\quad 9.63028\times10^{-6}\,V_{I}[\tau]^{5}-0.0000389771\,V_{I}[\tau]^{6}+\\
&\quad 0.0000128975\,V_{I}[\tau]^{7}+0.00121194\,V_{I}[\tau]^{8}-\\
&\quad 0.0125315\,V_{I}[\tau]^{9}+0.0773935\,V_{I}[\tau]^{10}-\\
&\quad 0.316574\,V_{I}[\tau]^{11}+0.851726\,V_{I}[\tau]^{12}-\\
&\quad 1.36749\,V_{I}[\tau]^{13}+V_{I}[\tau]^{14})
\end{aligned}
$$

(A3.3b)

$$
\begin{aligned}
&\phi_I''[\tau] == \Big(-6.07491\times10^{-16}\cos[\phi_I[\tau]]\,V_S - 2.52543\times10^{-15}\sin[\phi_I[\tau]]\,V_S - \\
&\quad 3.70873\times10^{-16}\,V_I'[\tau]^2 + V_I[\tau]^{22}\,(-1.41564 - 3.251\,\Delta\Omega - 3.251\,\phi_I'[\tau]) + \\
&\quad V_I'[\tau]\,\big(-2.03164\times10^{-14} - 3.16329\times10^{-14}\,\Delta\Omega - 3.16329\times10^{-14}\,\phi_I'[\tau]\big) + \\
&\quad V_I[\tau]\,\Big(-3.586\times10^{-16} + 3.24518\times10^{-15}\,\Delta\Omega - 1.09566\times10^{-16}\cos[\phi_I[\tau]]\,V_S - \\
&\qquad 1.95059\times10^{-16}\sin[\phi_I[\tau]]\,V_S + 7.20456\times10^{-14}\,V_I'[\tau]^2 + \\
&\qquad V_I'[\tau]\,\big(-3.14985\times10^{-15} - 3.34533\times10^{-15}\,\Delta\Omega - 3.34533\times10^{-15}\,\phi_I'[\tau]\big) + \\
&\qquad 3.24518\times10^{-15}\,\phi_I'[\tau]\Big) + \\
&\quad V_I[\tau]^{15}\,\big(0.00975447 + 0.0218922\,\Delta\Omega - 0.000202577\,\Delta\Omega^2 + 0.0501418\,V_I'[\tau]^2 + \\
&\qquad V_I'[\tau]\,(-0.118194 - 0.464206\,\Delta\Omega - 0.464206\,\phi_I'[\tau]) + \\
&\qquad (0.0218922 - 0.000405154\,\Delta\Omega)\,\phi_I'[\tau] - 0.000202577\,\phi_I'[\tau]^2\big) + \\
&\quad V_I[\tau]^{13}\,\big(0.0000397895 + 0.0000757756\,\Delta\Omega - 0.0000643155\,\Delta\Omega^2 + \\
&\qquad 0.0000168228\cos[\phi_I[\tau]]\,V_S + 6.02678\times10^{-6}\sin[\phi_I[\tau]]\,V_S - 0.00273062 \\
&\qquad V_I'[\tau]^2 + V_I'[\tau]\,(-0.00179936 - 0.00848402\,\Delta\Omega - 0.00848402\,\phi_I'[\tau]) + \\
&\qquad (0.0000757756 - 0.000128631\,\Delta\Omega)\,\phi_I'[\tau] - 0.0000643155\,\phi_I'[\tau]^2\big) + \\
&\quad V_I[\tau]^{11}\,\big(-7.2589\times10^{-6} - 0.0000129128\,\Delta\Omega - 4.27579\times10^{-6}\,\Delta\Omega^2 + \\
&\qquad 3.79712\times10^{-6}\cos[\phi_I[\tau]]\,V_S + 1.49647\times10^{-6}\sin[\phi_I[\tau]]\,V_S - 0.000642901 \\
&\qquad V_I'[\tau]^2 + V_I'[\tau]\,(0.000111119 + 0.00011676\,\Delta\Omega + 0.00011676\,\phi_I'[\tau]) + \\
&\qquad \big(-0.0000129128 - 8.55158\times10^{-6}\,\Delta\Omega\big)\,\phi_I'[\tau] - 4.27579\times10^{-6}\,\phi_I'[\tau]^2\big) + \\
&\quad V_I[\tau]^{9}\,\big(-1.25958\times10^{-7} - 1.86706\times10^{-7}\,\Delta\Omega - 6.2369\times10^{-8}\,\Delta\Omega^2 + 1.46261\times10^{-7} \\
&\qquad \cos[\phi_I[\tau]]\,V_S + 6.41666\times10^{-8}\sin[\phi_I[\tau]]\,V_S - 0.0000289389\,V_I'[\tau]^2 + \\
&\qquad V_I'[\tau]\,\big(4.44735\times10^{-6} + 5.16245\times10^{-6}\,\Delta\Omega + 5.16245\times10^{-6}\,\phi_I'[\tau]\big) + \\
&\qquad \big(-1.86706\times10^{-7} - 1.24738\times10^{-7}\,\Delta\Omega\big)\,\phi_I'[\tau] - 6.2369\times10^{-8}\,\phi_I'[\tau]^2\big) + \\
&\quad V_I[\tau]^{6}\,\big(-2.56941\times10^{-10} - 3.42817\times10^{-10}\,\Delta\Omega - 1.7933\times10^{-10}\,\Delta\Omega^2 + \\
&\qquad 1.64374\times10^{-10}\cos[\phi_I[\tau]]\,V_S + 2.19864\times10^{-10}\sin[\phi_I[\tau]]\,V_S - 5.44052\times10^{-9} \\
&\qquad V_I'[\tau]^2 + V_I'[\tau]\,\big(4.97103\times10^{-9} + 5.8881\times10^{-9}\,\Delta\Omega + 5.8881\times10^{-9}\,\phi_I'[\tau]\big) + \\
&\qquad \big(-3.42817\times10^{-10} - 3.58659\times10^{-10}\,\Delta\Omega\big)\,\phi_I'[\tau] - 1.7933\times10^{-10}\,\phi_I'[\tau]^2\big) + \\
&\quad V_I[\tau]^{4}\,\big(-2.06896\times10^{-12} - 2.20196\times10^{-12}\,\Delta\Omega - 1.15785\times10^{-12}\,\Delta\Omega^2 + \\
&\qquad 5.83473\times10^{-12}\cos[\phi_I[\tau]]\,V_S + 6.48227\times10^{-12}\sin[\phi_I[\tau]]\,V_S - 1.09582\times10^{-9} \\
&\qquad V_I'[\tau]^2 + V_I'[\tau]\,\big(1.55173\times10^{-10} + 1.23699\times10^{-10}\,\Delta\Omega + 1.23699\times10^{-10}\,\phi_I'[\tau]\big) + \\
&\qquad \big(-2.20196\times10^{-12} - 2.3157\times10^{-12}\,\Delta\Omega\big)\,\phi_I'[\tau] - 1.15785\times10^{-12}\,\phi_I'[\tau]^2\big) + \\
&\quad V_I[\tau]^{2}\,\big(-7.89337\times10^{-16} - 7.01142\times10^{-16}\,\Delta\Omega - 1.85437\times10^{-16}\,\Delta\Omega^2 - 7.92361\times10^{-15} \\
&\qquad \cos[\phi_I[\tau]]\,V_S - 5.82265\times10^{-14}\sin[\phi_I[\tau]]\,V_S - 4.62897\times10^{-12}\,V_I'[\tau]^2 + \\
&\qquad V_I'[\tau]\,\big(-4.87805\times10^{-13} - 1.32068\times10^{-12}\,\Delta\Omega - 1.32068\times10^{-12}\,\phi_I'[\tau]\big) + \\
&\qquad \big(-7.01142\times10^{-16} - 3.70873\times10^{-16}\,\Delta\Omega\big)\,\phi_I'[\tau] - 1.85437\times10^{-16}\,\phi_I'[\tau]^2\big) + \\
&\quad V_I[\tau]^{3}\,\big(-1.11689\times10^{-13} - 2.16633\times10^{-13}\,\Delta\Omega + 2.40115\times10^{-14}\,\Delta\Omega^2 - \\
&\qquad 3.70206\times10^{-13}\cos[\phi_I[\tau]]\,V_S - 4.5361\times10^{-13}\sin[\phi_I[\tau]]\,V_S + 1.01229\times10^{-10} \\
&\qquad V_I'[\tau]^2 + V_I'[\tau]\,\big(-1.01336\times10^{-11} - 9.0354\times10^{-12}\,\Delta\Omega - 9.0354\times10^{-12}\,\phi_I'[\tau]\big) + \\
&\qquad \big(-2.16633\times10^{-13} + 4.8023\times10^{-14}\,\Delta\Omega\big)\,\phi_I'[\tau] + 2.40115\times10^{-14}\,\phi_I'[\tau]^2\big) + \\
&\quad V_I[\tau]^{5}\,\big(2.71116\times10^{-11} + 2.70813\times10^{-11}\,\Delta\Omega + 2.02505\times10^{-11}\,\Delta\Omega^2 - \\
&\qquad 4.77789\times10^{-11}\cos[\phi_I[\tau]]\,V_S - 5.02619\times10^{-11}\sin[\phi_I[\tau]]\,V_S + 5.69339\times10^{-9} \\
&\qquad V_I'[\tau]^2 + V_I'[\tau]\,\big(-1.31864\times10^{-9} - 1.1977\times10^{-9}\,\Delta\Omega - 1.1977\times10^{-9}\,\phi_I'[\tau]\big) + \\
&\qquad \big(2.70813\times10^{-11} + 4.05011\times10^{-11}\,\Delta\Omega\big)\,\phi_I'[\tau] + 2.02505\times10^{-11}\,\phi_I'[\tau]^2\big) +
\end{aligned}
$$

$$
\begin{aligned}
& V_I[\tau]^7\,\big(9.12759\times10^{-10}+1.63309\times10^{-9}\,\Delta\Omega+6.65269\times10^{-10}\,\Delta\Omega^2+{}\\
&\quad 6.11965\times10^{-10}\cos[\phi_I[\tau]]\,V_S-2.59724\times10^{-10}\sin[\phi_I[\tau]]\,V_S-2.65137\times10^{-7}\\
&\quad V_I'[\tau]^2+V_I'[\tau]\,\big(1.44603\times10^{-8}+4.62116\times10^{-9}\,\Delta\Omega+4.62116\times10^{-9}\,\phi_I'[\tau]\big)+{}\\
&\quad \big(1.63309\times10^{-9}+1.33054\times10^{-9}\,\Delta\Omega\big)\,\phi_I'[\tau]+6.65269\times10^{-10}\,\phi_I'[\tau]^2\big)+{}\\
& V_I[\tau]^8\,\big(5.48739\times10^{-9}+4.99928\times10^{-9}\,\Delta\Omega+2.14053\times10^{-9}\,\Delta\Omega^2-1.52518\times10^{-8}\\
&\quad \cos[\phi_I[\tau]]\,V_S-5.73203\times10^{-9}\sin[\phi_I[\tau]]\,V_S+3.66673\times10^{-6}\,V_I'[\tau]^2+{}\\
&\quad V_I'[\tau]\,\big(-4.41853\times10^{-7}-4.51035\times10^{-7}\,\Delta\Omega-4.51035\times10^{-7}\,\phi_I'[\tau]\big)+{}\\
&\quad \big(4.99928\times10^{-9}+4.28106\times10^{-9}\,\Delta\Omega\big)\,\phi_I'[\tau]+2.14053\times10^{-9}\,\phi_I'[\tau]^2\big)+{}\\
& V_I[\tau]^{10}\,\big(1.20897\times10^{-6}+2.00168\times10^{-6}\,\Delta\Omega+6.41563\times10^{-7}\,\Delta\Omega^2-9.09332\times10^{-7}\\
&\quad \cos[\phi_I[\tau]]\,V_S-3.84151\times10^{-7}\sin[\phi_I[\tau]]\,V_S+0.000158335\,V_I'[\tau]^2+{}\\
&\quad V_I'[\tau]\,(-0.0000281509-0.0000340439\,\Delta\Omega-0.0000340439\,\phi_I'[\tau])+{}\\
&\quad \big(2.00168\times10^{-6}+1.28313\times10^{-6}\,\Delta\Omega\big)\,\phi_I'[\tau]+6.41563\times10^{-7}\,\phi_I'[\tau]^2\big)+{}\\
& V_I[\tau]^{12}\,\big(0.0000235615+0.0000452707\,\Delta\Omega+0.0000197243\,\Delta\Omega^2-{}\\
&\quad 0.0000103762\cos[\phi_I[\tau]]\,V_S-3.86486\times10^{-6}\sin[\phi_I[\tau]]\,V_S+0.00185772\\
&\quad V_I'[\tau]^2+V_I'[\tau]\,(-0.0001417+0.000317291\,\Delta\Omega+0.000317291\,\phi_I'[\tau])+{}\\
&\quad (0.0000452707+0.0000394486\,\Delta\Omega)\,\phi_I'[\tau]+0.0000197243\,\phi_I'[\tau]^2\big)+{}\\
& V_I[\tau]^{14}\,\big(-0.00117533-0.00251149\,\Delta\Omega+0.00014608\,\Delta\Omega^2-{}\\
&\quad 0.000012389\cos[\phi_I[\tau]]\,V_S-4.3063\times10^{-6}\sin[\phi_I[\tau]]\,V_S-{}\\
&\quad 0.00602194\,V_I'[\tau]^2+V_I'[\tau]\,(0.0191234+0.0761508\,\Delta\Omega+0.0761508\,\phi_I'[\tau])+{}\\
&\quad (-0.00251149+0.00029216\,\Delta\Omega)\,\phi_I'[\tau]+0.00014608\,\phi_I'[\tau]^2\big)+{}\\
& V_I[\tau]^{17}\,\big(0.235267+0.545163\,\Delta\Omega+0.00124712\,\Delta\Omega^2+0.237107\,V_I'[\tau]^2+{}\\
&\quad V_I'[\tau]\,(-1.80683-7.09633\,\Delta\Omega-7.09633\,\phi_I'[\tau])+{}\\
&\quad (0.545163+0.00249424\,\Delta\Omega)\,\phi_I'[\tau]+0.00124712\,\phi_I'[\tau]^2\big)+V_I[\tau]^{21}\\
&\ \ \big(2.95836+6.80106\,\Delta\Omega+0.00184505\,\Delta\Omega^2+V_I'[\tau]\,(-4.07384-16\,\Delta\Omega-16\,\phi_I'[\tau])+{}\\
&\quad (6.80106+0.0036901\,\Delta\Omega)\,\phi_I'[\tau]+0.00184505\,\phi_I'[\tau]^2\big)+{}\\
& V_I[\tau]^{19}\,\big(1.77758+4.10286\,\Delta\Omega+0.00528609\,\Delta\Omega^2+0.103323\,V_I'[\tau]^2+{}\\
&\quad V_I'[\tau]\,(-7.65495-30.0648\,\Delta\Omega-30.0648\,\phi_I'[\tau])+{}\\
&\quad (4.10286+0.0105722\,\Delta\Omega)\,\phi_I'[\tau]+0.00528609\,\phi_I'[\tau]^2\big)+{}\\
& V_I[\tau]^{16}\,\big(-0.0552847-0.127148\,\Delta\Omega-0.0000477802\,\Delta\Omega^2-0.146708\,V_I'[\tau]^2+{}\\
&\quad (-0.127148-0.0000955603\,\Delta\Omega)\,\phi_I'[\tau]-0.0000477802\,\phi_I'[\tau]^2+{}\\
&\quad V_I'[\tau]\,(0.534369+2.09874\,\Delta\Omega+2.09874\,\phi_I'[\tau])\big)+{}\\
& V_I[\tau]^{18}\,\big(-0.754855-1.74765\,\Delta\Omega-0.00361712\,\Delta\Omega^2-0.222664\,V_I'[\tau]^2+{}\\
&\quad (-1.74765-0.00723424\,\Delta\Omega)\,\phi_I'[\tau]-0.00361712\,\phi_I'[\tau]^2+{}\\
&\quad V_I'[\tau]\,(4.46652+17.5423\,\Delta\Omega+17.5423\,\phi_I'[\tau])\big)+{}\\
& V_I[\tau]^{20}\,\big(-2.90747-6.69423\,\Delta\Omega-0.00441614\,\Delta\Omega^2+7.10543\times10^{-15}\,V_I'[\tau]^2+{}\\
&\quad (-6.69423-0.00883227\,\Delta\Omega)\,\phi_I'[\tau]-0.00441614\,\phi_I'[\tau]^2+{}\\
&\quad V_I'[\tau]\,(8.14984+32.0085\,\Delta\Omega+32.0085\,\phi_I'[\tau])\big)\big)\Big/\\
\big(& V_I[\tau]\,\big(0.0000198369+1.19027\times10^{-6}\,V_I[\tau]+0.0000648171\,V_I[\tau]^2+{}\\
&\quad 0.00240804\,V_I[\tau]^3-0.0319257\,V_I[\tau]^4+{}\\
&\quad 0.216362\,V_I[\tau]^5-0.72421\,V_I[\tau]^6+V_I[\tau]^7\big)\\
&\ \big(7.97323\times10^{-10}+2.73595\times10^{-11}\,V_I[\tau]+2.04539\times10^{-8}\,V_I[\tau]^2+{}\\
&\quad 8.04922\times10^{-8}\,V_I[\tau]^3-1.24954\times10^{-6}\,V_I[\tau]^4+9.63028\times10^{-6}\,V_I[\tau]^5-{}\\
&\quad 0.0000389771\,V_I[\tau]^6+0.0000128975\,V_I[\tau]^7+0.00121194\,V_I[\tau]^8-{}\\
&\quad 0.0125315\,V_I[\tau]^9+0.0773935\,V_I[\tau]^{10}-0.316574\,V_I[\tau]^{11}+{}\\
&\quad 0.851726\,V_I[\tau]^{12}-1.36749\,V_I[\tau]^{13}+V_I[\tau]^{14}\big)\big)
\end{aligned}
$$

References

[1] A. Suarez, *Analysis and Design of Autonomous Microwave Circuits.*: Wiley-IEEE Press, 2009.

[2] K. Kurokawa, "Injection locking of microwave solid-state oscillators," *Proc. of the IEEE*, vol. 61, pp. 1386-1410, Oct. 1973.

[3] Y. Tajima, "GaAs FET Applications for Injection-Locked Oscillators and Self-Oscillating Mixers," *IEEE Transactions on Microwave Theory and Techniques*, vol. 27, no. 7, pp. 629-632, July 1979.

[4] T.H. Lee, H. Samavati, and H.R. Rategh, "5-GHz CMOS wireless LANs," *IEEE Transactions on Microwave Theory and Techniques*, vol. 50, no. 1, pp. 268-280, Jan. 2002.

[5] Hyunwoo Cho, Joonsung Bae, and Hoi-Jun Yoo, "A 39 μW body channel communication wake-up receiver with injection-locking ring-oscillator for wireless body area network," in *IEEE International Symposium on Circuits and Systems (ISCAS)*, Seoul, pp. 2641-2644, May 2012.

[6] L. Zhang, B. Ciftcioglu, M. Huang, and H. Wu, "Injection-Locked Clocking: A New GHz Clock Distribution Scheme," in *IEEE Custom Integrated Circuits Conference (CICC)*, San Jose, CA, pp. 785-788, Sep. 2006.

[7] Fu-Kang Wang et al., "A Novel Vital-Sign Sensor Based on a Self-Injection-Locked Oscillator," *IEEE Transactions on Microwave Theory and Techniques*, vol. 58, no. 12, pp. 4112-4120, Dec. 2010.

[8] L. Liu, T. Sakurai, and M. Takamiya, "315MHz energy-efficient injection-locked OOK transmitter and 8.4μW power-gated receiver front-end for wireless ad hoc network in 40nm CMOS," in *Symposium on VLSI Circuits (VLSIC)*, Honolulu, HI, pp. 164-165, June 2011.

[9] B. Mesgarzadeh and A. Alvandpour, "First-Harmonic Injection-Locked Ring Oscillators," in *IEEE Custom Integrated Circuits Conference (CICC)*, San Jose, CA, pp. 733-736, Sep. 2006.

[10] K. Takano, M. Motoyoshi, and M. Fujishima, "4.8GHz CMOS frequency multiplier with subharmonic pulse-injection locking," in *IEEE Asian Solid-State Circuits Conference (ASSCC)*, Jeju, pp. 336-339, Nov. 2007.

[11] P. Maffezzoni, D. D'Amore, S. Daneshgar, and M. P. Kennedy, "Analysis and Design of Injection-Locked Frequency Dividers by Means of a Phase-Domain Macromodel," *IEEE Transactions on Circuits and Systems I*, vol. 57, no. 11, pp. 2956-2966, Nov. 2010.

[12] M. P. Kennedy, Hongjia Mo, and Xi Dong, "Experimental characterization of Arnold tongues in injection-locked CMOS LC frequency dividers with tail and direct injection," in *20th European Conference on Circuit Theory and Design (ECCTD)*, Linkoping, Sweden, pp. 484-487, Aug. 2011.

[13] S. L. Jang, R. K. Yang, C. W. Chang, and M. H. Juang, "Multi-Modulus LC Injection-Locked Frequency Dividers Using Single-Ended Injection," *IEEE Microwave and Wireless Components Letters*, vol. 19, no. 5, pp. 311-313, May 2009.

[14] Z. D. Huang, C. Y. Wu, and B. C. Huang, "Design of 24-GHz 0.8-V 1.51-mW Coupling Current-Mode Injection-Locked Frequency Divider With Wide Locking Range," *IEEE Transactions on Microwave Theory and Techniques*, vol. 57, no. 8, pp. 1948-1958, Aug. 2009.

[15] S. Verma, H. R. Rategh, and T. H. Lee, "A unified model for injection-locked frequency dividers," *IEEE Journal of Solid-State Circuits*, vol. 38, no. 6, pp. 1015-1027, June 2003.

[16] M. Hossain and A. C. Carusone, "CMOS Oscillators for Clock Distribution and Injection-Locked Deskew," *IEEE Journal of Solid-State Circuits*, vol. 44, no. 8, pp. 2138-2153, Aug. 2009.

[17] Shih-Chieh Yen and Tah-Hsiung Chu, "A retro-directive antenna array with phase conjugation circuit using subharmonically injection-locked self-oscillating mixers," *IEEE Transactions on Antennas and Propagation*, vol. 52, no. 1, pp. 154-164, Jan. 2004.

[18] S.V. Hoeye, C. Vazquez, M. Fernandez, L.F. Herran, and F. Las-Heras, "Receiving Phased Antenna Array Based on Injection-Locked Harmonic Self-Oscillating Mixers," *IEEE Transactions on Antennas and Propagation*, vol. 57,

no. 3, pp. 645-651, Mar. 2009.

[19] A. Daryoush, M Francisco, R. Saedi, D. Polifko, and R. Kunath, "Phase control of optically injection locked oscillators for phased arrays," in *IEEE MTT-S International Microwave Symposium Digest*, Dallas (TX, USA), pp. 1247-1250 (vol. 3), May 1990.

[20] T. Berceli, W. D. Jemison, P. R. Herczfeld, A. S. Daryoush, and A. Paolella, "A double-stage injection-locked oscillator for optically fed phased array antennas," *IEEE Transactions on Microwave Theory and Techniques*, vol. 39, no. 2, pp. 201-208, Feb. 1991.

[21] E. F. Calandra and A. Sommariva, "Necessary and sufficient conditions for frequency entrainment of quasi-sinusoidal injection-synchronized oscillators," *IEEE Trans. Cir. Sys.,* vol. 33, no. 1, pp. 83-93, Jan. 1986.

[22] Agilent EEsof EDA: Advanced Design System 2009 (Update 1), User's Guide.

[23] Y. Tajima and K. Mishima, "Transmission-type injection locking of GaAs schottky-barrier FET oscillators," *IEEE Trans. Microwave Theory Tech.*, vol. 27, pp. 386-391, May 1979.

[24] E. F. Calandra and A. Sommariva, "Approach to the analysis of nonlinear feedback oscillators under large-signal injection," *IEE Proc.*, vol. 133, pt. G, no. 5, pp. 233-241, Oct. 1986.

[25] X. Lai and J. Roychowdhury, "Capturing oscillator injection locking via nonlinear phase-domain macromodels," *IEEE Trans. on Microwave Theory Tech.*, vol. 52, pp. 2251-2261, Sep. 2004.

[26] R. Adler, "A study of locking phenomena in oscillators," *Proceedings of the IRE*, vol. 34, no. 6, pp. 351-357, June 1946.

[27] P. Bhansali and J. Roychowdhury, "Gen-Adler: the Generalized Adler's equation for injection locking analysis in oscillators," in *IEEE 2009 Asia and South Pacific Design Automation Conf.*, Yokohama, pp. 522-527, Jan. 2009.

[28] T. Ohira, "Extended Adler's injection locked Q factor formula for general one- and two-port active device oscillators," *IEICE Electronics Express*, vol. 7, no. 19, pp. 1486-1492, Oct. 2010.

[29] A. Grebennikov, *RF and Microwave Transistor Oscillator Design.*: Wiley,

2007.

[30] A. Gelb and W. E. Vander Velde, *Multiple-input describing functions and nonlinear system design*. New York, USA: McGraw-Hill, 1968.

[31] E. Calandra, D. Lupo, and L. Puccio, "A DRO-based X-band Injection-Locked Amplifier Without Input Non-reciprocal Elements," in *Proceedings of European Conference on Circuit Theory and Design (ECCTD)*, Antalya, pp. 367-370, Aug. 2009.

[32] V.I. Arnold, *Geometrical Methods in the Theory of Ordinary Differential Equations.*: Springer-Verlag, 1983.

[33] Hyoung-Seok Oh, Taeksang Song, Euisik Yoon, and Choong-Ki Kim, "A power-efficient injection-locked class-E power amplifier for wireless sensor network," *IEEE Microwave and Wireless Components Letters*, vol. 16, no. 4, pp. 173-175, Apr. 2006.

[34] E. F. Calandra, M. Caruso, and D. Lupo, "Influence of active device nonlinearities on the determination of Adler's injection-locking Q-factor," in *20th European Conference on Circuit Theory and Design (ECCTD)*, Linkoping (Sweden), pp. 110-113, Aug. 2011.

[35] E. F. Calandra, M. Caruso, and D. Lupo, "Accelerated Analysis of Low-Level Injection Operation for Transistor-Based Oscillating Amplifiers," in *Recent Researches in Circuits, Systems and Signal Processing*, Corfu, Greece, pp. 176-181, July 2011.

[36] A. P. S. Khanna and Ed Gane, "A fast-locking X-band transmission injection-locked DRO," in *IEEE MTT-S International Microwave Symposium Digest*, New York, NY, USA, pp 601-604, May 1988.

[37] K. Kurokawa, "Some basic characteristics of broadband negative resistance oscillator circuits," *Bell System Technical Journal*, pp. 1937-1955, 1969.

[38] X. Wang and N. J. Gomes, "Locking bandwidth equations for electrically and optically injection-locked oscillators," *IEE Proceedings Optoelectronics*, vol. 151, no. 6, pp. 476-481, Dec. 2004.

[39] B. Razavi, "A Study of Injection Locking and Pulling in Oscillators," *IEEE Journal of Solid-State Circuits*, vol. 39, no. 9, pp. pp. 1415-1424, Sep. 2004.

[40] D. Morris. (2005, Oct.-Nov.) Enhancements to RFIC Simulation Improve Circuit Verification, in Chip Design Magazine. [Online]. http://chipdesignmag.com/display.php?articleId=189&issueId=13

[41] Agilent Technologies, Circuit Envelope Simulation, 2004.

[42] I. Petitbon, R. Gallion, G. Debarge, and C. Chabran, "Locking bandwidth and relaxation oscillations of an injection-locked semiconductor laser," *IEEE J. Quantum Electron.*, vol. 24, no. 2, pp. 148-154, Feb. 1988.

[43] S. Kobayashi and T. Kimura, "Injection Locking Characteristics of an AlGaAs Semiconductor Laser," *IEEE Journal of Quantum Electronics*, vol. 16, no. 9, pp. 915-917, Sep. 1980.

[44] H. Li and K. N. B. Abraham, "Analysis of the noise spectra of a laser diode with optical feedback from a high-finesse resonator," *IEEE Journal of Quantum Electronics*, vol. 25, no. 8, pp. 1782–1793, Aug. 1989.

[45] M. C. Espana-Boquera and A. Puerta-Notario, "Noise effects in injection locked laser simulation: Phase jumps and associated spectral components," *Electron. Lett.*, vol. 32, no. 9, pp. 818–819, Apr. 1996.

[46] J. C. Cotteverte, G. Ropars, A. Le Floch, and F. Bretenaker, "Polarization Dragging in Injected Lasers," *IEEE Journal of Quantum Electronics*, vol. 30, no. 11, pp. 2516-2525, Nov 1994.

[47] A. E. Siegman, *Lasers*. Mill Valley, CA, USA: University Science Books, 1986.

[48] A. Pikovsky and M. Rosenblum, "Synchronization: A general phenomenon in an oscillatory world," *Nova Acta Leopoldina*, vol. 88, no. 332, pp. 255-268, 2003.

[49] R. R. Ward, *The Living Clocks*. New York, USA: Collins, 1971.

[50] L. J. Paciorek, "Injection locking of oscillators," *Proceedings of the IEEE*, vol. 53, no. 11, pp. 1723-1727, Nov. 1965.

[51] A. Mirzaei, M. E. Heidari, and A. A. Abidi, "Analysis of Oscillators Locked by Large Injection Signals: Generalized Adler's Equation and Geometrical Interpretation," in *IEEE 2006 Custom Intergrated Circuits Conference (CICC)*, San Jose, CA, pp. 737-740, 2006.

[52] D. Price and H. M. Sze, "Phase-Stability Analysis of the Magnetron-Driven Vircator Experiment," *IEEE Transactions on Plasma Science*, vol. 18, no. 3, pp. 580-585, June 1990.

[53] N. R. Lanka, S. A. Patnaik, and R. A. Harjani, "Frequency-Hopped Quadrature Frequency Synthesizer in 0.13-um Technology," *IEEE Journal of Solid-State Circuits*, vol. 46, no. 9, pp. 2021-2032, Sep. 2011.

[54] Wolfram Research, *Wolfram Mathematica*. Version 9.0, 2013.

[55] E. X. DeJesus and C. Kaufman, "Routh-Hurwitz criterion in the examination of eigenvalues of a system of nonlinear ordinary differential equations," *Physical Review A*, vol. 35, no. 12, pp. 5288-5290, July 1987.

[56] A. V. Grebennikov, "Stability of Negative Resistance Oscillator Circuits," *International Journal of Electrical Engineering Education*, vol. 36, no. 3, pp. 242-254, July 1999.

[57] Y. Hong, P. S. Spencer, and K. A. Shore, "Power and frequency dependence of hysteresis in optically bistable injection locked VCSELs," *Electronics Letters*, vol. 37, no. 9, pp. 569-570, Apr. 2001.

[58] S. Osborne, A. Amann, and S. O'Brien, "All-optical memory based on the injection locking bistability of a two-colour laser diode," in *European Conference on Lasers and Electro-Optics (CLEO Europe) and European Quantum Electronics Conference (EQEC)*, Munich, Germany, p.1, 2009.

[59] S. Daneshgar, O. De Feo, and M. P. Kennedy, "Observations Concerning the Locking Range in a Complementary Differential LC Injection-Locked Frequency Divider - Part I: Qualitative Analysis," *IEEE Transactions on Circuits and Systems I: Regular Papers*, vol. 57, no. 1, pp. 179-188, Jan. 2010.

[60] M. D’Aquino, C. Serpico, R. Bonin, G. Bertotti, and I. D. Mayergoyz, "Analysis of synchronized regimes for injection-locked spin-transfer nano-oscillators," *Physica B: Physics of Condensed Matter*, vol. 407, no. 9, pp. 1357-1364, May 2012.

[61] E. Efstathiou, "An algorithm for numerical analysis of oscillator including the shifting bias of active element," in *Second International Conference on Frequency Control and Synthesis*, Leicester, UK, pp. 45-48, Apr. 1989.

[62] D. O. Pederson and K. Mayaram, *Analog Integrated Circuits for*

Communication, Chapter 11.: Springer, 2008.

[63] E. F. Calandra and M. Caruso, "Analysis of Bias-Shift Effects in Free-Running and Injection-Locked Negative Resistance Oscillators," in *2012 International Conference on Synthesis, Modeling, Analysis and Simulation Methods and Applications to Circuit Design (SMACD)*, Seville, Spain, pp. 53-56, Sep. 2012.

[64] O. Boric-Lubecke, Dee-Son Pan, and T. Itoh, "DC instability of the series connection of tunneling diodes," *IEEE Transactions on Microwave Theory and Techniques*, vol. 44, no. 6, pp. 936-943, June 1996.

[65] Liquan Wang and E. Wasige, "Tunnel diode microwave oscillators employing a novel power combining circuit topology," in *European Microwave Conference (EuMC)*, Paris, pp. 1154-1157, Sep. 2010.

[66] E. F. Calandra and A. Sommariva, "Transient analysis of multiple tuned injection-locked amplifiers with modulated input signal," *IEEE Transaction on Microwave Theory and Techniques*, vol. 37, no. 5, pp. 826-835, May 1989.

[67] E. F. Calandra, M. Caruso, and D. Lupo, "Computationally efficient analysis of microwave injection-locked amplifiers," in *21th International Crimean Conference "Microwave and Telecommunication Technology" (CriMiCo)*, Sevastopol (Ukraine), pp. 239-242, Sep. 2011.

[68] Ying Chen, K. Mouthaan, and F. Lin, "Design of X-Band and Ka-Band Colpitts Oscillators Using a Parasitic Cancellation Technique," *IEEE Transactions on Circuits and Systems I: Regular Papers*, vol. 57, no. 8, pp. 1817-1828, Aug. 2010.

[69] R. P. Nanavati and C. A. Morato De Andrade, "Tunnel diode junction capacitance in the vicinity of built-in voltage," *Proceedings of the IEEE*, vol. 51, no. 11, p. 1679, Nov. 1963.